



# Robust Optical Diffractive Technique to Read Out Cantilever Deflection

Benjamin Dueck

London Centre for Nanotechnology
University College London

January 2010

Supervisors:
Dr. Rachel A. McKendry
Prof. Dr. Gabriel Aeppli

Thesis submitted for the degree of Doctor of Philosophy
at the University College London.

Nothing in the world can take the place of persistence.

**Talent** will not;
nothing is more common than unsuccessful men with great talent.

**Genius** will not;
unrewarded genius is almost a proverb.

**Education** will not;
the world is full of educated derelicts.

Persistence, determination alone are omnipotent.

*Calvin Coolidge (1872-1933)*
*30th President of the United States*

I, Benjamin Dueck, confirm that the work presented in this thesis is my own. Where information has been derived from other sources, I confirm that this has been indicated in the thesis.

# Abstract

Microcantilevers have now been used successfully for over a decade. New assays are being developed and tested continuously but the technique has not arrived in hospitals and surgeries yet. The main obstacle was that a robust and reliable readout system which does not need intricate alignment before each measurement was not available. Therefore cantilever devices have only been used in university laboratories. The aim of the research presented in this thesis is to provide a diffractive optical readout for cantilever bending that is rapid, robust and easy to use.

The diffractive readout discovered during my PhD involves a laser illuminating the entire cantilever and additionally parts of the chip base to which it is attached. The laser light diffracted from the cantilever contains information that allows a distinction to be made between tilting and bending of the cantilever. Additionally, measurements of the absolute tilting and bending can be performed and the time needed for aligning the cantilever chip in the laser beam is reduced to a minimum.

This thesis describes the tools used to develop the diffractive readout and presents experimental results. First, a simulation was programmed to predict results and optimise experimental conditions. Second, an experimental setup was built from scratch and a new flow cell designed which was needed for transmission mode experiments. Third, test experiments in air were performed using a transmissive and a reflective diffraction approach. Fourth and finally, the applicability of the diffractive

readout was shown by demonstrating that the binding of the antibiotic vancomycin to a glycopeptide could be measured successfully.

I hope that the invention presented in this thesis will help to commercialise the cantilever setup and make it attractive for the use in hospital and surgeries speeding up diagnostic steps from days down to a few minutes.

This thesis lays the cornerstone of the discovered, patented and tested optical diffractive readout technique for cantilever based biosensors. Optimisation of the experiment, being very important and essential, has to be focused on in the future and is not dealt with in detail in here.

# Acknowledgement

First of all, I thank God for all the wonderful people which played a crucial role during all the stages of my PhD. Without their invaluable help I would not have been able to come to London, to program simulations, to perform experiments and to document everything in this thesis.

I am very grateful for my supervisors Prof. Gabriel Aeppli and Dr. Rachel McKendry who supported me over the last three years and shared their extraordinary knowledge and experience with me, spending a lot of their precious time. Also, I would like to thank them for reading the manuscript and providing me patiently with comments for further improvement.

It is a pleasure to thank all the members of Dr. Rachel McKendrys group who are great examples for me. I would like to thank Dr. Joseph Ndieyra for sharing his optimism, Dr. Moyu Watari for having company when working late hours, Manuel Vögtli for taking me to concerts in the Royal Albert Hall and Lars Henrik Skjolding for spreading his entrepreneurial ideas.

I am indebted to

- Dr. Steven Lynch and Dr. Bart Hoogenboom for sharing their knowledge about optics and always helping to solve problems.
- Nipa Patel, Rosie Baverstock-West and Denise Ottley for superbly mastering the red tape.
- The technical team, Steve Etienne, Kevin Lee and Mike Cresswell, for training and support using equipment in the clean room.
- Dr. Steven Nesbitt, Brian Nicholls, Richard Thorogate for keeping the laboratories up and running.
- Robert Gollay and James F. Percival from the chemistry workshop for designing and manufacturing parts for my experiments.
- Dr. Mike Arnott from UCL-Business for successfully filing patents.

The research and scholarship was generously funded by EPSRC.

Most of all I would like to thank my wife Daniela and my daughter Lisa Joy for a fabulous time in London which I will never forget.

Thank you all for your great support and constant encouragement!

# Contents

# List of Figures

# List of Tables

# 1 Introduction

Being able to predict the events happening in the future has always been seen as a big advantage. Knowing, for example, the weather or share prices in advance puts us in the fortunate position not to be left out in the rain. But the most important treasure for most people is to have good health. In order to stay fit it is crucial that health can be monitored effectively and diseases be diagnosed as early as possible.

The most prominent techniques used in clinics or centralised laboratories to detect bacteria or viruses are the polymerase chain reaction (PCR) and variations of it as well as enzyme-linked immunosorbent assay (ELISA). PCR was developed by Kary Mullis in the 1980s as a technique to make millions of copies of fragments of deoxyribonucleic acid (DNA) in a few hours and can therefore detect the presence of DNA coming from a virus or bacteria [2, 3, 4]. ELISA assays were developed independently and simultaneously by the group of Peter Perlmann and Eva Engvall at Stockholm University in Sweden [5], by the group of Anton Schuurs and Bauke van Weemen in the Netherlands [6], and by the group of Avrameas at the Pasteur Institute in France [7, 8, 9]. These techniques have been used successfully in the last years and a variety of different tests have been developed since then. However these methods involve sample amplification and labelling with fluorescent or radioactive tags, which involves multiple reagents, reaction steps and trained technicians meaning that it is time consuming and expensive. Labelling a molecule of interest may also perturb the results by altering the delicate conformation of a biomolecule.

Label-free detection methods have been developed in the last decades and according to Comley their future never looked brighter [10]. Label-free methods offer the advantage that biomolecules can be rapidly detected in a single step reaction with no additional reagents or steps thereby reducing the time and cost of an assay. This thesis presents a diffractive optical readout for label-free biosensors which are based on cantilevers.

## 1.1 Cantilever Sensors

The invention of the atomic force microscope (AFM) by Binnig, Quate and Gerber [11] more than 20 years ago was a significant driver for the research on microcantilevers as sensors. The term "cantilever" as it will be used here designates a flat beam that is clamped or supported at only one end. Though the shape is mostly rectangular and differing in length, width and thickness, there also exist triangular structures, T-structures and many more (see Fig. 1.1). The thickness is usually very small compared to the length or width, giving the cantilever a high surface-to-volume ratio.

It was found that instead of just scanning surfaces, cantilevers could be used to sense chemical and biological reactions by tailoring cantilevers with specific capture coatings and then exposing them to different analytes in gas or solution phase (see Fig. 1.2b). Then, their bending is not caused by the interaction of a tip with a surface

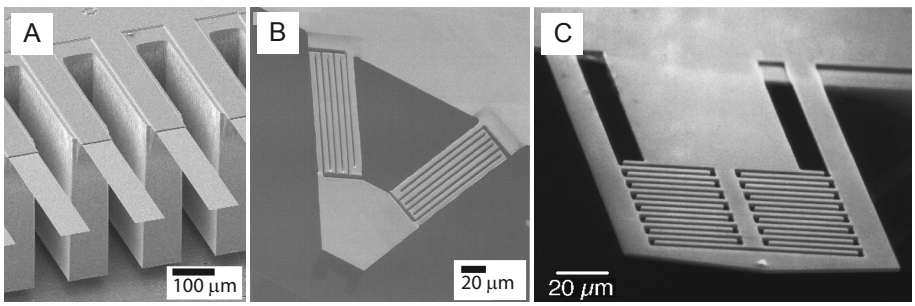


Figure 1.1: (A) Shows the cantilevers used in our group [12] (B) Triangular cantilever modified by FIB [13] (C) Interdigitated cantilevers for interferometric readout [14]

but by processes taking place on the surface of the cantilever itself as described above. These processes change the surface stress and cause the cantilever to bend.

Bending of the cantilever that occurs due to surface stress changes in a biologically relevant sensing application is typically in the range of a 1 nm to 1 $\mu$m. These minute changes, invisible to the naked eye, have to be measured with appropriate readout systems. A variety of different ways to read out cantilever bending are described in this chapter as well as the diffractive read-out technique which was developed and patented [15] during my PhD. A Reprint of the patent can be found in the Appendix A.

### 1.1.1 Advantage of Cantilever Biosensors

The advantage of microcantilever biosensors over PCR and ELISA is, that it is a label free detection technique [16] which reduces the preparatory steps before the actual detection takes place. This decreases the overall time needed for detection, minimises the risk of contaminating precious samples and reduces the interference from the labels during the detection step. Another advantage of microcantilevers is, that they can be fabricated using existing conventional low-cost silicon microfabrication techniques [17, 18] developed for microchip production. These methods can also be used to fabricate arrays consisting of more than thousand microcantilevers [19, 20].

Cantilever sensors have a very high sensitivity [21]. Recently, our group has achieved a sensitivity in the picomolar range (data not published yet). Specificity is accomplished by using reference cantilevers coated with non-specific ligands and acquiring differential measurements. This controls for non specific effects including changes in temperature, refractive index, reactions occurring on the underside of the cantilever or non-specific binding..

Another advantage of microcantilevers over other label-free techniques, such as surface plasmon resonance [22, 23] or quartz crystal microbalance [24] is that the strain which it measures is more biochemical relevant than a change in mass or dielectric constant, because the strain gives insight into in-plane forces of the ad-

sorbed molecules. These insights might further the understanding of the mechanics underlying the measured reaction.

Therefore, using the label free microcantilever technique for disease diagnosis can improve the quality and quantity of the tests. It could also be used as a platform for handheld point of care (POC) devices [25] needing no or very little sample preparation, suitable to be used by non-specialists and in remote areas.

### 1.1.2 Different modes of measurement

Cantilever biosensors can be used in static mode [26, 27] or dynamic mode [28, 29, 30], in air, vacuum, or liquid environment. In static mode a change in the deflection $\Delta z$ of the cantilever is measured and in dynamic mode a change in its resonance frequency $\Delta f$. Both modes should be seen as complementary rather than competitive because they give access to different quantities. Static and dynamic mode measurements can even be performed simultaneously [31].

Valuable reviews on cantilevers have been presented by Lavrik et al. [13], Ziegler [32], Waggoner et al. [33], Carrascosa et al. [34], and Goeders et al. [35].

Two examples for static mode and one example for dynamic mode measurements are discussed in the following.

#### 1.1.2.1 Temperature measurements

In static mode cantilever sensors are very sensitive tools to measure temperature changes. If a cantilever is coated with a metal layer and the thermal expansion coefficients of the cantilever and the layer differ then a change in temperature will cause a deflection $\Delta z$ of the cantilever (see Fig. 1.2a). Timoshenko has reported a theoretical evaluation of the radius of curvature of a bimaterial cantilever as a function of a temperature change $\Delta T$. Using the length $l$ of the cantilever and substituting the radius of curvature with the deflection $\Delta z$ yields the following equation [36]:

$$\Delta z\,(\Delta T) = C\frac{3l^2}{t_1 + t_2}\,(\alpha_1 - \alpha_2)\,\Delta T$$

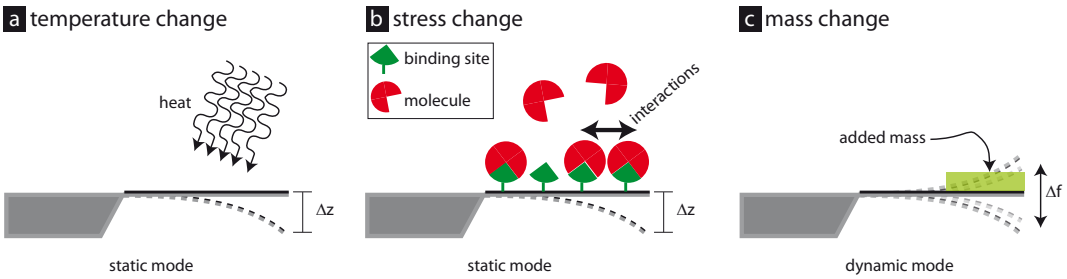


Figure 1.2: Different modes of cantilever measurements. a) Due to the different thermal expansion coefficients of the cantilever (grey) and the surface coating (black) the cantilever bends when a temperature change occurs. $\Delta z$ is the deflection of the free end of the cantilever. b) The cantilever surface is coated with a layer that contains binding sites for specific molecules. Upon binding of molecules, the surface stress changes and bending of the cantilever occurs. The change in surface stress can be caused by the binding process itself and additionally by interactions of the bound molecules like electrostatic attraction or repulsion. c) A cantilever is oscillated at its resonant frequency. Adsorption of mass to it leads to a change in resonant frequency $\Delta f$.

$$\text{with} \qquad C = \frac{\left(1+\frac{t_1}{t_2}\right)^2}{3\left(1+\frac{t_1}{t_2}\right)^2 + \left(1+\frac{t_1 E_1}{t_2 E_2}\right)\left(\frac{t_1^2}{t_2^2}+\frac{t_2 E_2}{t_1 E_1}\right)}$$

$t_1$ and $t_2$ is the thickness, $E_1$ and $E_2$ the Young's modulus, and $\alpha_1$ and $\alpha_2$ the thermal expansion coefficient of the cantilever and the coating, respectively. More recent modifications of the equation above can be found in [37, 38].

Among others, Gimzewski et al. have used the cantilever as a calorimeter and reported a sensitivity in temperature changes of $10^{-5}$ K at 300 K [26].

#### 1.1.2.2 Surface Stress Measurements

A cantilever, like every finite solid body, has surfaces. Every surface is subject to a surface stress. From an atomistic point of view the physical origin of surface stress results from the differences of forces acting on atoms or molecules at the surface to the forces acting on atoms or molecules inside the bulk of the material [39].

The surface stress $\sigma$ is tangential to the surface layer and can be calculated by the Shuttleworth equation [40]:

$$\sigma = \frac{F}{A} + A\frac{\partial\left(F/A\right)}{\partial A}$$

$F$ is the surface free energy and $A$ the area of the surface. The surface free energy is defined as the reversible work per unit area to create a surface and the surface stress is the reversible work per unit area to stretch a surface elastically [41]. The surface free energy is always positive, otherwise the solid would fragment. The surface stress can be positive (tensile) or negative (compressive).

The relation between the radius of curvature $R$ of a cantilever and the difference of surface stress $\Delta\sigma$ between topside ($\Delta\sigma_t$) and underside ($\Delta\sigma_u$) is described by Stoney's equation [42, 39]:

$$\Delta\sigma = \Delta\sigma_t - \Delta\sigma_u = \frac{1}{6}\frac{E_{\text{Young}}}{1-\nu}\frac{t^2}{R}$$

$t$ is the thickness of the cantilever, $E_{\text{Young}}$ the Young's modulus and $\nu$ the Poisson ratio of the material it is made of.

The radius of curvature $R$ of the bent cantilever is a measure for the surface stress change $\Delta\sigma$ that occurs when molecules adsorb to its surface [43]. This technique has previously been described as the "bending-plate technique" [44].

In this thesis the deflection $\Delta z$ of the cantilever at its free end will be used instead of the radius of curvature. Therefore, assuming homogeneous bending, Stoney's equation leads to

$$\Delta\sigma\left(\Delta z\right) = \frac{1}{3}\left(\frac{t}{l}\right)^2\frac{E_{\text{Young}}}{1-\nu}\Delta z \tag{1.1}$$

for a cantilever of length $l$ and thickness $t$. Stoney's equation relates the macroscopic quantity of change in deflection $\Delta z$ of the cantilever to the microscopic quantity of change in surface stress $\Delta\sigma$. Our groups experiments have shown that the surface stress is dependent on chemical charges, temperature, elasticity and geometry of the ligand-receptor complex [45, 46, 12].

When a cantilever is used as a biosensor just one side of the cantilever is coated with a receptor layer while the other side is passivated or left uncoated (see Fig. 1.2b). Now, a reaction occurring only on the side coated with the receptor, and not on the other side, will result in a change of differential surface stress between both sides, leading to a bending of the cantilever.

Thus, the cantilever can be used as a transducer converting biochemical reaction energy into mechanical work. Measurements that rely on the detection of changes in surface stress are known as static mode measurements.

This mode of measurement has been used successfully to rapidly measure DNA hybridisation [47, 48, 16, 49] and recognise proteins [50]. In 2001 Wu et al. demonstrated that microcantilevers can be used for detection of disease-related proteins under clinically relevant conditions and concentrations [51]. Recently, Ndieyeira et al. published work on using the cantilever to measure drug target interactions, studying the binding of antibiotics to an analogue of vancomycin-resistant Enterococcus (VRE) [12]. These are just a few of the many applications which can be found in the literature (see reviews mentioned above).

It should be noted here that it is not straightforward to estimate the amplitude and direction of cantilever bending upon binding of complex molecules given the complicated dependence of the surface stress on the elastic strain of the cantilever [52]. As an example, Wu et al. have observed how adsorption of complementary single-stranded DNA onto the cantilever surface can induce either compressive or tensile stress [48]. Therefore, a multiscale model for predicting amplitude and direction of cantilever bending has been developed recently by Sushko et al. to describe the transduction of simple alkanethiol biochemical reactions into micromechanical cantilever bending motion [46]. It is also not obvious that the binding of a ligand to receptors immobilised on the cantilever surface leads to the uniform stress which is assumed in Stoney's equation. However, that a uniform stress is generated for the detection of the binding of antibiotic vancomycin presented in Chapter 5 has been shown experimentally by Voegtli [53]. His results are also shown in Fig. 1.3.

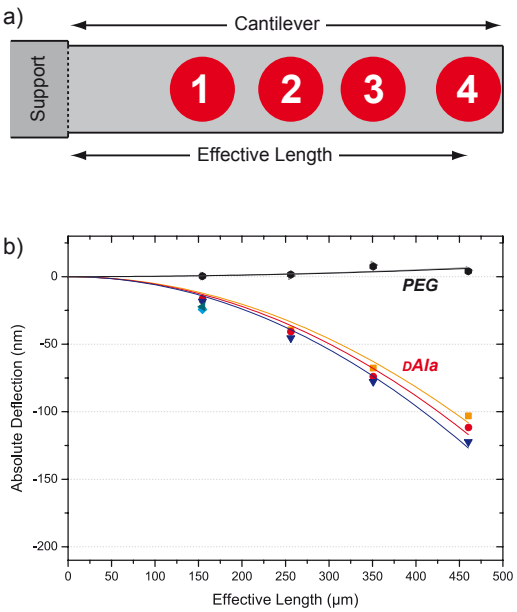


Figure 1.3: Investigation of cantilever curvature upon injection of a 250 $\mu$M vancomycin solution. (a) Schematic of a cantilever showing the four different effective lengths investigated, which are defined as the distance from the hinge to the centre of the laser spot on the cantilever. Red circles represent the laser spots. (b) Absolute cantilever deflection for different effective lengths (symbols) and fit of Stoney's equation (solid lines). PEG cantilevers are shown in black and grey and DAla cantilevers in colour. (Adapted from ref. [53])

#### 1.1.2.3 Mass measurements

The previous two examples showed static mode measurements. Another important mode of measurement is the dynamic mode which is mentioned here for the sake of completeness. However, no dynamic mode measurements have been performed with the optical diffractive readout yet.

In dynamic mode the cantilever can be treated as a mechanical oscillator. In general the cantilever is excited by a piezo actuator to oscillate at its resonant frequency $f_0$ which can be approximated by [54]:[1]

$$f_0(m) = \frac{1}{2\pi}\sqrt{\frac{k}{m_0}} \tag{1.2}$$

The resonant frequency depends on the spring constant $k$ which itself depends on the cantilever dimensions and material. $f_0$ depends also on the mass $m_0$ of the oscillator. If the cantilever oscillates at $f_0$ and a mass is adsorbed on its surface then the resonant frequency will decrease. Therefore a shift in frequency $\Delta f$ can be used to measure mass.

Recently Grueter et al. demonstrated that it is also possible to measure mass and elastics properties of nanometre thick samples [56].

Two examples of this mode of measurement with biological application are the detection of viruses [57] and the weighing of cells [58].

The optical diffractive readout presented in this thesis is tested for static mode measurements only. The first experiments to test the optical diffractive readout employed a temperature change to induce bending of the silicon cantilever which was coated with a titanium and gold layer (see chapter 4). Further experiments were carried out where the bending of the cantilever was induced by the antibiotic vancomycin binding to a receptor layer on the cantilever surface (see chapter 5).

[1] This equation should only be used as a rule of thumb since it does not take into account the dissipation of the resonator energy. A more accurate calculation has been published by Martin et al. in reference [55].

## 1.2 Readout Systems

The readout system is essential to determine the bending of the cantilever which contains information about the chemical processes taking place on the coated cantilever surface. The following four methods have been used most often:

1. Capacitive readout (e.g. [59, 60])
2. Piezoresistive readout (e.g. [61, 62])
3. Metal–Oxide–Semiconductor Field-Effect Transistor (MOSFET) readout (e.g. [63, 64])
4. Optical readout (e.g. [65, 66])

Lavrik et al. include information in their review about the piezoelectric method and electron tunnelling [13] which will not be discussed in more detail here due to their infrequent use. The next paragraphs will describe the four readout techniques listed above.

### 1.2.1 Capacitive Readout

A capacitor can store energy between two electrodes which are separated by a dielectric. The capacitance of energy it can hold depends mainly on the geometry of the electrodes, their distance $d$ to each other, and the dielectric constant $\epsilon_{\mathrm{dielectric}}$ of the medium between them. For a simple capacitor with two parallel plates, having a surface area $A$ each, the capacitance $C$ can be calculated using the following equation [67]:

$$C = \frac{\epsilon_{\mathrm{dielectric}} A}{d} \tag{1.3}$$

This simple relation reveals how the capacitance changes when the distance between the two electrodes is increased or decreased. How this is exploited for the cantilever sensors can be seen in Fig. 1.4. One electrode, the counter electrode, is fixed and the cantilever is used as the second electrode. If bending occurs, the

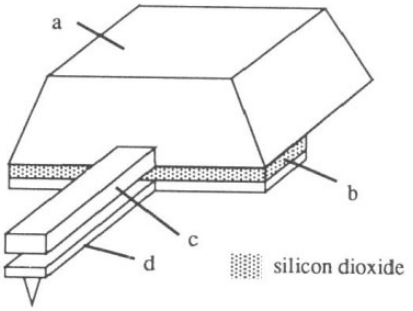


Figure 1.4: Integrated capacitive cantilever readout used for AFM: (a) carrier, (b) insulating $SiO_2$, (c) counter electrode, (d) cantilever with tip [68]

cantilever changes its distance to the counter electrode. Therefore, the capacitance changes which can be measured and displayed.

The sensitivity of the capacitive readout can be expressed as the change of $C$ with respect to $d$:

$$\frac{\partial C}{\partial d} = -\frac{\epsilon_{\text{dielectric}} A}{d^2} \tag{1.4}$$

From Eq. 1.4 it is obvious that the sensitivity does strongly depend on $d$ but also on $\epsilon_{\text{dielectric}}$ and $A$. A smaller separation between the plates or increasing the surfaces of the cantilever and the counter electrode will increase the sensitivity.

Göddenhenrich et al. have reported a resolution in bending of 10 pm [69].

While the first is compatible with miniaturisation the latter is not. The main application for this technique is the detection of gases. For example, Amirola et al. used a micromachined cantilever for a gas sensing application and were able to detect volatile organic components (VOC) [60]. The limits of detection were reported as 50 ppm for toluene and 10 ppm for octane. The use in liquid is limited especially when $d$ becomes very small because of electrical insulation problems.

### 1.2.2 Piezoresistive Readout

Piezoresistive material changes its electric conductance when exposed to changes in mechanical stress. Hence, the change in conductance of piezoresistive material embedded in a cantilever can be used to measure its bending. The size of the signal depends on the gauge factor $GF$ which in turn depends on material properties and

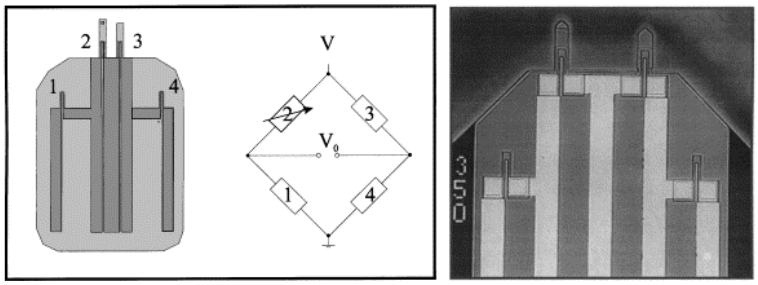


Figure 1.5: Schematic drawing and microscope image of AFM probe with integrated piezoresistive readout. The cantilevers are approximately 50 µm wide, 200 µm long and 1.5 µm thick [62].

geometry. It is defined as the relative resistance change per unit strain $\epsilon_{\text{strain}}$ [70]:

$$GF = \frac{\Delta R}{R_o} \frac{1}{\epsilon_{\text{strain}}}$$

where $R_0$ is the resistivity of the unstrained material and $\Delta R$ the change in resistivity. Since a higher $GF$ gives better sensitivity, researchers have tried to use different materials or doping to increase the $GF$. Rowe et al. combined silicon and aluminium and used a special geometry. They report a $GF$ of 843 which is eight times higher than usually achieved with doped silicon [71].

A typical example of a piezoresistive cantilever can be seen in Fig. 1.5, employing a Wheatstone bridge which is a very sensitive circuit to detect changes in resistivity. The detection limit in terms of deflection at the free end of the cantilever is around 50 nm for reproducible results [63].

### 1.2.3 MOSFET Readout

The metal–oxide–semiconductor field-effect transistor (MOSFET) readout relies on a change in channel mobility due to a change in surface stress as shown in Fig. 1.6. A fixed biased voltage is applied on the gate and source-drain region and every change in channel mobility will result in a change in drain current. Sheckhawat et al. achieved a sensitivity of $<5$ nm [63]. Although the sensitivity is sufficient for biological applications there are some drawbacks which are mentioned further down.

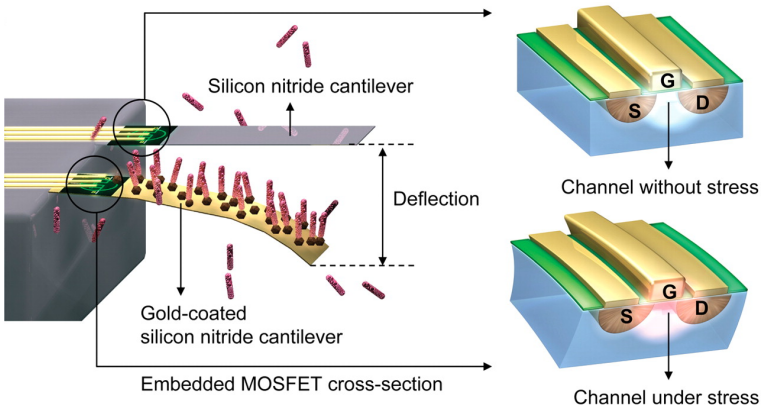


Figure 1.6: Cantilever with MOSFET readout [63].

### 1.2.4 Optical Readouts

Most existing devices use optics to read out the cantilever bending. These can be classified into techniques using geometrical optics and those using interferometric or diffractive optics.

#### 1.2.4.1 The Optical Lever Technique (Geometrical Optics)

The optical lever technique is used in most instruments which need to measure cantilever deflection quickly and reliably. Its attractiveness lies in its simplicity, consisting of a laser, a reflective surface on the cantilever and a photo sensitive device (PSD) as shown in Fig. 1.7. The laser is reflected from the free end of the cantilever and the position of the reflected beam is monitored with a PSD.

The information needed to compute the bending are the distance $d$ between PSD and cantilever and the length $l$ of the cantilever. A change in the deflection $\Delta z$ results in a change of position $\Delta s$ of the reflected beam on the PSD, because the law of reflection states that the angle of the incoming light beam equals that of the reflected beam. If the deflection of the cantilever $\Delta z$ is small compared to $l$, one can use the small angle approximation $\sin\varphi \approx \tan\varphi \approx \varphi$. Then the following simple geometrical relations hold true to calculate $\Delta z$ from measuring $\Delta s$:

$$2\varphi = \frac{\Delta s}{d} \qquad \text{and} \qquad \varphi = 2\frac{\Delta z}{l}$$

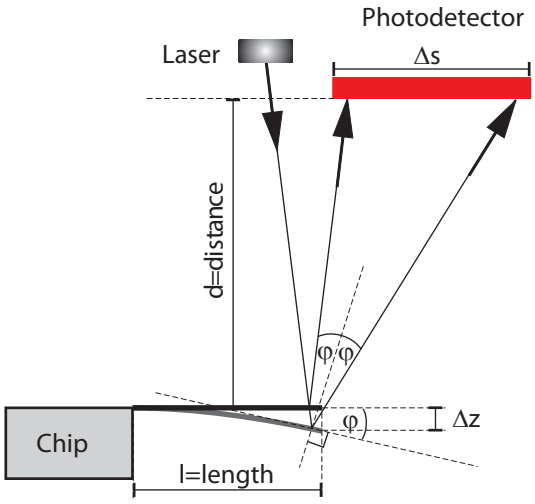


Figure 1.7: Geometry of optical readout where Δz is the deflection at the free end of the cantilever, d the distance between cantilever and photo detector, l the length of the cantilever and $\varphi$ the opening angle between the flat and the bent cantilever.

(Variables are as defined in Fig. 1.7.) This leads to:

$$\Delta z\,(\Delta s) = \frac{l}{d}\frac{\Delta s}{4}$$

Geometrical optical measurements have also been extended to measure the whole cantilever surface profile by either measuring the deflection at fixed positions with multiple lasers [72] or scanning the spot across the cantilever [73].

#### 1.2.4.2 Interferometric/Diffractive Optics

More recently, the interferometric detection methods were revisited because of their potential for high-resolution measurements of cantilever bending for small cantilevers [13]. The first interferometric cantilever detection was reported by Marting et al. using a laser heterodyne interferometer [55].

Today, many readouts employ phase shifting interferometry as used by Helm et al. [74] and Kelling et al. [75]. The principle is shown in Fig. 1.8. One beam of light is split into two parts, a measuring beam and a reference beam. The reference beam is reflected off a flat reference mirror and interferes with the measuring beam reflected off the cantilever surface. If just one wavelength is used, the interference

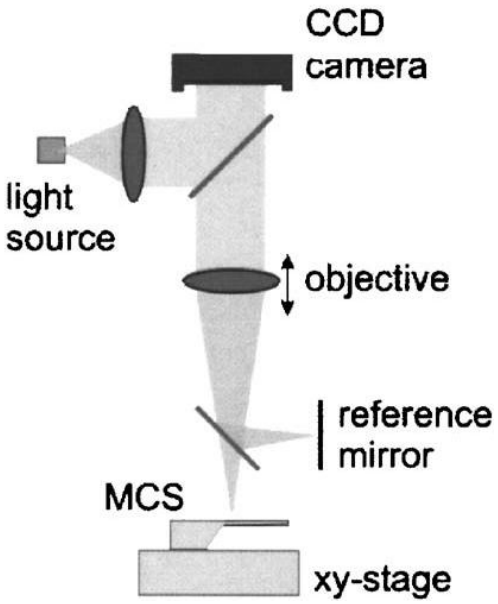


Figure 1.8: Cantilever readout using phase-shifting interferometry [74]

pattern will show constructive interference where the two beams are in phase and destructive interference when the beams are shifted by an phase angle of $\pi$. From the interferogram the bending profile of the cantilever can be calculated. In the case of white light, the reference mirror has to be displaced and the resulting changes in the interference fringe pattern analysed. Using this method Helm et al. resolve bending below 2 nm with a lateral resolution of 2 $\mu$m [74].

Some methods to determine the cantilever bending are different realisations based on the principle of Fabry-Perot interferometry, e.g. [76, 77, 78, 79]. Other solutions are based on coupling the light into the cantilever as published by Zinoviev et al. [80] and Nordström et al. [81].

### 1.2.5 Summary of Different Readout Systems

A whole variety of different readout techniques have been developed, successfully mastering different challenges. A comparison of the resolutions achieved is tabulated in Table 1.1. It has to be kept in mind that resolution is not the only measure to evaluate a readout system. The application, as well as the ease of use and costs are

| Method | Resolution | Reference |
|---|---|---|
| Piezoresistive | 50 nm | [63] |
| MOSFET | 5 nm | [63] |
| Capacitive | 10 pm | [69] |
| Optical beam deflection | 10 pm | [26] |
| Optical interferometry | 1 pm | [26] |

Table 1.1: Typical resolutions for different readout techniques

factors which are more important when translating a technology into the commercial arena.

The main need which led to the development of the diffraction readout presented in this thesis, is to provide a robust technique which is capable of resolving a 1 nm deflection, is easy to use and does not pose strong limitations on parallelising the measurement.

The capacitive readout cannot easily be used in liquids due to electrical insulation problems which occur especially when the distance between the electrodes becomes very small. Together with the piezoresistive, piezocapacitive and MOSFET readouts they have the advantage that they can be used in opaque liquids, like blood, which are inaccessible for optical readouts. The integration of the readout onto the cantilever chip is an advantage and disadvantage at the same time. It is beneficial that external parts are avoided, but at the same time there are restrictions on scaling down the size and thickness of the cantilevers. Scaling up the number of cantilevers for these technique is also costly and problematic since each cantilever requires its own readout and electrical wiring. Often the cantilever thickness is reduced to enhance sensitivity to changes in differential stress. But this approach is not possible for the readouts embedded in the cantilever because it would decrease the resolution of the readout.

Due to their simplicity and their high spatial resolution, optical lever readouts are commonly used in cantilever applications. It is interesting to note that the optical lever technique was first described in 1826 by the founder of the journal *"Annalen der Physik und Chemie"* Poggendorff [82] before it was used later in 1986 by Meyer et al. for cantilever measurements in atomic force microscopy [65].

### 1.2.6 Objective of the Thesis

Looking at the advantages of cantilever based biosensors mentioned in the last sections it becomes apparent that these devices offer great potential to detect and monitor diseases. Also they can be used for investigating drug-target interactions. Bending of the cantilever that occurs due to surface stress changes in a biologically relevant sensing application is typically in the range of a 1 nm to 1 $\mu$m. These minute changes, invisible to the naked eye, have to be measured with an appropriate readout system. To enable the use of cantilever based biosensors in industrial environment or hospitals the following properties should be fulfilled for its readout:

1. The readout should measure deflection with a resolution of 1 nm.
2. The readout should be robust, meaning that it is only sensitive to the bending of the cantilever but not to its tilt or other influences.
3. The readout should be easy to use, meaning that lengthy alignment procedures are avoided.
4. The readout should be applicable for small cantilevers ($<$20 $\mu$m) which exhibit higher sensitivity.
5. The readout should be usable to easily measure multiple cantilever in order to increase the throughput or investigate different reactions simultaneously.

Most readout systems that are currently available meet point one but lack one or more of the other requirements as will be discussed later. Therefore, the main aim of this thesis is the presentation of a new diffractive optical readout for cantilever bending which has the potential to meet all the requirements above. A readout based on diffraction has the potential to be used for cantilevers which are to small to be readout by conventional optical lever technique since effects in the diffraction pattern are enhanced with decreasing size of the object generating it. Decreasing the size and thickness of the cantilever increases its sensitivity.

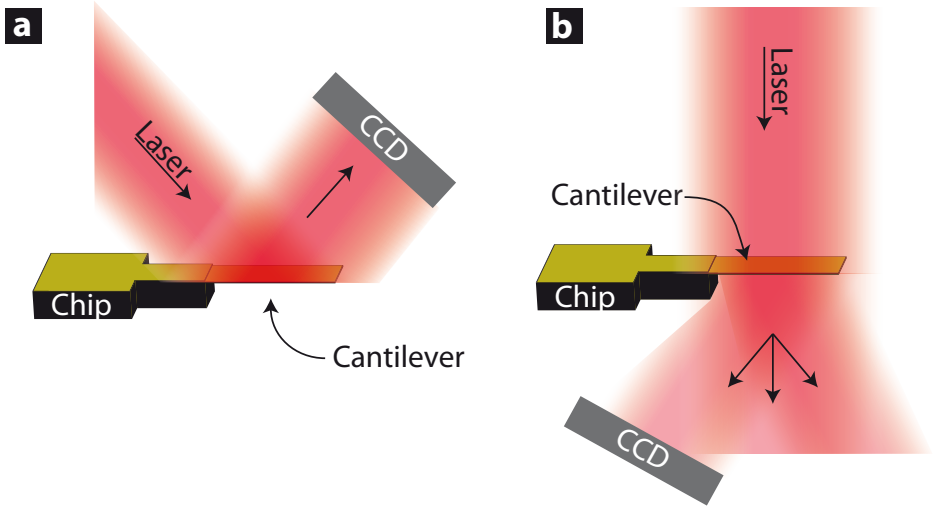


Figure 1.9: The two new diffractive readout techniques. a) Reflection mode measurement b) Transmission mode measurement

Table 1.2 on the following page shows how the different readouts presented above perform for each of the five properties.

## 1.3 The Novel Diffractive Optical Readout Techniques

The conventional optical lever technique uses a laser beam focused to a small spot shining onto the free end of the cantilever. In order to reduce the error in determining the bending of the cantilever the spot has to be as small as possible. With the newly developed diffractive optical readout, the major change visible in the experimental setup is the illumination of the whole cantilever plus parts of the chip base as shown in Fig. 1.9a. One of the features of this technique is that it can be used to measure the bending in reflection as well as in transmission mode.

The laser beam that is diffracted from the cantilever and the chip base in reflection or transmission will be recorded with a charge-coupled device (CCD). The CCD is connected to a computer, and software then analyses the captured diffraction pattern and displays the bending. Alignment is made very easy since the beam of the laser is broader than the cantilever. It is not necessary to place a small focused laser spot precisely on the cantilever at a point known, as is the case for the optical lever

| | resolution (1 nm) | distinguish tilt. / bend. | alignment | miniaturisation | parallelisation |
|---|---|---|---|---|---|
| Piezoresistive | - | + | + | - | o |
| MOSFET | - | + | + | - | o |
| Capacitive | + | + | + | - | o |
| Optical beam deflection | + | - | - | - | + |
| Optical interferometry (Fabry - Perot) | + | - | - | + | o |
| Optical interferometry (phase shifting) | + | + | o | - | + |

Table 1.2: Summary/benchmark of existing readouts. "+" / "-" denotes whether the requirement is fully met/not met. In the cases where it is possible but difficult to meet the requirements, e.g. parallelisation for cantilever arrays with integrated readout is possible but the number of readouts scales with the number of cantilevers and therefore increases the level of complexity. "o" denotes cases where the requirement can be met but only with a considerable effort.

technique. Instead, it is only necessary to place the cantilever somewhere inside the area illuminated by the laser.

## 1.4 Diffraction

### Historical Introduction[2]

Diffraction was first observed, described by Grimaldi and published shortly after his death in 1665 [86]. Eight years later Christian Huygens made a claim based on his intuition known today as the Huygens' principle [87, 88]:

> "the future shape of any given wave surface can be determined by assuming that each point of this surface emits a spherical wave and by constructing the envelope of all these spherical waves."

Later, in 1804 Thomas Young formulated the concept of interference of waves [89, 90] which was then combined with Huygens claim by Fresnel in 1818. But it took until 1882 for the ideas of Huygens, Young and Fresnel to be expressed mathematically using the equations describing the behaviour of electromagnetic fields, proposed by Maxwell in 1860 [84].

Diffraction has been defined by Arnold Sommerfeld in the following way [88]:

> "Any deviation of light from rectilinear paths that can not be explained by reflection or refraction is called diffraction."

Solving diffraction problems analytically is only possible for a very small set of cases which obey a number of boundary conditions, therefore numerical calculations are needed. Huygens' principle is predestined for this.

Before going into detail about the simulation in the next chapter, theoretical background for electromagnetic waves is presented in the following paragraphs which leads to a mathematical foundation of the Huygens' principle which was first worked out mainly by Kirchhoff [91] and then refined by Rayleigh and Sommerfeld [92].

[2] This paragraph is based on accounts in Born [83], Goodman [84], and Priestly found in Appendix 1 of [85]

### 1.4.1 Basics of Diffraction

A laser emits coherent electromagnetic waves with the wavelength $\lambda$. The propagation of electromagnetic waves in free space with the refractive index $n = 1$ is described by the homogeneous wave equations for the electric field $\vec{E}$ and the magnetic field $\vec{B}$

$$\frac{\partial^2 \vec{E}}{\partial t^2} = c^2 \nabla^2 \vec{E} \tag{1.5}$$

$$\frac{\partial^2 \vec{B}}{\partial t^2} = c^2 \nabla^2 \vec{B} \tag{1.6}$$

which can be derived from the Maxwell equations. $c$ is the speed of light and $t$ represents time. $\nabla^2$ is the Laplacian operator which is defined as

$$\nabla^2 \equiv \frac{\partial^2}{\partial x^2} + \frac{\partial^2}{\partial y^2} + \frac{\partial^2}{\partial z^2}$$

Assuming that the wave propagates in a medium which is linear, homogeneous, and non-dispersive, all components of the electric and magnetic field obey the same equation and therefore the behaviour of each component can be represented by one scalar wave equation which is valid for source free regions:

$$\frac{\partial^2 u\,(x,t)}{\partial t^2} = c^2 \frac{\partial^2 u\,(x,t)}{\partial x^2} \tag{1.7}$$

$u = u\,(x,t)$ is a scalar function which depends on time $t$ and the position in space $x$ and represents each component of the $\vec{E}$ or $\vec{B}$ field. This scalar second-order partial differential equation can be further reduced by separating the time dependence using the following ansatz:

$$u\,(x,t) = U(x) \exp\left[-j\omega t\right] \tag{1.8}$$

$j = \sqrt{-1}$ is the imaginary unit and $\omega$ the angular frequency. Substituting Eq. 1.8 in Eq. 1.7 reveals that $U\,(x)$ must obey the following equation, known as the homogeneous Helmholtz equation:

$$\left(\nabla^2 + k^2\right) U = 0 \tag{1.9}$$

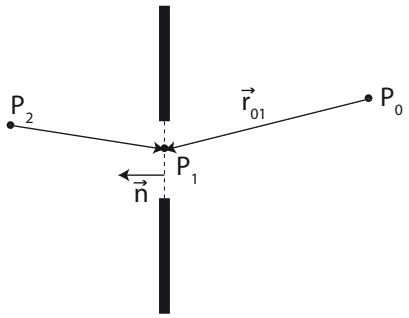


Figure 1.10: Point source illumination of a plane screen [84]

$k$ is the wavenumber defined through the wavelength $\lambda$ or the angular frequency $\omega$ and the speed of light $c$:

$$k = \frac{2\pi}{\lambda} = \frac{\omega}{c}$$

### 1.4.2 Rayleigh-Sommerfeld Solution

The Helmholtz equation (Eq. 1.9) can only be solved for very specific cases. One of them is the aperture in a plane screen shown in Fig. 1.10. Rayleigh and Sommerfeld have been able to provide an analytical solution for this case [84]:

$$U(P_0) = \frac{1}{j\lambda} \iint_{\Sigma} U(P_1) \frac{\exp(jkr_{01})}{r_{01}} \cos\theta \mathrm{d}s \tag{1.10}$$

Looking at Fig. 1.10, $\theta$ is the angle between the vectors $\vec{n}$ and $\vec{r}_{01}$, $r_{01}$ is the distance between the points $P_0$ and $P_1$, $\Sigma$ is the area of the aperture, $U(P_1)$ is the field at point $P_1$ from the incoming wave from $P_2$ and $U(P_0)$ the field at $P_0$.

Examining the Rayleigh-Sommerfeld solution (Eq. 1.10) one can recognise the assumptions made by Huygens, Young, and Fresnel based on their intuition: (1) d$s$ represent infinitesimal small points at the aperture. (2) $\exp(jk_{r_{01}})/r_{01}$ describes the spherical wavelets emitted from each d$s$ and (3) $\int\int_{\Sigma}$ is the mathematical expression for constructing the wave at $P_0$ from the interference of all point sources d$s$ located at the aperture $\Sigma$. Despite lacking the mathematical tools, the agreement of the Rayleigh-Sommerfeld solution with the assumptions of Huygens, Young and Fresnel is astonishing.

## 1.5 Diffraction Pattern - Examples

### 1.5.1 The Double-Slit Experiment

The double-slit experiment (see Fig. 1.11a) which is a modified version of the Young's experiment [93] depicts the generation of a diffraction pattern. The aperture $\Sigma_a$ is illuminated by a monochromatic plane wave having the wavelength $\lambda$. The slits or holes $S_1$ and $S_2$ act as in-phase coherent emitters. For a point $P$ on $\Sigma_o$ the optical path length difference for $S_1$ and $S_2$ is $\overline{S_1P} - \overline{S_2P} = r_2 - r_1$ which is approximately equal to $\overline{S_1A} = a \sin\theta$ for large aperture to screen distance $s$. In case $\overline{S_1A}$ is a multiple of $\lambda$ an intensity maximum is produced by constructive interference. It follows, that interference maxima can be observed if

$$\sin\theta = \frac{n\lambda}{a}$$

holds true for $n = 0, 1, 2, \ldots$ The intensity distribution on the screen $\Sigma_o$ is shown in Fig. 1.11b.

### 1.5.2 Diffraction Grating

An aperture containing more than two holes or slits is a diffraction grating. Now, the intensity at a point on a screen at a distance from the grating is determined from the superposition of all the waves that penetrate through the holes in the aperture. To describe the emerging intensity pattern on the screen one can make use of the well known diffraction grating equation. Using the notation in Fig. 1.12 , the intensity as a function of the angle is described by [94]:

$$I(\theta) = I_0 \,\mathrm{sinc}^2\beta \left(\frac{\sin N\alpha}{\sin\alpha}\right)^2 \tag{1.11}$$

$$\text{with } \beta \equiv \frac{kb}{2}\sin\theta \qquad \alpha \equiv \frac{ka}{2}\sin\theta$$

$I$ and $I_0$ are intensities, $k$ is the wave number, $N$ the number of slits, $b$ the slit width, $a$ the spacing between the slits, $\theta$ is defined as in Fig. 1.12 and $\mathrm{sinc} \equiv \sin u/u$.

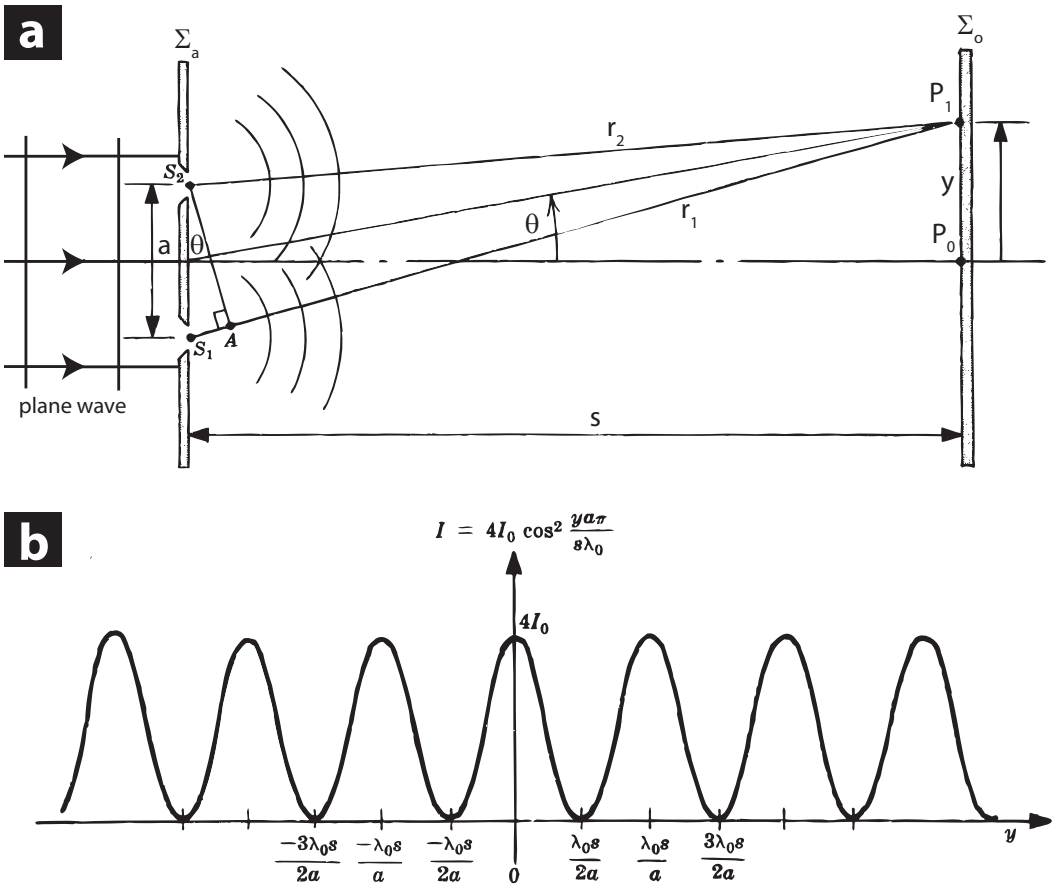


Figure 1.11: a) The aperture $\Sigma_a$ is illuminated by a monochromatic plane wave with wavelength $\lambda$. At the slits $S_1$ and $S_2$ spherical waves are emitted having the same initial phase. Both waves travel to the screen $\Sigma_o$ at distance $s$. The intensity at a point $P$ can be determined from the superposition of both waves. At $P_1$ not to far from the central axis, the phase of the waves from $S_1$ and $S_2$ differ by $r_1 - r_2 \approx \overline{S_1 A}$ due to the different distances travelled. In case $\overline{S_1 A}$ is a multiple of $\lambda$ than constructive interference produces an intensity maximum. Destructive interference occurs for $\overline{S_1 A} = \lambda\left(n + \frac{1}{2}\right)$ with $n = 0, 1, 2, \ldots$ Partial interference occurs if none of both cases exists. b) Shows the intensity of the interference pattern on $\Sigma_o$. It can be observed that the spacing between the maxima increases if $a$ decreases or $\lambda$ increases. (Figures are adapted from [93]).

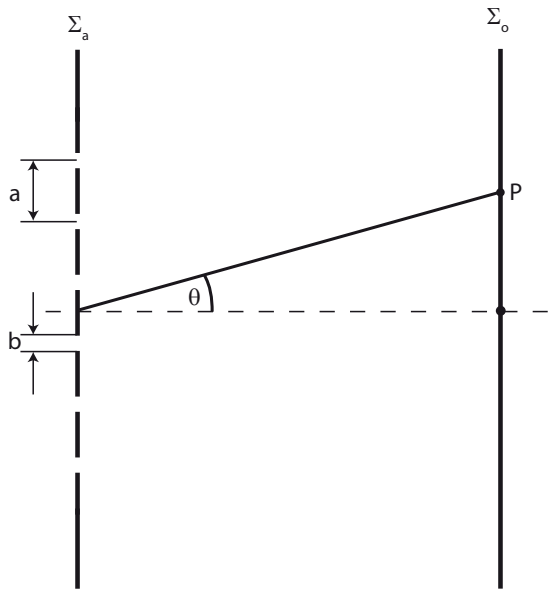


Figure 1.12: Diffraction grating (adapted from [93])

Eq. 1.11 is only valid for the Fraunhofer region also called the far field, i.e. at distances $> N^2a^2\lambda^{-1}$ [94]. Intensity distributions of diffraction patterns in the far field, like the case of the diffraction grating here, can also be calculated by formulating an aperture function that represents the diffraction grating and then compute the Fourier transform of it.

Choosing $a = 15\,\mu$m, $b = 2\,\mu$m, $N = 6$ produces a diffraction pattern on $\Sigma_o$ as shown in Fig. 1.13. The large peaks that can be seen in the diffraction pattern are the Bragg peaks. Their spacing stands in reciprocal relation to the spacing of the slits $a$ in the diffraction grating. Therefore, the diffraction pattern is an image of the diffraction grating in reciprocal space. The small peaks between the Bragg peaks are called Fraunhofer fringes. They are a direct results of the finite size of the diffraction grating or in other words the number of the slits $N$. If $N$ increases, the number of the Fraunhofer fringes between two Bragg peaks will increase but their intensity will decrease until they eventually disappear for $N \to \infty$. Increasing $N$ will also decrease the width of the Bragg peaks and for $N \to \infty$ they will approach an array of Dirac's $\delta$-function, also known as the impulse function.

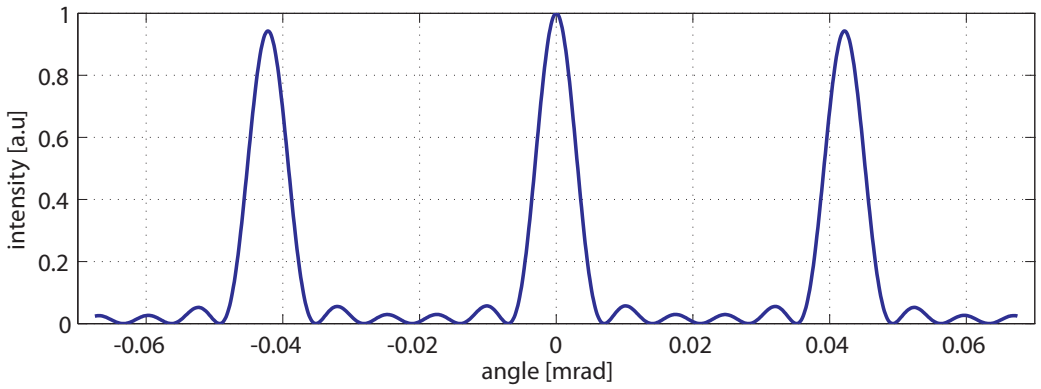


Figure 1.13: Intensity of diffraction pattern in the far field on the screen $\Sigma_o$ for $N = 6$ slits, having a width of $b = 2\,\mu$m and a spacing of $a = 15\,\mu$m. The large peaks are called the Bragg peaks. The small peaks are the called the Fraunhofer fringes.

### 1.5.3 The Cantilever Solution for Numeric Computation

Fig. 1.14 shows a schematic of the scene to be simulated. The main parts to be included in the simulation are the laser beam, the cantilever and the CCD. Calculating a diffraction pattern generated by a cantilever is more complicated than from an aperture in a plane screen as above and there have been no analytical solutions published so far.[3] Therefore the diffraction pattern has to be computed numerically based on the assumption that the reflecting/transmitting parts of the cantilever chip will be thought of as a series of small point sources that emit spherical wavelets (according to the Huygens principle) whose phases are determined by the incoming laser beam. Fig. 1.14c zooms in on the cantilever showing the point sources it is represented by. The spacing between them has been chosen to be $\delta_{\mathrm{PS}} \approx 100\,$nm which is well below the wavelength of the laser $\lambda = 632.8\,$nm. It was found that a further decrease of $\delta_{\mathrm{PS}}$ would not change the results significantly but increase computational costs massively. The electric field $E_m$ of the diffraction pattern at a pixel $m$ of the CCD is calculated by summing the contribution of all $i$ spherical wavelets:

$$E_m = \sum_i \frac{U_i}{d_{im}} \exp\left[-jk\delta_{im}\right] \tag{1.12}$$

[3] An example of curved gratings is known as the Rowland circle (ref. [95] pp. 412)which is very instructing but not readily applicable here.

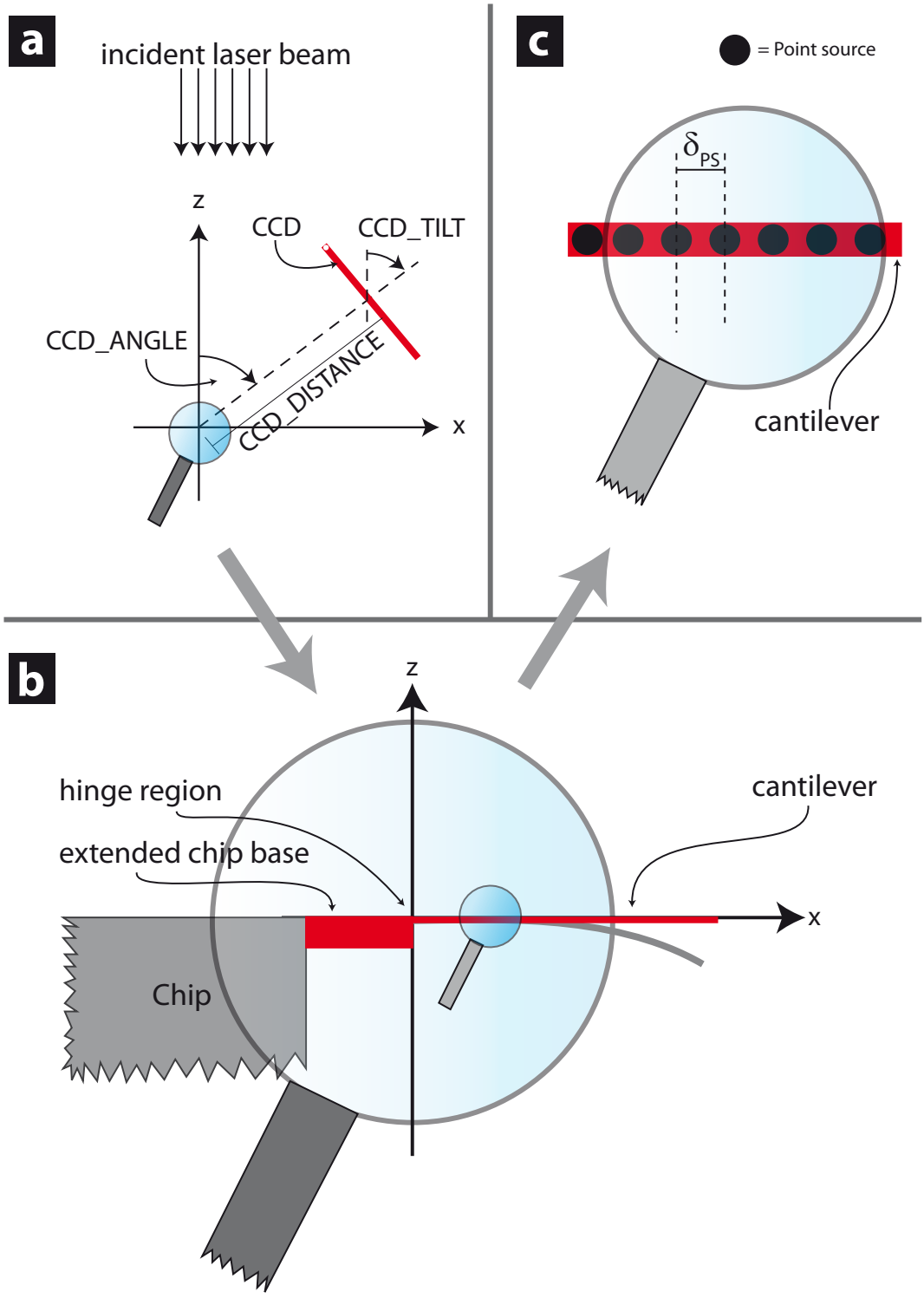


Figure 1.14: Schematic of simulation. (a) Laser beam and CCD in the coordinate system of the simulation. (b) Zoom in on the origin of the coordinate system showing the cantilever, extended chip base (feature of the IBM chips used) and a part of the chip base. (c) A blow-up view on the cantilever showing the point sources by which it is represented by in the simulation.

where $d_{im}$ is the distance between point source $i$ and CCD-pixel $m$ accounting for the decay of the intensity of field, $j = \sqrt{-1}$, $k$ is the wavenumber and $\delta_{im}$ is the phase at the CCD-pixel $m$ of the wave emitted from point source $i$. The real part of $U_i$ represents either the reflectivity or transmittance at $i$ and the imaginary part represents the emitting phase of the pointsource $i$ which depends on its position in the incident laser beam. Once the electrical field at pixel $m$ is known, the intensity $I_m$ can be calculated by multiplying $E_m$ with its complex conjugate value:

$$I_m = E_m E_m^* \tag{1.13}$$

### 1.5.4 Diffraction Pattern from Cantilever

The cantilever itself also acts as a diffracting object. It is helpful to use the geometrical theory of diffraction developed by Keller [96] which states that diffracted waves are caused by edges. The diffraction pattern then is constructed by using geometrical optics and adding the effect of the diffracted waves.

Plane waves of monochromatic coherent light are incident on the cantilever (Fig. 1.15a). For the non-patterned cantilever the transmittance of different parts are shown in Fig. 1.15b (black line). For the chip body the transmission coefficient is zero, meaning that no light is transmitted through it. The extended chip base transmits 3% of the incident light and the cantilever 19% (see Sec. 3.5.1.3 on page 81). Therefore, the edges in the incident beam are at the position $P_0$, $P_1$ and $P_2$. For reasons of clarity only the waves from $P_1$ and $P_2$ are shown in the figure. As in the cases before, the intensity at the point $P_{\mathrm{CCD}}$ is the superposition of the waves coming from $P_0, P_1$ and $P_2$ and depends on the optical path length differences of the three waves. Therefore, the periodicity of the intensity maxima in the diffraction pattern depends mainly on the length of the cantilever and is influenced to a small extend by the extended chip base.

Engraving a diffraction pattern on the cantilever will change the transmission function at the positions where material was milled away. The changes of the real

part of the transmission function due to the diffraction pattern are indicated by the blue line in Fig. 1.15b. Now, the intensity at the point $P_{\mathrm{CCD}}$ will be dominated by the superposition of all the waves transmitted through grooves of the diffraction grating.

One example of a diffraction pattern generated by a patterned cantilever is shown in Fig. 1.16. The diffraction pattern engraved in the cantilever consists of 20 grooves with 1 $\mu$m width (length 61.3 $\mu$m) and a spacing of 23.4 $\mu$m (see Fig. 3.10 on page 84). The diffraction pattern at a distance of approximately 1.5 m was captured with a digital camera. The Bragg peaks and Fraunhofer fringes described earlier can be seen.

A diffraction pattern captured with a CCD is always 2-dimensional (2D). In this thesis only a 1-dimensional (1D) diffraction pattern will be computed in the simulation and the results from experiments will also be presented in 1D form for direct comparison. The 2D patterns are captured with the CCD but only the intensity profile at maximum intensity parallel to the long axis of the cantilever will be analysed (see Fig. 1.16). Therefore, if not mentioned otherwise, all diffraction pattern referred to in this thesis are 1D although, of course, there are tremendous opportunities that follow from the exploitation of full 2D patterns.

More examples of diffraction grating produced by non-patterned and patterned cantilever can be found in the chapter 2 on page 45.

### 1.5.5 Overview of Thesis

The structure of this thesis is the following. Chapter 2 describes and explains how to use the simulation written in MatLab which was employed to optimise the optical diffractive read out. Chapter 3 presents the experimental setup and procedures. In Chapter 4 experimental results are shown comparing the conventional optical lever technique to the diffractive optical readout in transmission and reflection. Chapter 5 shows the a study of drug-target interaction involving the antibiotic vancomycin. Finally, chapter 6 contains a conclusion mentioning the different tasks which need to

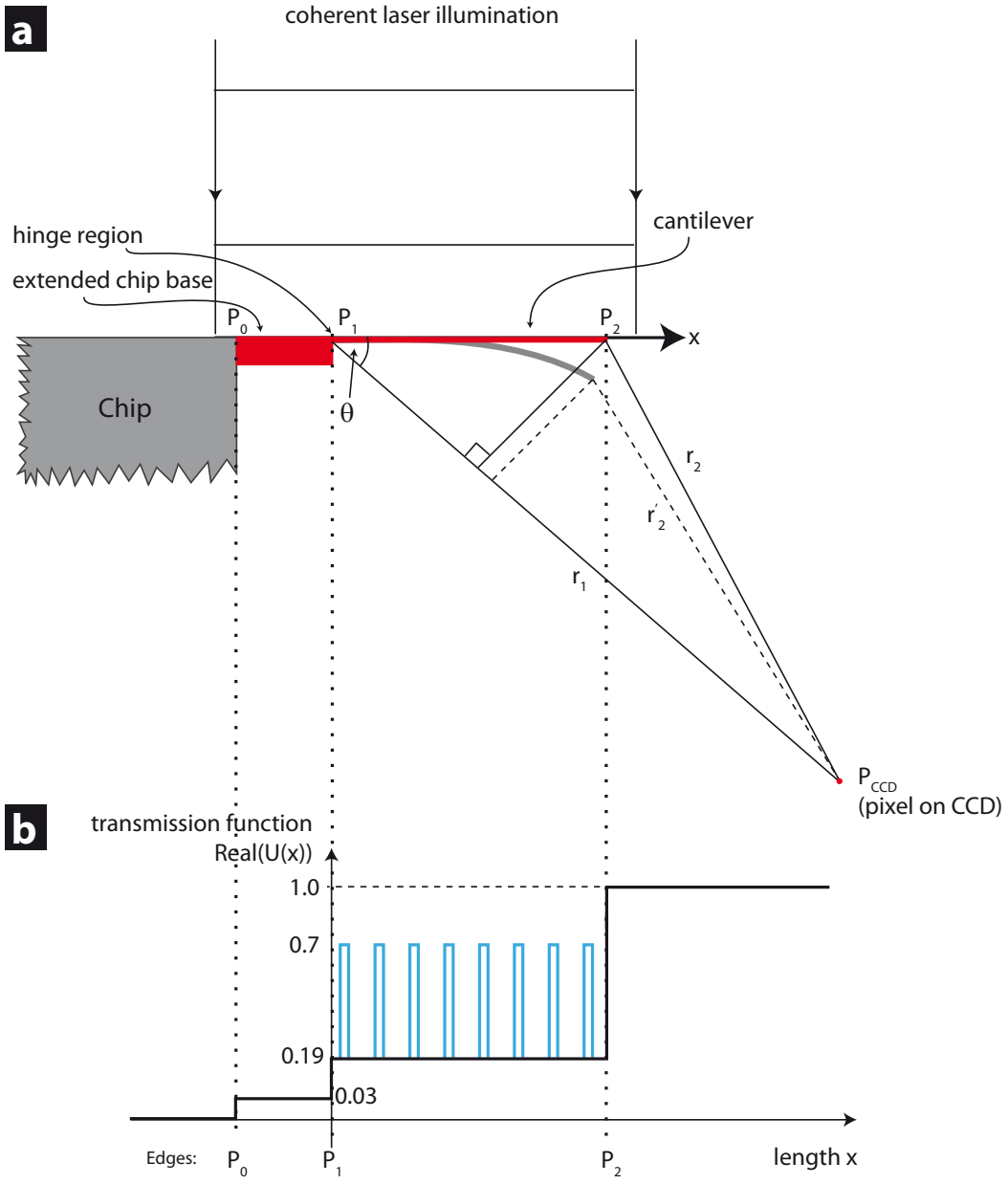


Figure 1.15: This example shows (a) the illumination of the cantilever with a coherent plane wave. (For clarity only the waves from $P_1$ and $P_2$ are shown in the figure.) Therefore the phase of the incoming wave is equal at points $P_1$ and $P_2$ (and $P_o$). The intensity at a pixel $P_{\mathrm{CCD}}$ will be determined by the difference in optical path length of the waves coming from $P_1$ and $P_2$. The black line in (b) shows the real part of the transmission function $U(x)$ for a non-patterned cantilever. Engraving a diffraction grating into the cantilever changes the function as indicated by the blue lines.

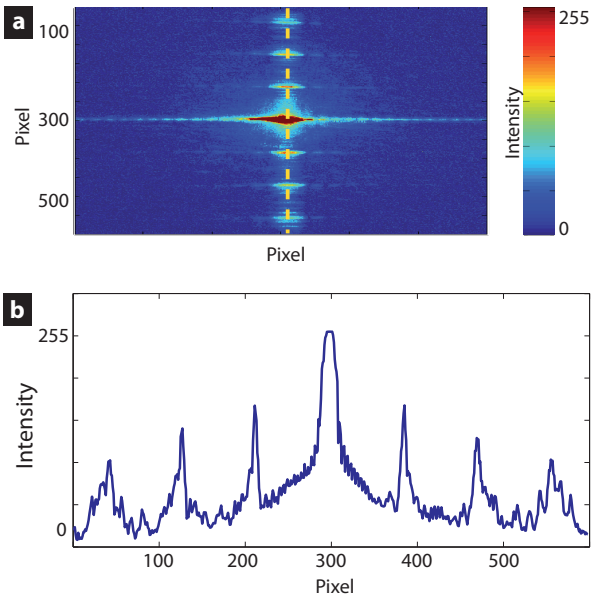


Figure 1.16: (a) 2-dimensional diffraction pattern of the patterned cantilever shown in Fig. 3.10 on page 84 recorded with a CCD. (b) 1-dimensional diffraction pattern representing the intensity profile along the dashed yellow line in (a).

be performed to further optimise the readout. The thesis finishes with a vision on how the readout could be applied and further developed (section 6.3).

# 2 Simulation

The objective in programming a simulation is to be in the position to estimate the outcome of experiments before actually performing them. It can be very helpful for further optimisation of the parameters of the experiment. The task of the simulation is to compute diffraction patterns of cantilevers with different deflections and optical surface properties. An overview of all parts to be simulated is shown in Fig. 2.1.

The simulation has already been mentioned briefly in the previous chapter showing the schematic of the scene to be simulated (Fig. 1.14) and introducing the two equations at the heart of the numerical calculation (Eq. 1.12 and 1.13).

To keep the simulation flexible it was split into modules which can be easily customised. New modules can also be integrated. This chapter describes the modules of the simulation and how they are used.

It should be noted here, that the influence of a change in the refractive index in the pathway of the laser has not been studied so far, because measurements involved either no liquids or liquids with similar refractive indices only.

## 2.1 The Implementation

Matlab (Version R2008b) was chosen to program the simulation. The assumption is made that the cantilever is a rectangular beam, bending is homogeneous ($z(x) \propto x^2$) and occurs only in one axis. Therefore, the cantilever is treated as an one-dimensional

object placed in a two-dimensional environment with a coordinate system as described in Fig. 1.14a.

### 2.1.1 Overview of the Modules

A modular approach was chosen to keep the simulation as flexible as possible. At the time of writing the thesis, the simulation consisted of the following files:

`simulate.m` initialises and executes the simulation.

`simulate_Multicore.m` must be used to initialise and execute the simulation on multiple cores of a central processing unit (CPU).

`init_Main.m` initialises the settings for laser, cantilever and CCD.

`init_CCD.m` initialises the CCD according to the settings made in `init_Main.m`.

`init_Cantilever.m` initialises the cantilever and sets the optical properties.

`calc_TiltingCantilever.m` calculates the new position of the point sources resembling the cantilever for a given displacement of its free end caused by tilting.

`calc_BendingCantilever.m` calculates the new position of the point sources resembling the cantilever for a given deflection of its free end caused by bending.

`calc_InputPhases.m` calculates the phase(s) of the wave front of the incoming laser beam incident on the cantilever.

`calc_InputPhasesFromPointSource.m` calculates the phase of a wave coming from a point source.

`calc_DiffractionPattern.m` computes the diffraction pattern.

`calc_DiffractionPattern_multicore.m` calculates the diffraction pattern using multiple cores of a CPU.

### 2.1.2 Initialisation

The laser beam, the cantilever, and the charged coupled device (CCD) are simulated. The settings for each of these three components will be described here. An overview over the variables to set is found in Fig. 2.1. Further explanations are found in the corresponding section in this chapter.

Variables in `init_Main.m`. with capital letters are global variables which can be accessed from other modules of the source code. The first variable to be set is

`MEASUREMENT_MODE` which can be set to `reflection` or `transmission`.

#### 2.1.2.1 Laser

The following variables have to be set in the `inti_Main.m`. Without loss of generality the incoming laser beam is orthogonal to the flat 1D cantilever, shining on top of it (Fig. 1.14a).

`beam_lambda` sets the wavelength in metres. It is set to `beam_lambda=632.8e-9` to simulate the Helium-Neon laser to be used in the experiment.

`BEAM_INTENSITY` adjusts the intensity of the laser beam to compare results from different simulations.

`BEAM_TYPE` can be set to `collimated`, `point` or `line`. The first will simulate a perfectly collimated wave, the second a point source whose distance will be calculated by the settings for the beam divergence and the third simulates a line of point sources.

`beam_divergence` sets the divergence for the incoming laser beam in radians and is ignored in case `BEAM_TYPE=collimated`.

`source_length` sets the length of the line source (=the laser) in metres.

`number_of_pointsources` sets the number of point sources that resemble the line source.

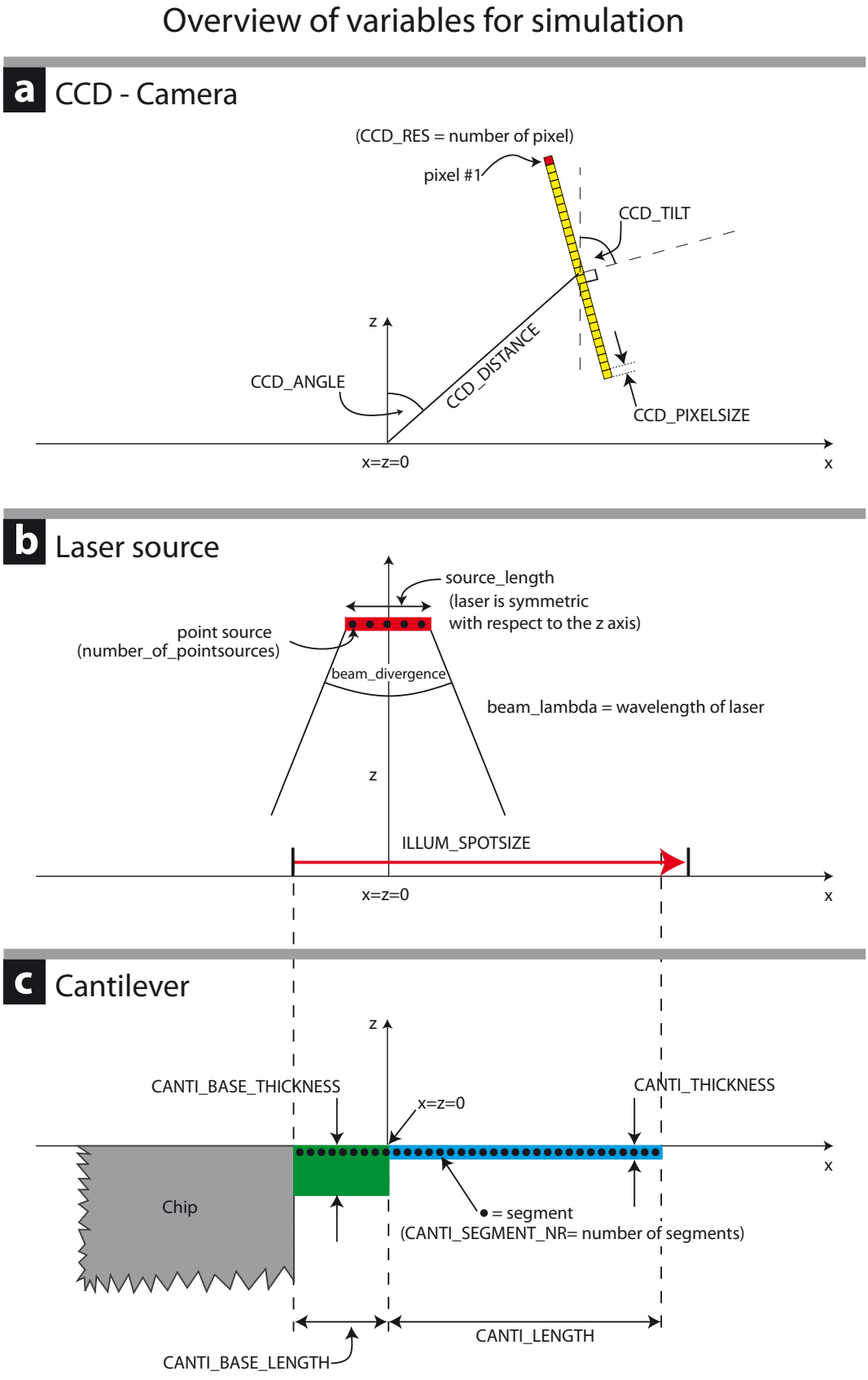


Figure 2.1: Overview over the variables of the simulation. a) Variables for the CCD-camera are explained in Sec. 2.1.2.3. b) Variables for the laser are explained in Sec. 2.1.2.1. c) Variables for the cantilever are explained in Sec. 2.1.2.2.

`ILLUM_SPOTSIZE` sets the width of the spot in units of metres at the position of the flat cantilever.

`ILLUM_PROFILE` can be used to customise the intensity profile of the incoming laser beam to an arbitrary shape at the position of the flat cantilever ($\Delta z$=0), e.g. a Gaussian intensity profile.

Typical settings for the laser used in the experiment are `beam_lambda = 632.8e-9`, `beam_divergence = 1e-3`, `source_length = 1e-3` and `number_of_pointsources = 50`.

#### 2.1.2.2 Cantilever and Chip

**Variables set in** `init_Main.m`

`CANTI_LENGTH` sets the length of the cantilever in metres.

`CANTI_SEGMENT_NR` sets the number of secondary point sources which resemble the cantilever.

`CANTI_TRANSPARENCY` sets a default value for the transparency of the cantilever which can be changed when the optical properties of the cantilevers are set using the function `init_Cantilever` but is ignored in case of reflection measurements. Values are between 0 and 1.

`CANTI_THICKNESS` sets the thickness in units of metres of the cantilever which is used when simulating in transmission mode and is ignored in case of reflection measurements.

`CANTI_BASE_LENGTH` this is a part of the chip that can additionally be illuminated. The length is set in units of metres. By default this part of the chip does not bend when the bending profile of the cantilever is changed. However, it can be set to tilt, when the tilt of the cantilever is changed in order to simulate a rotation of the whole cantilever chip.

`CANTI_BASE_THICKNESS` sets the thickness in units of metres of the extended cantilever base which is used when simulating in transmission mode and is ignored in case of reflection measurements.

`CANTI_BASE_TRANSPARENCY` sets the transparency for the cantilever chip base. In the case of the IBM chip I have been using during the experiments, the extended base is partially transparent and does influence the diffraction pattern when `MEASUREMENT_MODE='transmission'`. It will be ignored in the case of reflection mode measurement. Values are between 0 and 1.

The optical properties of the cantilever surface like reflective patterns are set using the function: `init_Cantilever`. To simulate the influence of bending or tilting of the cantilever the functions `calc_TiltingCantilever` and `calc_BendingCantilever` have to be used, respectively.

Typical values used are `CANTI_LENGTH = 500e-6`, `CANTI_SEGMENT_NR = 5000` and `CANTI_THICKNESS = 1e-6`.

**Functions that initialise the cantilever surface**

`init_Cantilever(pattern)` This function returns a variable which contains the optical reflective properties of the cantilever and the chip to be simulated. This variable is needed for the calculation of the diffraction pattern. The input variable `pattern` can be used to set uniform, periodic or arbitrary reflective properties for the cantilever surface. `pattern` is an array containing at least one vector of two elements. The first specifies a length in metres and the second a coefficient for the specified length which represents the reflectivity in reflection mode or the transparency in transmission mode.

Below are three different examples of initialising a cantilever of 500 $\mu$m length (the length has to be set in `init_Main.m`):

- A completely homogeneous reflecting surface

  ```
  cantilever = init_Cantilever([500e-6 1]);
  ```

- Alternately reflective and non-reflective pattern of patches with 10 $\mu$m and 15 $\mu$m width, respectively:
  `cantilever = init_Cantilever([10e-6 1;15e-6 0]).`
  Here the variable `pattern` consists of two vectors, the first representing the reflective part and the second the non-reflective part. Since the cantilever is chosen to be 500 $\mu$m the pattern will be repeated until the length of the cantilever is reached and then cut off.

- An arbitrary pattern with the sequence 100 $\mu$m - 100% reflectivity/25$\mu$m - 25% reflectivity/0.5 $\mu$m - 0% reflectivity/374.5 $\mu$m - 80% reflectivity will be generated by:
  `cantilever = init_Cantilever([100e-6 1;25e-6 0.25;`
  `0.5e-6 0;374.5e-6 0.8]).`

The variable `cantilever` which is returned from the function `init_Cantilever` is an $i \times 7$ array where $i$ is the number of point sources that represent the extended cantilever base and the cantilever. The seven dimensions contain the following information for each of the $i$ point sources:

1. x-position
2. z-position
3. The reflectivity/transmittance of the cantilever at the position of the point source.
4. A flag to indicate whether the position of a point source should be changed when tilting or bending occurs: flag=0 position is not changed, flag=1 position only changes when tilting occurs, flag=2 position is changed when tilting or bending occurs. This is necessary when the chip base is included in the simulation since it will not change position when the cantilever bends but only when the whole chip is tilted.

5. The angle between the z-axis and the surface normal of the element of the cantilever where the point source is located.

6. The thickness of the cantilever element at the position of the point source.

7. The refractive index of the element at the position of the point source.

The two last dimensions mentioned can be used in transmission mode simulation to check the influence of the thickness of the material on the phase of the penetrating wave.

**Functions that change the bending profile of the cantilever or tilt it**

Each part that is included in the simulation, i.e. the extended cantilever support and the cantilever itself, has been assigned a value in the program which tells the other routines whether it should be included in the tilt or bending operation. Usually the extended cantilever support is only tilted but not bent and the cantilever will be tilted or bent depending on what the settings are. The function responsible for changing the bending profile or tilt are `calcBendingCantilever(straight_cantilever, deflection)` and `calcTiltingCantilever(straight_cantilever, deflection)`. Both functions need the variable `cantilever` as input that contains, among other data, the position of the point sources resembling the extended cantilever base and the cantilever. The second input needed by both functions is the deflection at the free end. Depending on which function was chosen, the cantilever is simply tilted or its surface profile is changed by homogeneous bending.

#### 2.1.2.3 CCD - Camera

All the variables describing the CCD are defined as in Fig. 1.14a.

`CCD_ANGLE` sets the angle in units of radians between the flat cantilever and the axis through the origin of the coordinate system and the centre of the CCD. The positive direction is clockwise.

`CCD_DISTANCE` sets the distance from the origin of the coordinate system to the centre of the CCD in metres.

`CCD_PIXELSIZE` sets the length of a pixel of the CCD in metres.

`CCD_RES` sets the number of pixels of the camera.

`CCD_TILT` sets the tilt in units of radians of the CCD in respect to the axis through the origin of the coordinate system and the centre of the CCD. The positive direction is clockwise. In most cases it is set equal to `CCD_ANGLE`.

## 2.2 Running the Simulation

The function of the simulation is shown by the flow chart in Fig. 2.2. After initialising the laser, the cantilever and the CCD the calculation is started using `simulate.m` or `simulate_Multicore.m` choosing the cantilever bending or tilting to be simulated.

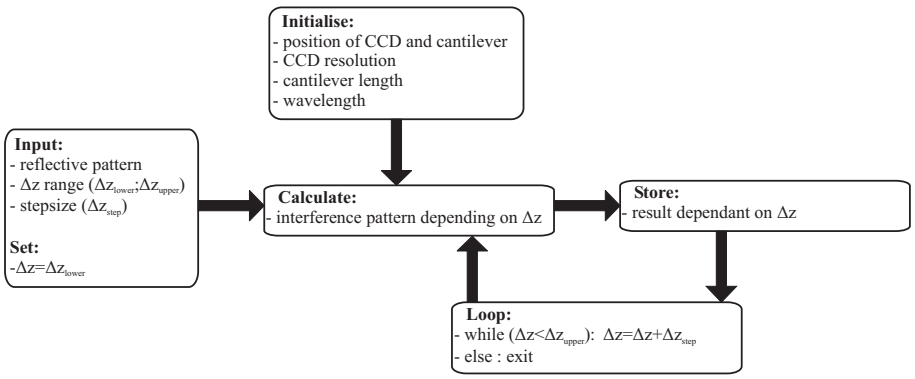


Figure 2.2: Flow chart of simulation

Typically the content of `simulate.m` for running the simulation on one core of the CPU only looks as shown here (lines starting with `%` are comments):

```
1 %%%%%%%%%%%%% BEGIN %%%%%%%%%%%%%
2 %initialise all variables
3 init_Main;
4
```

```
5  %initialise the non bent cantilever with its optical
       properties
6  cantilever=init_Cantilever([500e-6 1]);
7
8  %simulate bending from -1 um to +1 um in 100 nm steps
9  for k=1:21
10   cantilever_bent=calc_BendingCantilever(cantilever, -1e-6+(
         k-1)*1e-7);
11   pattern(k,:)=calc_DiffractionPattern(cantilever_bent,
         init_CCD);
12 end
13
14 %calculate the intensity of the diffraction pattern
15 diffraction_pattern=pattern.*conj(pattern);
16 %%%%%%%%%%%%% END %%%%%%%%%%%%%
```

In line 3 all variables set in the file `init_Main.m` are initialised. Line 6 initialises the reflective properties of the cantilever. In this case it is a 500 $\mu$m fully reflective surface. The `for`-loop from line 9-12 executes the calculation for cantilever bendings (line 10) and the results of the calculation of the complex field intensity is then stored in the variable `pattern` (line 11). After calculating all the complex field intensities for the different bending states, the diffraction pattern is then calculated in line 15 by multiplying the complex field at each pixel with its complex conjugate and is stored in the array variable `diffraction_pattern` which can be used for further analysis or display.

## 2.3 Testing the Simulation

Before using the simulation to predict diffraction pattern, it was checked by comparing its results with solutions of the diffraction grating presented in Sec. 1.5.2.

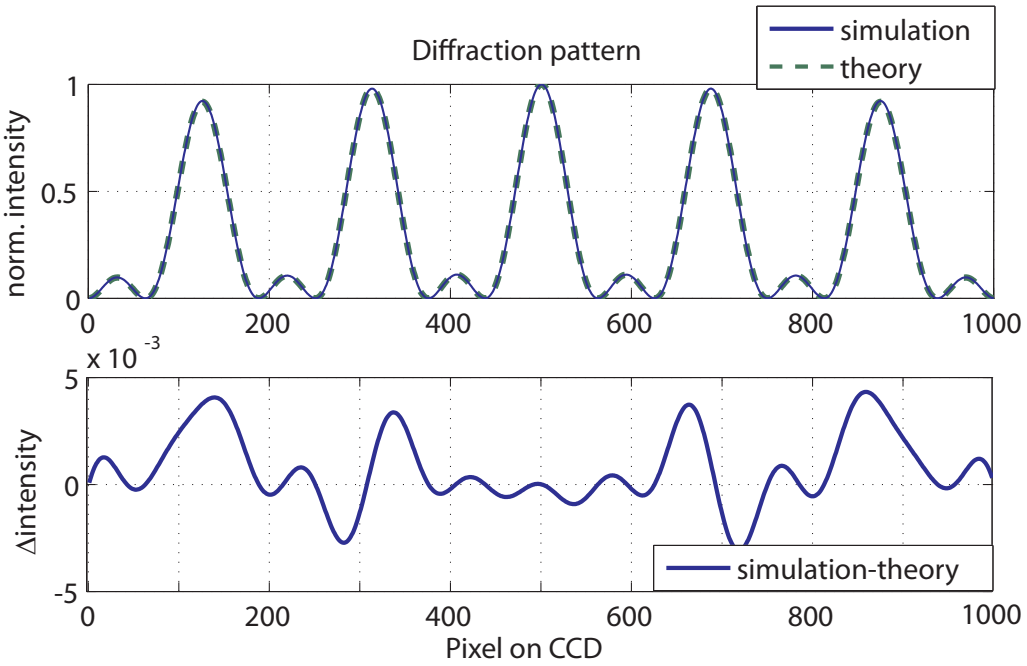


Figure 2.3: Comparison of simulation with theory for diffraction grating

Parameters which were used for the comparison of simulation and theory for the diffraction pattern are as follows:

$$a = 25\,\mu\text{m},\ b = 2\,\mu\text{m},\ N = 3$$

$a$ is the spacing, $b$ the width and $N$ the number of slits. The distance was set to 50.3 cm. To match the theory the incoming laser light in the simulation has to be set to collimated. Very good agreement can be seen in Fig. 2.3. The error in the middle of the detector is lowest and increases slightly to the edges. This increase is caused by the fact that in the simulation the CCD surface is flat whereas Eq. 1.11 assumes a curved CCD surface leading to a deviation in the difference which is symmetric to the 0th order peak (approximately at pixel 500 in Fig. 2.3). Even with this deviation it can be concluded that the difference between simulation and theory is well below 1% in this case.

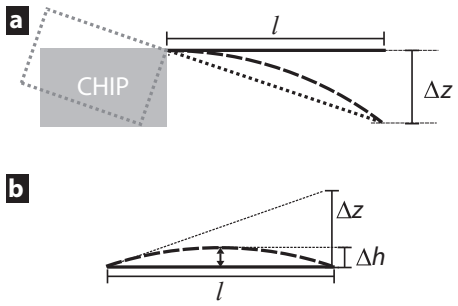


Figure 2.4: (a) shows bending and tilting of a cantilever attached to a chip base and (b) bending of a beam that is not attached to a chip base anymore and will be referred to as "free cantilever".

## 2.4 The Two Modes of Measurements

Two different methods have been explored to measure cantilever bending. Reflection mode measurement is shown in Fig. 1.9a where the laser reflected from the gold coated surface of chip base and cantilever and is recorded using a CCD. Depending on the optical surface properties of the cantilever, diffracted orders higher than the $0^{\text{th}}$ can be produced and recorded. Transmission mode measurements are possible (Fig. 1.9b) due to partial transparency of the cantilever. Higher order Bragg peaks in transmission were generated by embedding a diffraction grating into the cantilever. Typical cases for both modes of measurements are presented in the following paragraphs.

There are also three different ways the cantilever can be deformed which are shown in Fig. 2.4: (a) shows the bending or tilting of a cantilever and (b) shows the bending of a beam which will be called "free cantilever" (not attached to a chip base anymore) from here onward. For the latter case $\Delta z$ is calculated from $\Delta h$ and for small deformation it can be derived that $\Delta z = 4\Delta h$.

The simulation results shown in this chapter serve to give a general overview over

- how the diffraction pattern looks in transmission and reflection mode.
- how the diffraction pattern is affected by cantilever bending.
- how the diffraction pattern is affected by cantilever tilting.

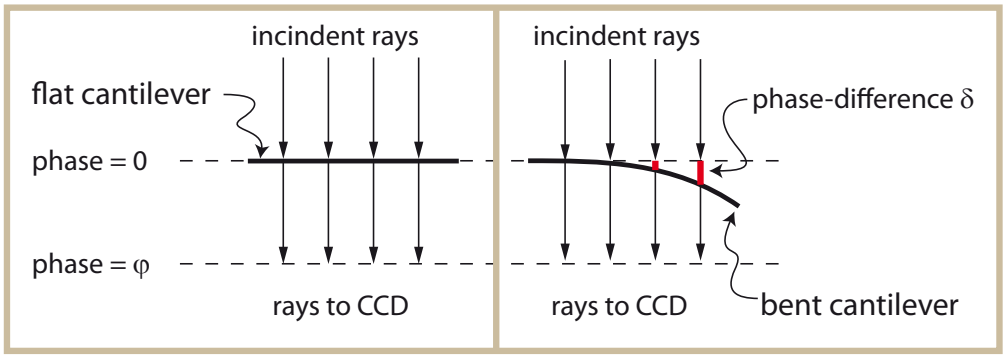


Figure 2.5: Phase difference for $0^{\text{th}}$ order diffraction beam

- what the approximate resolution is which can be achieved for different cases.

### 2.4.1 Transmission Mode

Measuring the intensity in the direct beam line ($0^{\text{th}}$ order Bragg peak) in transmission mode is usually avoided. Firstly, most of the time the intensity is too high and could damage the CCD. Secondly, in our case the changes in the diffraction pattern due to a change in the state of bending of a cantilever are negligible.

The latter can best be explained by comparing a flat cantilever with a bent one as shown in Fig. 2.5. The cantilevers are assumed to be infinitely thin and the phase difference of the incoming and outgoing beam is zero. Once the cantilever is bent, some of the incoming rays have to travel further. Their phase is shifted by $\delta$ when they impinge on the cantilever. At the same time, the same wave after transmission through the cantilever starts with a phase of $-\delta$ when compared with the flat case. The overall result is that there is no difference of the phase in the forward direction of the rays at the CCD position between the flat and bent cantilever. Therefore, observing the diffraction pattern at higher angles is not only necessary but beneficial as will be shown later.

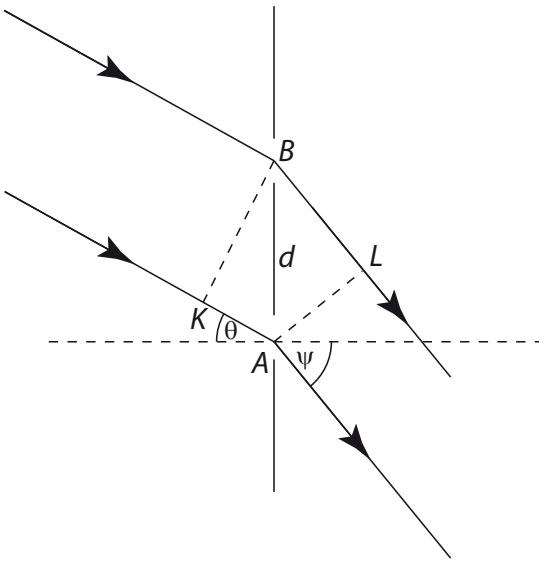


Figure 2.6: Diffraction grating. $A$, $B$, $K$, and $L$ are points on the rays, $d$ is the distance between the slits in the grating and $\theta$ is the angle of the incident beam and $\psi$ the outgoing beam angle (positive in clockwise direction). $A$ is also the centre of rotation for the diffraction grating.

### 2.4.2 Effects of Tilting of a Diffraction Grating

Another interesting question is discussed in this section: In which direction does the diffraction pattern of a cantilever rotate when the cantilever which acts as a transmission diffraction grating is tilted? The answer is not as obvious for the case of transmission as it is for reflection.

This problem is most easily tackled by assuming that the diffraction pattern generated by a cantilever behaves like the one generated by the much more studied general diffraction grating. Fig. 2.6 shows a diffraction grating with the spacing $d$ of the slits. $\theta$ and the exiting beam angle $\psi$ are both defined as being positive in clockwise direction. $\psi$ depends on $\theta$, $d$, the wavelength $\lambda$ and the diffraction order $m$ (with $m > 0$ for $\psi > 0$) as described by the well known Laue equation which can be rewritten for this case in the following way :

$$\sin\psi - \sin\theta = \frac{m\lambda}{d} \tag{2.1}$$

Instead of looking at the rotation of the diffraction grating around $A$ the incoming beam angle $\theta$ is changed and there are three different ways in which $\psi$ can respond

$$\frac{\mathrm{d}\psi}{\mathrm{d}\theta} = \begin{cases} = 1 & \text{case 1} \\ > 1 & \text{case 2} \\ < 1 & \text{case 3} \end{cases} \tag{2.2}$$

Translating these three cases back into the problem of tilting the diffraction grating instead of the incoming laser beam, we get

- case 1: The diffraction pattern does not rotate when the diffraction grating is tilted.
- case 2: The diffraction pattern does rotate in the opposite direction of the tilt of the diffraction grating.
- case 3: The diffraction pattern does rotate in the same direction as the tilt of the diffraction grating.

Which of the three cases is true can be found by using Eq. 2.1:

$$\psi = \arcsin\left(\frac{m\lambda}{d} + \sin\theta\right)$$

$$\frac{\mathrm{d}\psi}{\mathrm{d}\theta} = \frac{\cos\theta}{\sqrt{1 - \left[\sin\theta + \frac{m\lambda}{d}\right]^2}} \tag{2.3}$$

Setting $m = 0$ for the zeroth order diffracted beam and yields:

$$\frac{\mathrm{d}\psi}{\mathrm{d}\theta} = \frac{\cos\theta}{\sqrt{1 - \sin^2\theta}} = \frac{\cos\theta}{\sqrt{\cos^2\theta}} = 1$$

For $m > 0$, small tilts of the grating $\theta \ll 1$ ($\Rightarrow \sin\theta = \theta$ and $\cos\theta = 1$), and $m\lambda d^{-1} \ll 1$ we get:

$$\frac{\mathrm{d}\psi}{\mathrm{d}\theta} = \frac{1}{\sqrt{1 - \underbrace{\left[\theta + \frac{m\lambda}{d}\right]^2}_{=\xi}}} = \frac{1}{\sqrt{1-\xi}} > 1$$

because $0 < \xi \ll 1$ and therefore $0 < \sqrt{1-\xi} < 1$.

In the case of reflection the diffraction pattern rotates in the same direction as the cantilever is tilted. But having derived the case for transmission above, it can be concluded that for $m = 0$ the diffraction pattern does not move when the cantilever acting as a diffraction grating is tilted. Going to higher orders ($m \neq 0$), the diffraction rotates clockwise when the grating is rotated anticlockwise. This effect has also been seen by John et al. performing laser diffraction experiments on periodic dynamic patterns in anisotropic fluids [97]. It will also be confirmed in the chapter on the experiments.

#### 2.4.2.1 Results for non-patterned Cantilever

The standard cantilever arrays from IBM (see p. 79) which have been used throughout all experiments were coated with a homogeneous layer of 2 nm titanium, acting as an adhesive layer, followed by 20 nm of gold.

The diffraction pattern was simulated at three different CCD positions defined by `CCD_ANGLE = 0, 20, 40` degrees and `CCD_DISTANCE = 100e-3`. Three different deflection $\Delta z = -1, 0, 1\,\mu$m were simulated for bending and tilting. The results are shown in Fig. 2.7.

As derived in the last section there is no change of the pattern in the direct beam line for bending/tilting (Fig. 2.7a/b). Simulating the diffraction pattern at 20 degrees for bending/tilting (Fig. 2.7c/d) shows a small change for different bending. The intensity at this angle is decreased by a factor of $10^5$. The high frequency oscillations are the Fraunhofer fringes resulting from the finite size (500 $\mu$m) of the cantilever.

The oscillation of the intensity maxima is caused by the finite extended support with the length of 50 $\mu$m. At `CCD_ANGLE=40` degrees the changes due to bending/tilting (Fig. 2.7e/f) are slightly more pronounced when compared to `CCD_ANGLE=20` but still very minute and a difference between bending and tilting cannot be observed.

#### 2.4.2.2 Results for Cantilever with Engraved Diffraction Grating

The homogeneous gold coating can be turned into a diffraction grating by milling away patches of the gold-layer using a focused ion beam (FIB) as described in section 3.5.1.3 on page 81. The slits milled into the cantilever coating have a width of $\approx$1 $\mu$m with a spacing of 23.4 $\mu$m (see Fig. 3.10 on page 84). Now, only the 12th order Bragg peak was simulated at a distance of 300 mm which occurs at an angle of $\approx$ 21 deg.

Similar to the previous example for the non patterned cantilever, the changes for bending and tilting in Fig. 2.8 look similar. The main difference is, that here we observe a Bragg peak instead of Fraunhofer fringes which shows a slight shift due to bending/tilting of the cantilever.

#### 2.4.2.3 Analysing the Transmission Diffraction Pattern

A figure of merit $FOM_k$ is defined to quantify the difference in the diffraction pattern for sample $k$ to a reference diffraction pattern. It maps the intensity changes of all pixels of one pattern into a single number:

$$FOM_k : \mathbb{N}^{1024} \rightarrow \mathbb{R}$$

$$FOM_k = \sum_{i=1}^{1024} \sqrt{\left(diffp_{k,i} - diffp_{k_{ref},i}\right)^2} \tag{2.4}$$

with $diffp_{k,i}$ being the intensity at pixel $i$ of the diffraction pattern sample number $k$ and $k_{ref}$ the reference sample. In the experimental part the conventional optical lever measurement was performed simultaneously and a proportionality constant

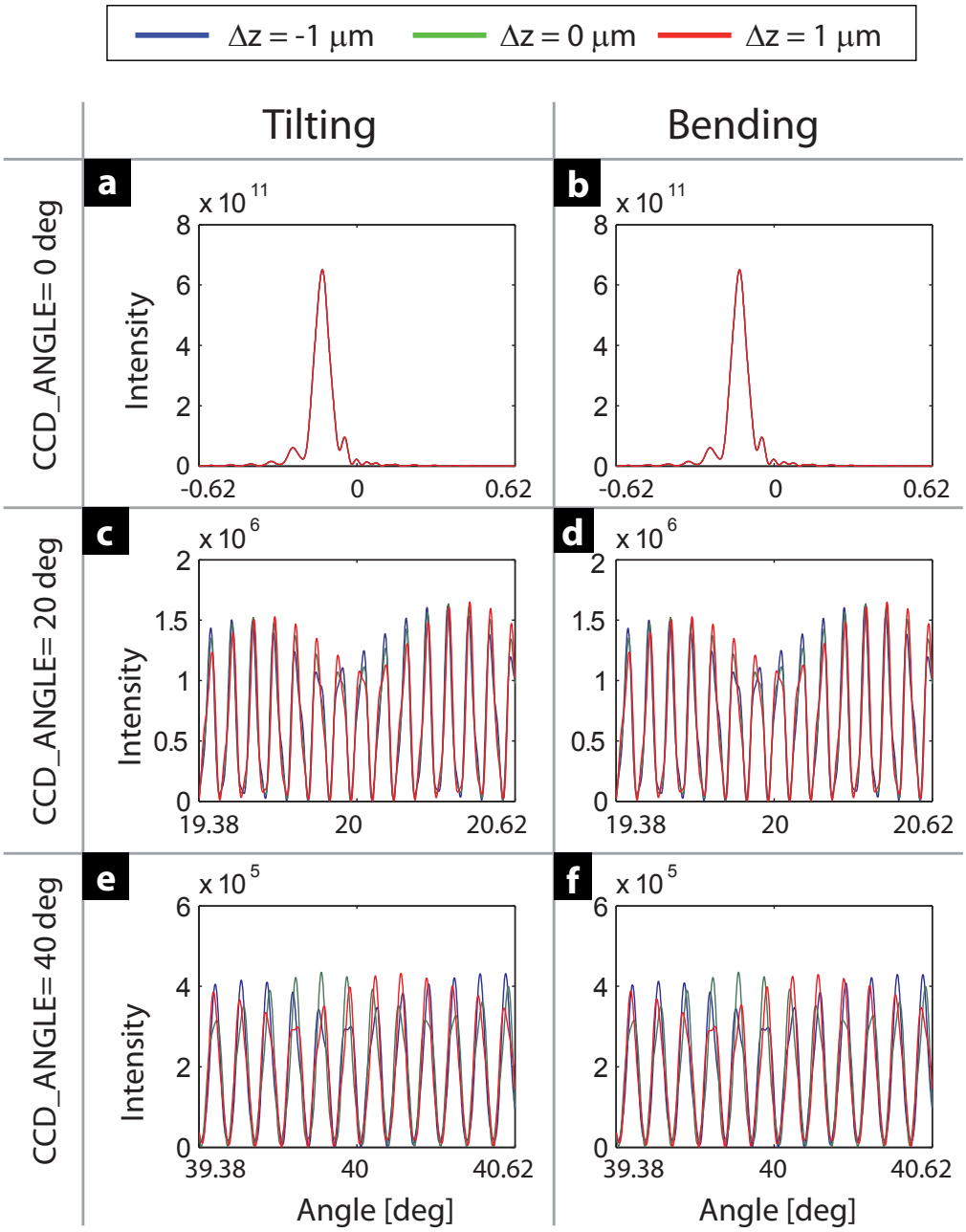


Figure 2.7: Simulated diffraction pattern for a cantilever. a) and b) show the direct beam line whereas the c)-f) are simulated at higher angles and show the Fraunhofer fringes corresponding to the length of the cantilever. The periodicity of the peaks depends on the length of the cantilever and the variation in intensity of the peaks seen in c) and d) stem from the finite size of the extended cantilever support. Since the intensity for the Fraunhofer fringes decays with $1/x^2$, the intensity fall off at higher angles is very small and not visible in c) - f).

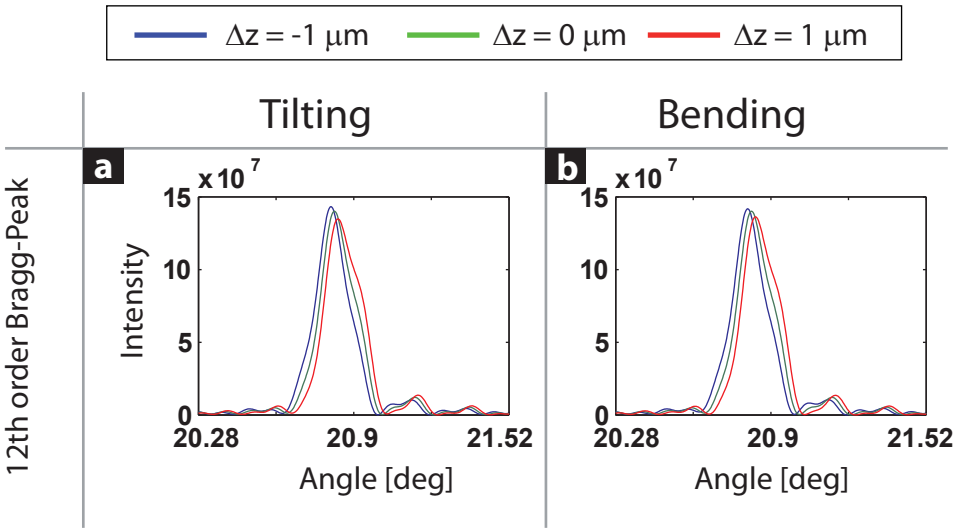


Figure 2.8: $12^{\text{th}}$-order diffraction pattern for differently (a) tilted or (b) bent cantilever.

could be determined relating the $FOM_k$ to the deflection $\Delta z$. Therefore $FOM_k$, once determined, can be used as a measure for the deflection.

This figure of merit was chosen to be sensitive to shift of peaks in the diffraction pattern. It should be noted that in the experiments $FOM_k$ has been found to be approximately proportional to the bending which is not generally to be expected. This proportionality could collapse for large differences in bending or tilting.

### 2.4.3 Reflection Mode

In reflection mode the laser and CCD are on the same side of the cantilever. Simulation for reflection has only been performed for non patterned cantilevers. Two different reflection mode measurements are presented in the following subsections. The first case deals with a laser that illuminates the cantilever only while the second deals with a laser beam that is deliberately expanded to shine onto the cantilever and the cantilever chip.

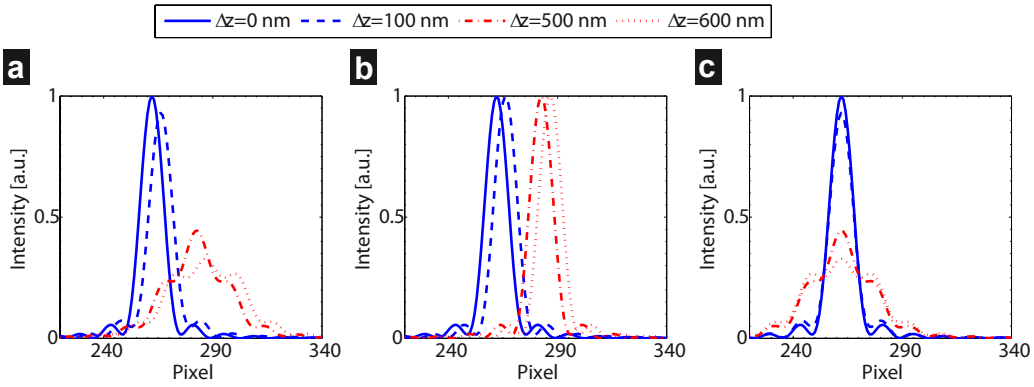


Figure 2.9: Diffraction pattern for bending only (a) and tilting only (b) of a cantilever and bending of a free cantilever (c).

#### 2.4.3.1 Illumination of the Entire Cantilever

Using light diffracted from the entire cantilever and not from a small spot at the free end only includes much more information about changes occurring to the cantilever surface. Simulating the tilting and bending of the cantilever reveals the following as shown in Fig. 2.9: The bending of the cantilever results in a shift of the main peak and a change of its shape (Fig. 2.9a). Tilting the cantilever only changes the peak position but not its shape (Fig. 2.9b). Bending a free cantilever (see definition of free cantilever in Fig. 2.4 on page 56) changes the peak shape but not its position.

The bending of a cantilever as shown in Fig. 2.4a on page 56 can be split up into a tilt and pure bending which is a change in curvature. The simulation in this section has revealed that the influence of tilting and bending on the diffraction pattern can be deconvolved from it.

#### 2.4.3.2 Illumination of Cantilever and Chip Base

As seen in the previous section illuminating the entire cantilever in reflection reveals striking differences in the diffraction pattern between bending and tilting the cantilever. Illuminating additionally a part of the chip base which does not change position when the cantilever bends introduces a reference peak in the diffraction pattern and tilt and bending to be even better distinguished. Assuming that 500 $\mu$m of the reflecting chip base is illuminated additionally to the cantilever, it can be observed that if

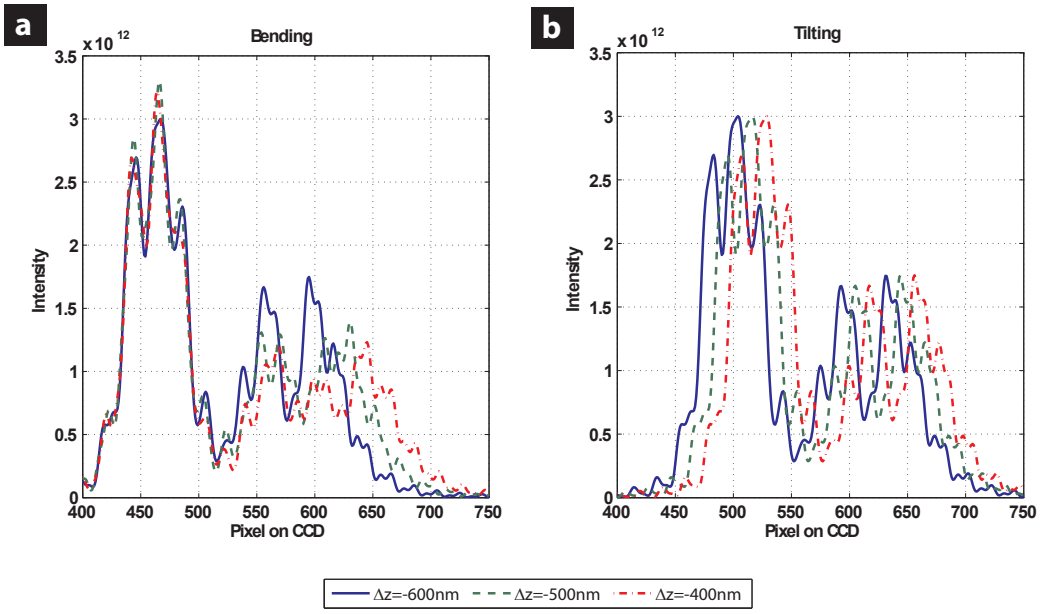


Figure 2.10: Diffraction pattern from simulation of non patterned cantilever in reflection, illuminating the cantilever and parts of the chip base for (a) bending of the cantilever and (b) tilting of the cantilever chip including the cantilever.

the cantilever bends, the whole diffraction pattern increases in width, whereas if the cantilever including the whole chip is tilted around the hinge region of the cantilever, the whole diffraction pattern just shifts as shown in Fig. 2.10. The peak that does not change position when the cantilever is bent will be called the reference peak in the following.

## 2.5 Diffractive Readout with Lens

For some experiments a lens was used in the path of the reflected light between cantilever and CCD in order to capture the entire diffraction pattern of cantilevers with large initial bending. This section describes the equation behind the numerical calculation employed to predict the diffraction pattern captured with the CCD when a lens was used. The source code of the numerical calculation can be found in Appendix B.4.

The numerical approach is based on combining two concepts. Firstly, the cantilever is represented by a phase-modulated diffracting screen which is described in

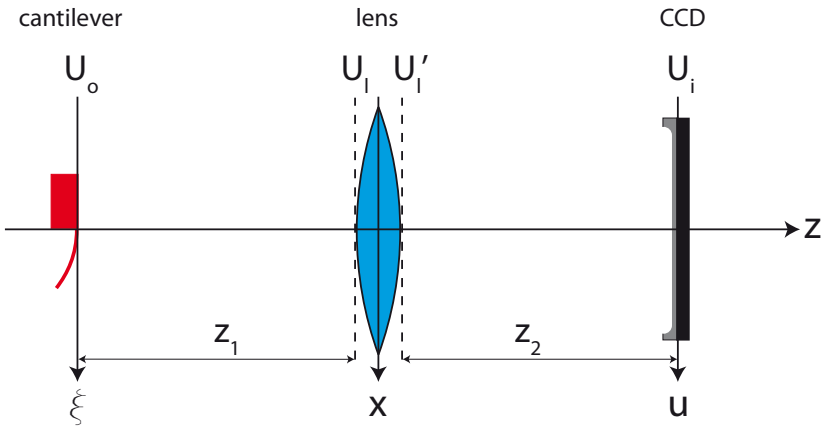


Figure 2.11: Schematic of experimental setup with a lens in the laser beam reflected from the cantilever.

a paper by J. A. Ratcliffe [98]. The phase-modulated screen remains always flat, in the position where the flat cantilever is placed. It only modifies the phase of the reflected wave according to the phase change that would occur when the incoming laser is reflected from a bent or tilted cantilever. Secondly, the Fresnel diffraction equation (Eq. 2.7) as derived by Goodman in reference [84] has been used. Phase factors that only depend on the pixel position of the CCD have been dropped throughout as the intensity of the diffraction pattern is the quantity of interest which is calculated as the product of the magnitude of the electromagnetic wave with its conjugate-complex value.

Fig. 2.11 shows the schematic. The cantilever chip is positioned at $z = 0$ where the electric field $U_o$ is defined which represents the wave reflected from the cantilever. It is assumed that the cantilever is illuminated by a plane wave of unit amplitude, therefore $U_o(x) = \exp[jk\varphi(\xi)]$, with $j$ being the imaginary unit, $k$ the wave number and $\varphi(\xi)$ the phase of $U_o$ at position $\xi$. If the cantilever is not bent $U_o = 1$, otherwise a deflection of $\delta z$ at position $\xi$ will result in $\varphi(\xi) = 2\delta z$ since the beam is traversing the distance between the $\xi$-axis and the cantilever position twice. $U_l$ is the field directly in front of the lens which is the superposition of all the spherical waves diverging from the points $\xi$ on the cantilever. Using the paraxial approximation for

one point source at position $\xi$ would result in a field

$$U_l(x) = \frac{1}{j\lambda z_1} \exp\left[j\frac{k}{2z_1}(x-\xi)^2\right] \tag{2.5}$$

with $\lambda$ being the wavelength and $z_1$ the distance between the $\xi$-axis and the $x$-axis. The lens with focal length $f$ transforms the field $U_l$ into

$$U_l'(x) = U_l(x)\, P(x) \exp\left[-j\frac{k}{2f}x^2\right] \tag{2.6}$$

with $P(x)$ being the pupil function of the lens defining its diameter. For the distance $z_2$ the Fresnel diffraction equation is used

$$U_i(u) = \frac{1}{j\lambda z_2} \int_{-\infty}^{\infty} U_l'(x) \exp\left[j\frac{k}{2z_2}(u-x)^2\right] \mathrm{d}x \tag{2.7}$$

Combining now Eq. 2.5, 2.6, and 2.7 and taking into account that the cantilever chip is represented as a series of point sources located at the $\xi$-axis with their phases depending on the incoming beam, yields the following expression:

$$U_i(u) = \int_{-\infty}^{\infty} h(u;\xi)\, U_o(\xi)\, \mathrm{d}\xi$$

with the impulse response function:

$$\begin{aligned} h(u;\xi) \;=\; & \frac{1}{\lambda^2 z_1 z_2} \exp\left[j\frac{k}{2z_1}\xi^2\right] \\ & \times \int_{-\infty}^{\infty} P(x) \exp\left[j\frac{k}{2}\left(\frac{1}{z_1}+\frac{1}{z_2}-\frac{1}{f}\right)x^2\right] \\ & \times \exp\left[-jk\left(\frac{\xi}{z_1}+\frac{u}{z_2}\right)x\right] \mathrm{d}x \end{aligned}$$

## 2.6 Phase Problem

The previous section dealt with the computation of the diffraction pattern from a known cantilever shape. This is called a direct problem. One aim of this thesis is to provide a technique which allows to determine the cantilever shape from a diffraction pattern. This is called an inverse problem. Equation 1.12 for the electric field of the diffracted wave contains its phase which describes the deflection of the cantilever in the $z$-direction (see Fig. 1.14a for coordinate system). Unfortunately, the CCD camera records only intensity but not the phase.

One possibility to retrieve the phase is using iterative methods. Sayre observed in 1952 that in order to retrieve the phase from an intensity measurement it is necessary to sample the diffraction pattern at twice the Nyquist frequency [99]. The sampling theorem states that in order to perfectly reconstruct a band-limited analog signal it has to be sampled at the Nyquist frequency $2f_{\max}$, with $f_{\max}$ being the maximum frequency in the original signal [100]. Therefore, according to Sayre the diffraction pattern has to be sampled at $4f_{\max}$. Sayres observation led to the development of iterative algorithms by Gerchberg and Saxton [101, 102] and later by Fienup [103]. These algorithms have been further developed and are used today to reconstruct 2D and 3D objects with a spatial resolution in the range of 20 nm [104, 105] and resolve a deformation of lattice spacing in the order of 0.5 $\AA$ using x-rays of 1.3 $\AA$ wavelength [106, 107].

Unfortunately, this method cannot be used to calculate the phase from the diffraction pattern of the experiment presented in this thesis since the solutions for 1D problems are usually non-unique [108]. For 2D and 3D it has been shown that a unique solution almost always exists [109]. It may be possible to find constraints, suitable for the case of the cantilever, in order to ensure a unique solution to the inversion of the 1D diffraction pattern. Then, it would be possible to completely recover the phase, which represents the cantilever shape.

Another, more promising way, to retrieve the phase is to use an additional reference beam as proposed in 1948 by Dennis Gabor [110]. Today, this method is known

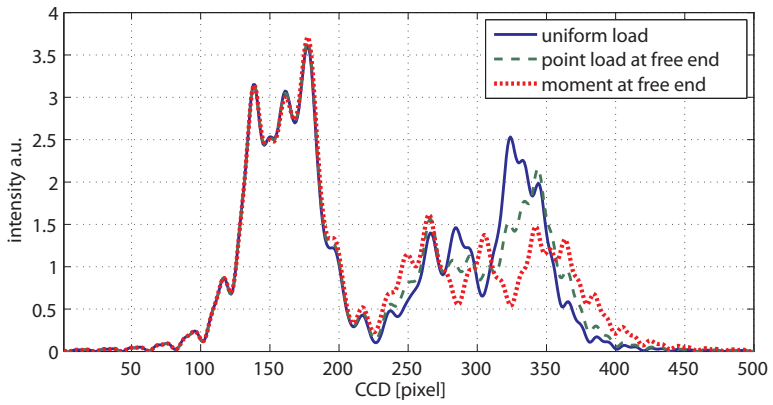


Figure 2.12: Simulating diffraction pattern for different cantilever bending profiles keeping the deflection $\Delta z$ constant.

as Holography. Methods involving interference of a measuring wave with a reference wave have already been presented in Sec. 1.2.4.2. Looking at the schematic for the simulation (Fig. 1.14) it is clear that the reflected beam can be thought of as consisting of two parts. First, the part which is reflected from the extended chip base and the chip body acts as a reference beam since it is not changed when the cantilever bends. Second, the part which is reflected from the cantilever acts as the measuring beam, containing the information about the cantilever surface profile. Both beams interfere with each other and it should be possible to develop an algorithm which can extract the full shape of the cantilever surface.

That different bending profiles of the cantilever lead to different diffraction pattern is shown in the following. A simulation of the three bending profiles mentioned in Appendix C with the same deflection of $\Delta z = -1\,\mu$m is presented in Fig. 2.12. The reference peak which is generated mainly from waves which were diffracted from the chip base, is almost the same for all three cases. The width of the pattern increases with increasing maximum slope of the bending profile (for the slopes see Fig. C.1). The main point is, that the diffraction pattern for different bending profiles but the same $\Delta z$ are distinguishable.

## 2.7 Conclusion

Different methods which can be used to determine the bending of the cantilever have been simulated here. In transmission mode, the diffraction patterns do not exhibit characteristics which could be exploited to distinguish between tilting and bending. It can also be seen by comparing Fig. 2.7 with Fig. 2.10, that the resolution for transmission mode is expected to be inferior to reflection mode. Reflection mode has the additional advantage of allowing to measure tilt and bending individually even when they occur simultaneously.

# 3

# Engineering and Experimental Methods

The diffractive optical readout made it necessary to a build a completely new setup which was flexible enough to be used for reflection and transmission mode experiments.

This chapter is dedicated to the description of the newly developed experimental setup and its parts. A schematic overview displaying all parts of the experiment can be seen in Fig. 3.1. The test solutions shown in the upper left corner are selected by the valve which can be computer controlled and the flow is driven by gravity through the flow cell into the waste container. The cantilever array chip is mounted vertically in the flow cell and the bending of the cantilever which depends on its coating and the test solutions used can be monitored in two different ways.

On the right side of the flow cell the optical lever readout (described in Sec. 1.2.4.1) is used with $\mathrm{Laser_{OL}}$ and $\mathrm{CCD_{OL}}$. Lenses for focusing the laser beam to a small spot on the cantilever underside have been omitted in the drawing for reasons of clarity but are explained below separately. The spot position on $\mathrm{CCD_{OL}}$ is analysed with software written in LabView (version 8.2) running on the connected PC. On the left side the diffractive readout is realised with $\mathrm{Laser_D}$ and $\mathrm{CCD_D}$. Again, the cylindrical lens used for shaping the laser beam was omitted from the drawing for reasons of clarity. For reflection mode it is important to position the CCDs in such a way that the laser from the opposite side of the cantilever does not shine directly into the

CCD. For this reason the two lasers are facing each other. The same is true for the CCDs.

The Peltier positioned behind the cell is controlled by an external PID controller which is connected to the PC. The goniometer and the xyz-stage were mainly used to position the chip or to study the behaviour of the diffraction pattern as a function of tilt. If several cantilevers had to be measured the xyz-stage was used to position them in the laser beam alternately.

Described above and shown in Fig. 3.1 is the diffractive readout in reflection mode. For transmission mode, the optical lever readout was located in front of the cantilever together with $\text{Laser}_\text{D}$ whereas $\text{CCD}_\text{D}$ was moved behind the cantilever (i.e. on the right side of the cell in the drawing).

## 3.1 Flow Cell

Experiments using cantilever chips as sensors can be carried out in gaseous and liquid environment and a new flow cell had to be designed allowing both. Much of the design is similar to the flow cell that was delivered with the Scentris™ instrument, a cantilever sensor system manufactured by Veeco (Santa Barbara, CA, USA). The major change is the additional back window to facilitate a beam transmitted through the cantilever to leave the flow cell on the back side.

A photograph of the fluid cell is shown in Fig. 3.2. The electric leads on the left side supply the peltier with power and on the right side the inlet (lower tubing) and the outlet (upper tubing) for gases or fluids can be seen. A chip is mounted in the chamber and clamped into position with a spring clip which is also visible. The flow cell itself is completely made out of stainless steel and the green colour in the photograph stems from a coating that was applied to reduce scattering of the laser. This was later removed because it was found to be bio-incompatible. All parts of the cell are shown in the assembly drawing Fig. E.1 and the drawings for each part can be found in the Appendix from page 170 onwards or as AutoCAD® and PDF files on the DVD accompanying this thesis. The main part is the body of the flow cell.

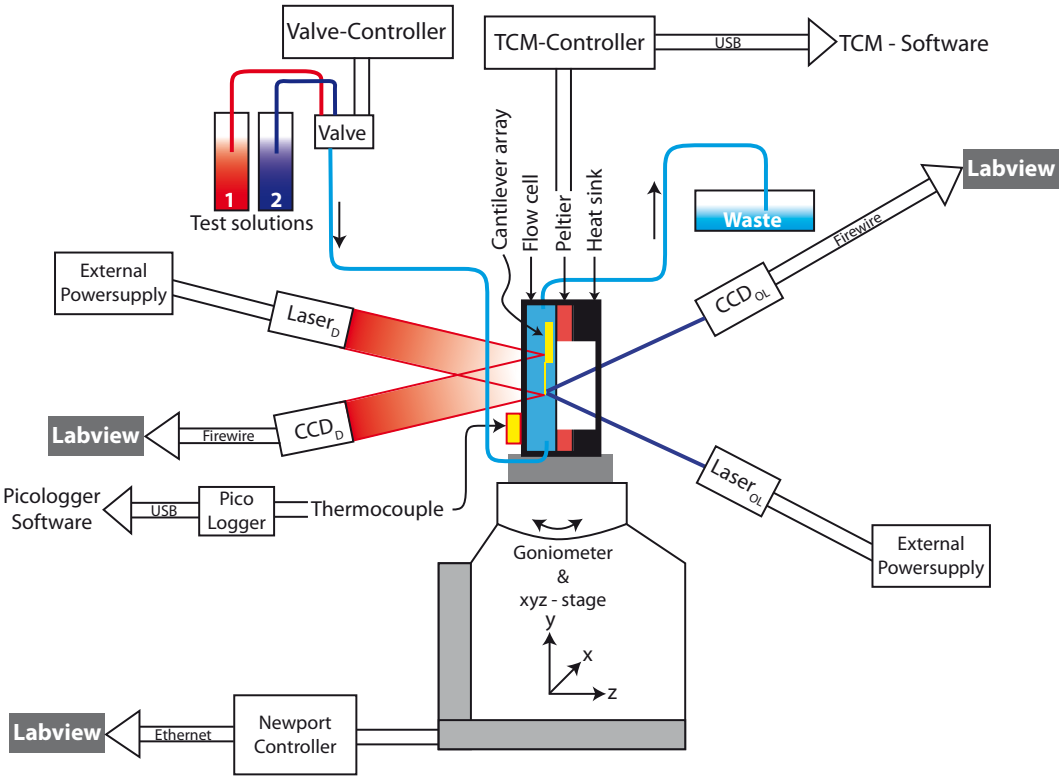


Figure 3.1: Schematic figure of experimental setup. The cantilever is mounted vertically in the flow cell. Test solutions 1 and 2 are selected by the valve and driven through the cell into the waste by gravity flow. On the right side, the optical lever technique is used to read out the cantilever bending and on the left side is the new diffractive readout in reflection mode. Goniometer, xyz-stage, CCDs are controlled by one LabView (version 8.2) program. The TCM controller for the Peltier module and the pico-logger for the external thermocouple were controlled by two separate programs.

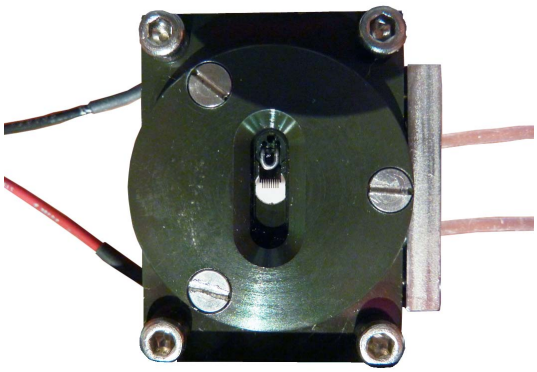

Figure 3.2: Photo of the flow cell. The power supply for the peltier element located behind the flow cell can be seen on the left and the inlet and outlet for the test solutions or gases are visible on the right side.

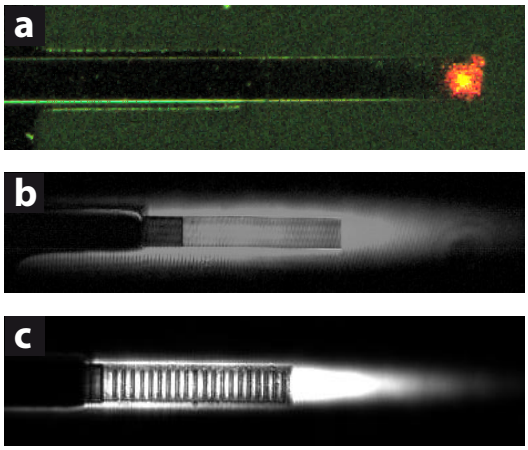


Figure 3.3: (a) Reflection of laser at the free end of the cantilever for conventional optical lever technique. (b) Laser to illuminate the entire cantilever for diffractive measurement on non-patterned cantilever and (c) for patterned cantilever. (b) and (c) are recorded in transmission.

It contains the channels for fluids and gases and all the other parts are attached to it. The Peltier element is clamped between the back of the main body and the heat sink.

## 3.2 Optics

### 3.2.1 Optical Lever Technique

The Premier Laser Diode Module (Edmund Optics, UK) was used with a wavelength of 655 nm. The power of the laser could be set from 0-5 mW by applying a voltage from 0 to 1 Volt to a control input which was usually set to 0.1 Volt. To achieve the desired laser spot on the cantilever, the inbuilt optics were replaced by the following setup of lenses. An inverted microscope objective was placed 9 mm away from the laser diode to collimate the beam and a lens with a focal length of 250 mm focused the beam to a spot shining onto the cantilever surface (see Fig. 3.3a). The incident angle of the beam is ≈30 deg to the surface normal of the cantilever. The reflected laser beam then travels through a lens positioned at distance from the cantilever equal to its focal length of 50 mm before it is recorded using a CCD camera (DFK-31 AF03, Imaging Source/Germany).

### 3.2.2 New Reflective/Transmissive Diffraction Technique

The optics needed for the diffractive measurement technique comprise a single cylindrical lens transforming the spherical laser beam into an elliptical shape to illuminate one cantilever entirely but omitting neighbouring cantilevers. The laser source used was a Helium-Neon laser (HRR050, Thorlabs Inc., UK) with the output power fixed at 5 mW. The laser power was regulated using neutral density filters in the beam line to avoid damaging the CCD camera which was used to record the diffraction pattern (ORCA-AG from Hamamatsu, UK). The illumination of non-patterned and patterned cantilever displayed in Fig. 3.3b-c shows the intensity after transmission through the cantilever.

## 3.3 Stage

Testing the robustness of a readout technique accurately needs a stage which can move and rotate the cantilever array in a very controlled way. Therefore, the flow cell which holds the cantilever array was mounted on a stage consisting of two goniometers on an xyz-stage (see Fig. 3.1). All five axes are computer controlled and allowed for a defined manipulation of the cantilever chip position.

### 3.3.1 Test of Linear Stages

Each single axis of the xyz-stage was calibrated on its own by the supplier, Newport. After assembling them the accuracy was checked using a Michelson interferometer (Fig. 3.4). Each linear axis has a travel range from -12.5 mm to +12.5 mm and the accuracy was checked at the positions -10 mm, 0 mm and +10 mm. The movable mirror 2 as shown in Fig. 3.4 was placed on the xyz-stage. The collimated laser is split by the beam splitter and reflected by the two mirrors which were slightly tilted in respect to the incoming beam to produce a stripe pattern on the CCD from the two interfering beams. Moving mirror 2 by half the wavelength of the laser ($\lambda/2 = 632.8\,\text{nm}/2 = 316.4\,\text{nm}$) will show one cycle of intensity change on the CCD since the wave has to travel the distance between the beam splitter and mirror 2

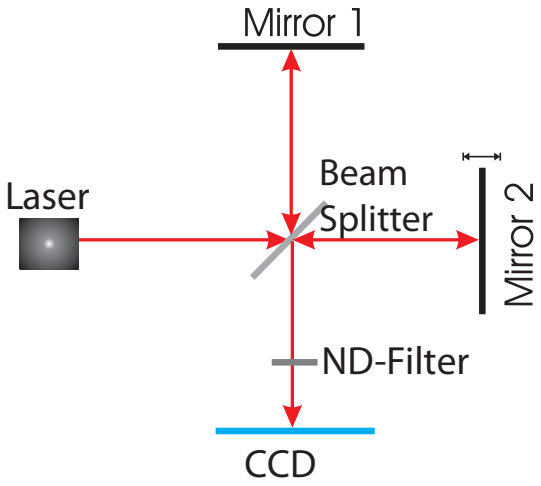


Figure 3.4: Michelson interferometer

twice. In the test the stage was moved a distance 2.5 $\mu$m in 10 nm steps in one direction and the position from the encoder was recorded together with the corresponding interference pattern.

The intensity changes at one pixel on the CCD are shown in Fig. 3.5. If the stage is working perfectly the distance between two maxima should be identical to $\lambda/2$. The results of analysing the intensity changes for each axis and at different positions can be seen in Table 3.1. The error is the standard deviation of at least 10 measurements.

| | pos: -10 mm | pos: 0 mm | pos: 10 mm |
|---|---|---|---|
| x-axis (group 4) | 337 nm ± 10 nm | 320 nm ± 7 nm | 309 nm ± 7 nm |
| y-axis (group 5) | 310 nm ± 24 nm | 273 nm ± 40 nm | 299 nm ± 20 nm |
| z-axis (group 6) | 329 nm ± 6 nm | 337 nm ± 17 nm | 329 nm ± 9 nm |

Table 3.1: Accuracy of different axes of the stage

As mentioned above the expected distance was 316.4 nm leading to an accuracy of around 10%. It has to be noted that the measurement accuracy was limited by the stability of the interferometer. Therefore the accuracy does not represent the true values for the Newport stage but describes the accuracy of the interferometer setup.

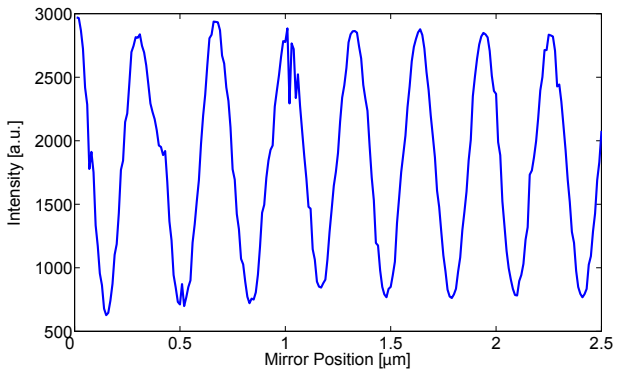


Figure 3.5: Intensity at a pixel on the CCD as a function of the position of mirror 2.

### 3.3.2 Calibration of the Goniometer

The input for the goniometer controller is in units of mm. Therefore a calibration has to be performed to find the factor that converts the length into the actual tilt angle it produces. The lower goniometer was calibrated by the optical lever technique described in subsection 1.2.4.1 on page 26 using a mirror mounted on the stage. Recording the position of the spot on the CCD together with the input to the controller yielded a calibration constant of:

$$C_{\text{gon}} = (8.20 \pm 0.05)\,\frac{\text{mrad}}{\text{mm}}$$

The error was calculated based on the propagation of the uncertainty from the measurement of the distance between mirror and CCD. According to the catalogue of the manufacturer (Newport Corp.) the constant should be $(8.06 \pm 0.02)$ mrad/mm.

## 3.4 Chemistry, Coatings and Solutions

**Buffer Solution** 0.1 M mono-basic and 0.1 M di-basic sodium phosphate salts (Sigma-Aldrich, U.K.) were dissolved in ultra pure water (16-18 MΩ·cm, Millipore Co., MA, U.S.A.) to reach pH 7.4. Before using the buffer in the experiments it was filtered using 0.2 $\mu$m filters (Millipore), ultrasonicated for 5-10 mins at room temperature, and purged with argon to remove any gas bubbles [1].

10 $\mu$M of human serum albumin (HSA) was added to the buffer for all vancomycin experiments presented in this thesis. While it obviously enhances the biological relevance of the experiments, it also has the beneficial side effect of reducing the drift. This is the case because HSA sticks to the non-coated underside of the cantilever and therefore prevents unspecific reaction occurring on the underside which are thought to be the cause of the drift.

**Vancomycin Solution** Vancomycin hydrochloride (Sigma-Aldrich, U.K.) was dissolved in buffer solution to yield 10 $\mu$M vancomycin preparation.

**D*Ala* and *PEG*** For the experiment presented in chapter 5 the cantilevers were coated with the glycopeptide Lysine-D-Alanine-D-Alanine or with triethylene glycol. D*Ala* is used to mimic parts of a bacterial cell wall of a vancomycin susceptible bacteria [111, 112, 12] and *PEG* is reported to resists biomolecule absorption on surfaces [113, 114].

In order to adsorb D*Ala* and *PEG* in form of a monolayer on top of the gold coated cantilever a thiol linker has to be attached to each biomolecule resulting in the following chemical form:

- for Lysine-D-Alanine-D-Alanine:
  $HS(CH_2)_{11}(OCH_2CH_2)_3O(CH_2)(CO)NH(CH_2)_5$(CO)-L-Lys-($\epsilon$-Ac)-D-Ala-D-Ala
  (sourced from Targanta Therapeutics, Cambridge, MA, U.S.A, 1 $\mu$M solution)
  will be referred to as D*Ala* in the following

- for triethylene glycol: $HS(CH_2)_{11}(OCH_2CH_2)_3OH$
  (sourced from Zhou and Abell, Dept. of Chemistry, Cambridge University, U.K.)
  will be referred to as *PEG* in the following

Their structures are shown in Fig. 3.6. (Details about vancomycin and its use in fighting the super bug MRSA (Methicillin-Resistant Staphylococcus Aureus) have

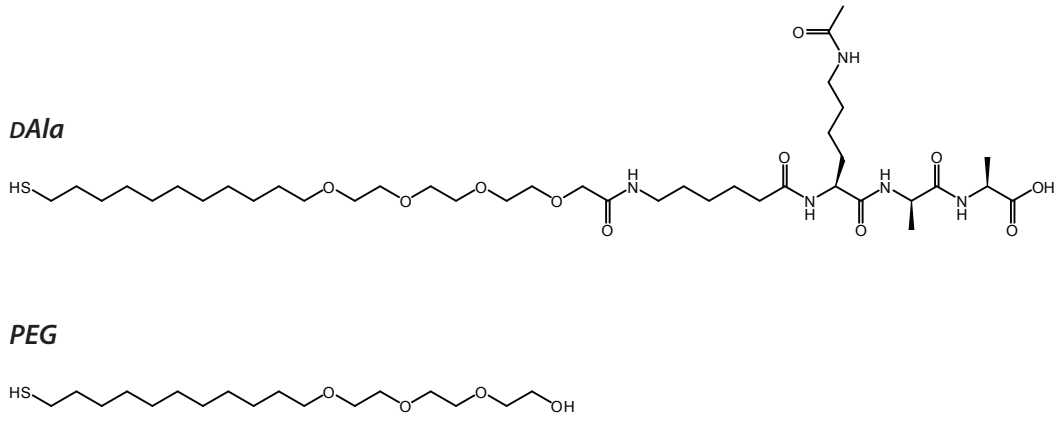


Figure 3.6: Chemical Structures of mucopeptide analogues used to coat cantilevers for the drug-target interaction stress measurements. D*Ala* represents VSE phenotypes *PEG* was used as a reference (figure adapted from [53]).

been published by Dudley Williams in [111] and can also be found in the PhD-Thesis of Alejandra Donoso Barrera [70].)

## 3.5 Cantilever Chips

The chips used throughout the experiments contain arrays of eight silicon cantilevers (Fig.3.7) fabricated by IBM Rüschlikon Research Laboratories in Switzerland. Each cantilever is 500 $\mu$m long, 100 $\mu$m and 0.9 $\mu$m thick (see Fig. 3.8) having a spring constant of 0.02 N/m.

### 3.5.1 Preparation of Cantilevers

#### 3.5.1.1 Cleaning

Before evaporating the cantilevers they were thoroughly cleaned for 20 minutes in a freshly prepared piranha solution with the ratio of 1 $H_2SO_4$:1 $H_2O_2$. They were then rinsed with deionised water (conductivity $\approx$18.2 M$\Omega$·cm). After a second rinsing step, this time with pure ethanol (ACS reagent, $\geq$99.5% from Sigma-Aldrich, cat.no. 459836), they were dried on a heating plate at a temperature of 75°C.

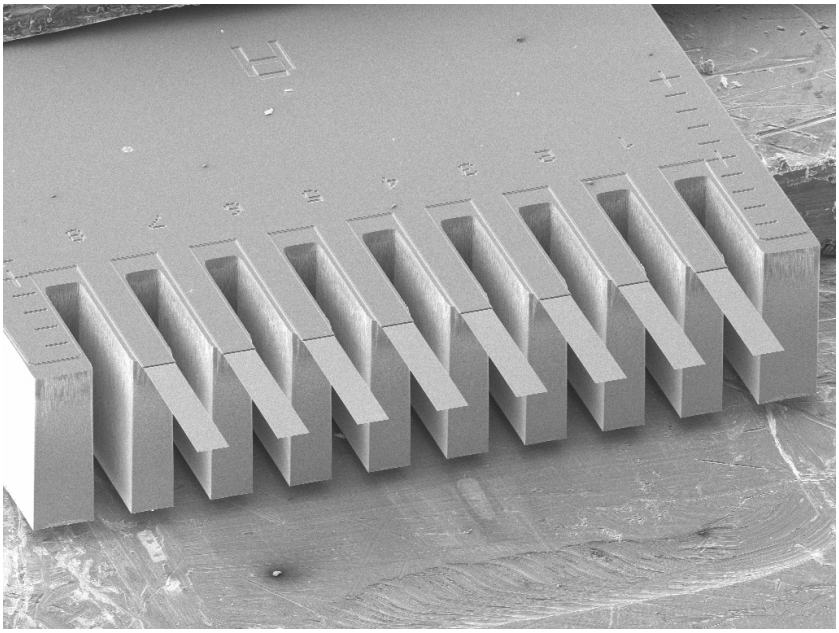

Figure 3.7: SEM-Image of one of our cantilever arrays taken with the Carl Zeiss XB1540 before using the focused ion beam to manipulate the cantilevers.

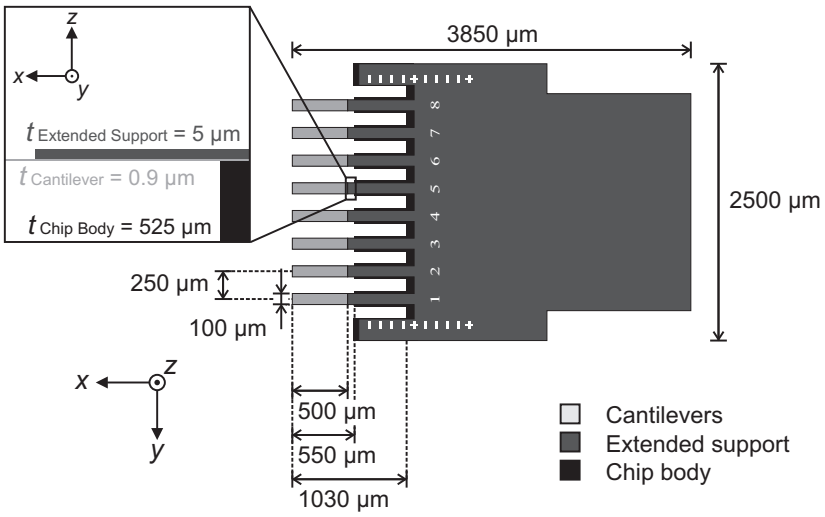


Figure 3.8: Dimensions of IBM cantilever chips (from [1])

Now the cantilevers were ready to be loaded into the vacuum chamber of the evaporator.

#### 3.5.1.2 Evaporation

The cantilevers were evaporated in the Auto 500 E-Beam evaporator from BOC/Edwards. The base pressure before evaporation was always below $1 \cdot 10^{-6}$ mbar. First a 2 nm thick layer of titanium was evaporated at a rate of ≈0.03 nm/s using an electron-beam (e-beam) current of 22 mA at 10 kV. The titanium acts as an adhesion layer for the 20 nm gold layer which was evaporated at a rate of ≈0.07 nm/s using an e-beam current of 30 mA at 10kV. The rate achieved at a set current can vary from time to time depending on the target material the e-beam is impinging on and the pattern and speed the e-beam sweeps over it.

#### 3.5.1.3 Patterning with FIB

A focused ion beam (FIB) is an excellent tool for prototyping on the nano scale and has been used successfully for fabrication or modification of cantilevers [68, 115, 116]. For a series of measurements in transmission mode the cantilever needed to be modified to resemble a diffraction grating. This has the advantage of diffracting more intensity of the laser light to higher angles where the change of the diffraction pattern upon bending of the cantilevers is more pronounced, thus improving the signal to noise ratio.

As a rule of thumb the FIB milling time needed can be calculated with the following formula [117]:

$$\text{mill time [s]} = \frac{\text{volume } (\mu\text{m}^3)}{\text{beam current } (\text{nA}) \times \text{volume deposition yield } (\mu\text{m}^3/\text{nC})} \tag{3.1}$$

Using gases can further shorten the milling time. The volume deposition yield can be found in table 3.2.

In the first tests I milled holes through the metal coating and the entire thickness of the cantilever. Using a beam current of 2 nA, 8-10 milling layers, 25 s milling

| Gas | Yield $(\mu m^3/nC)$ | Enhancement |
|---|---|---|
| | 0.4 | - |
| Iodine | 0.8 | 2 |
| $XeF_2$ | 1.7 | 4.2 |
| Oxygen | 1.8 | 4.5 |

Table 3.2: Enhancement of milling time due to injection of gas [117]

time per layer (i.e. a total milling time of about 200-250 s) and injecting fluorine gas at the same time the holes could be milled without inducing too much cantilever bending. It was found that the milling time was not consistent throughout all milling runs but varied by a factor of four to five. Most likely the reason for this is, that the distance of the gas nozzle from the milling spot was not kept constant between different runs. It has been shown by Li and Warburton that changing the position of the gas nozzle in respect to the milling region can change deposition rates by a factor of four [118]. The enhancement rates for milling using different gases vary by a factor of 4 (see Tbl. 3.2) which also supports the assumption that the major cause for varying milling rates comes from the position of the gas nozzle. Therefore the rule of thumb (Eq. 3.1) and the milling rates presented here should only be used as rough guidelines.

The result from the first milling is shown in Fig. 3.9. The dimensions of the 4 holes in lever 1 are 10x10 $\mu m^2$ with a spacing of 100 $\mu$m, lever 3 was cut down to a length of 100 $\mu$m, on lever 5 is a sequence of 10 holes 20x10 $\mu m^2$ with a spacing of 50 $\mu$m and cantilever 8 was cut to a length of 120 $\mu$m with two holes of the dimension 30x10 $\mu m^2$ and spacing of 80 $\mu$m. These levers have not been used for further experiments but were used to test the possibility of manipulating cantilevers in a controlled way by FIB.

The bending that occurs sometimes while milling might be due to charging up or heating of the cantilever and is not always reversible. To avoid bending, longer milling steps can be carried out in a sequence of short mills interrupted by short breaks.

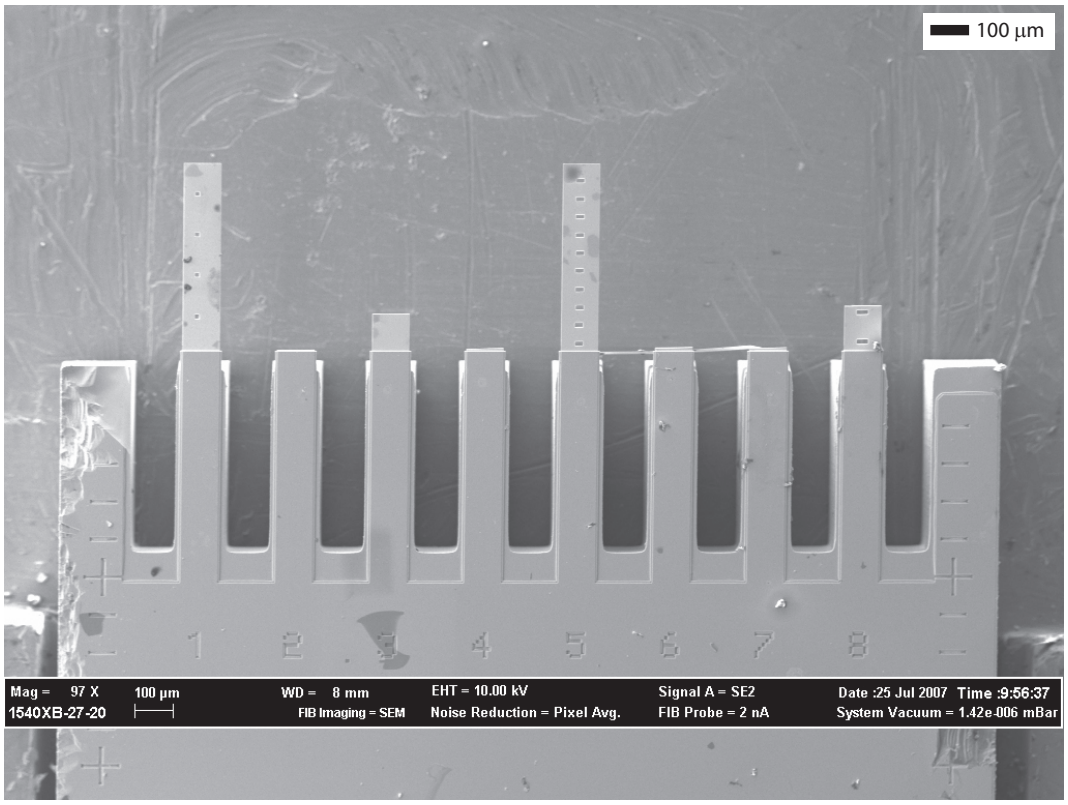


Figure 3.9: Holes milled through the metal coating and the cantilever using FIB. The width of the cantilever is 100 $\mu$m. The image was taken in SEM mode with conditions as shown on the text label.

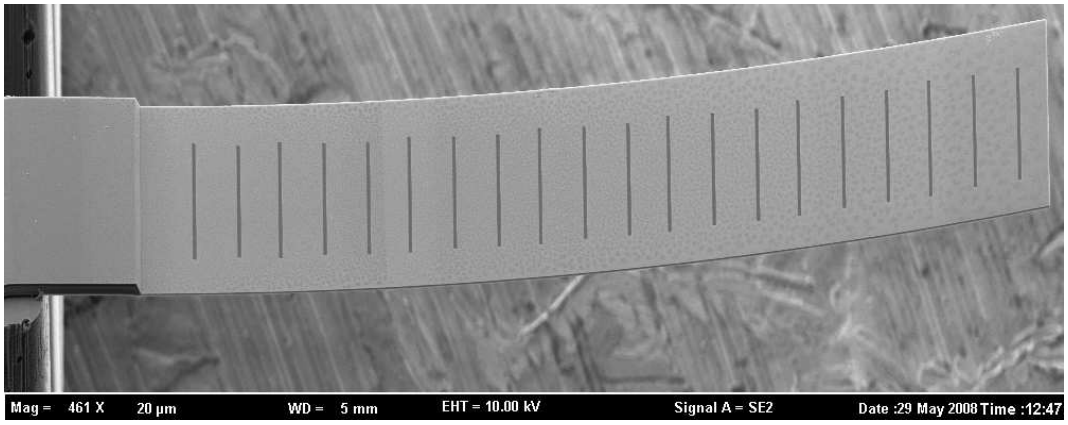


Figure 3.10: Diffraction grating embedded in the cantilever using FIB milling. The image was taken in SEM mode with conditions as shown on the text label.

It was found that in order to modify the optical properties of the cantilever and transform it into a diffraction grating it is enough to mill away only the metal coating. An additional milling through the silicon cantilever does not increase the contrast very much since silicon is quite transparent for the laser wavelength that was used. Its extinction coefficient is about 150 times lower when compared with gold or titanium (see further down). The cantilevers used for the transmission experiments have therefore been prepared by just milling away the metal coating and leaving the silicon part of the cantilever almost unchanged. This also keeps the material properties of the modified and non-modified cantilevers similar. The pattern milled onto the surface of the lever used for the transmission experiments consists of lines with the dimensions of 1.0x61.3 $\mu$m$^2$ and a spacing of 23.4 $\mu$m. The settings for the ion-beam were: current = 100 pA, 1 milling layer, time = 20 s.

The change of the optical properties on milling away the metal coating will be calculated in the next paragraph and used later as input for the simulation. The cantilevers prepared by FIB were not functionalised to be used as biosensors.

**Optical properties** Transmission coefficients $\tau_{\text{chip}}$ for the chip, $\tau_{\text{support}}$ for the extended cantilever support and $\tau_{\text{cantilever}}$ for the cantilever after the evaporation can be calculated using the extinction coefficients for the different materials and their thicknesses. The extinction coefficients $\kappa$ for silicon, titanium and gold are

$\kappa_{\mathrm{Si}} = 0.0195$, $\kappa_{\mathrm{Ti}} = 2.9344$ and $\kappa_{\mathrm{Au}} = 3.07$, respectively. Beer's Law ([119] p.302)

$$\tau = \exp\left[-\frac{4\pi}{\lambda}\int_0^{t'} \kappa\left(z'\right)\,\mathrm{d}z\right]$$

with $\kappa\left(z'\right)$ representing the extinction coefficient depending on the coordinate $z'$ and the thickness of the layer $t'$ is used to calculate the transmission coefficients $\tau$:

$$\tau_{\mathrm{chip}} = \exp\left[-\frac{4\pi}{632.8\,\mathrm{nm}}\left\{525\,\mu\mathrm{m}\cdot 0.0195 + 2\,\mathrm{nm}\cdot 2.9344 + 20\,\mathrm{nm}\cdot 3.07\right\}\right] \approx 0$$

$$\tau_{\mathrm{support}} = \exp\left[-\frac{4\pi}{632.8\,\mathrm{nm}}\left\{5.9\,\mu\mathrm{m}\cdot 0.0195 + 2\,\mathrm{nm}\cdot 2.9344 + 20\,\mathrm{nm}\cdot 3.07\right\}\right] \approx 0.03$$

$$\tau_{\mathrm{cantilever}} = \exp\left[-\frac{4\pi}{632.8\,\mathrm{nm}}\left\{0.9\,\mu\mathrm{m}\cdot 0.0195 + 2\,\mathrm{nm}\cdot 2.9344 + 20\,\mathrm{nm}\cdot 3.07\right\}\right] \approx 0.19$$

The transmission coefficient for the bare silicon cantilever is $\tau_{\mathrm{bare\_cantilever}} = 0.72$.

#### 3.5.1.4 Functionalisation

After cleaning and evaporation of the chips, the biological recognition layer was put down on the cantilever.

Adsorbing molecules to the gold coated cantilever surface has been done by linking them to thiols which then form a self assembled monolayer (SAM) on gold spontaneously [120]. The two different coatings needed for testing vancomycin are D *Ala* and *PEG* which was used as a reference.

The cantilevers are inserted into one end of the micro capillaries as shown in Fig. 3.11 and the solution containing a 2 mM ethanolic solution of *PEG* or 1$\mu$M D*Ala* is injected at the other end. Micro capillary forces drive the solution to the cantilevers and the time of incubation is 20 min to form a SAM. The cantilever chip is then rinsed again with ethanol before it is stored in deionised water, ready to be used for experiments.

An alternative way of functionalising only one side of the cantilevers is by using an ink jet spotting device which is usually run in a temperature and humidity controlled chamber [121].

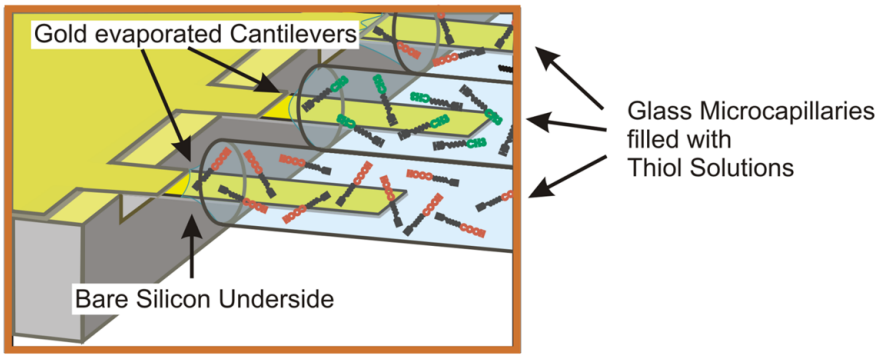


Figure 3.11: Functionalisation of cantilever via incubation inside micro capillaries [45]

# 4 Experiments

The simulation (chapter 2) gave insight into the potential of the different optical configurations. But it does not take into account all the perturbing influences such as stray light, imperfect laser beam and liquid measurement environment. Therefore an experimental setup was built (chapter 3). The objective of performing the experiments which are presented in this chapter was to have an experimental benchmark and comparison of the different measurement modes. The results from the simulation combined with the results from the experiment will enable to choose the right optical configuration for further optimisation.

The two different diffractive modes of measurement, namely reflection and transmission mode, were tested. Transmission mode measurements comprise experiments using patterned and non-patterned cantilevers and studying the diffraction pattern at different angular positions of the recording CCD. Reflection mode measurements were only performed with non-patterned cantilevers to study changes of the diffraction pattern in air and liquid.

The experimental results presented here directly compare the different realisations of the diffractive readout with the optical lever technique to find out whether the latter can be replaced by the former.

## 4.1 Transmission Mode

Although it was found with the simulation that the transmission mode is inferior in terms of resolution when compared to the reflection mode but it offers other advantages. Due to space restriction, sometimes it is more practical to use the readout in transmission mode rather than reflection mode. But the main advantage of the transmission mode is that it does not depend on a reflective surface. The only requirement for transmission mode to work is, that edges are present which generate the diffraction pattern (see Sec. 1.5.4 on page 41). This allows a much wider variety of surface coatings. It also allows to measure the deflection of cantilevers without an extra coating.

In transmission mode the laser illuminates the entire cantilever from one side and the diffraction pattern generated on the other side of the cantilever is recorded. For all experiments shown here the deflection of the free end of the cantilever was measured simultaneously with the conventional optical lever technique to allow for direct comparison. For the transmission mode measurements performed without liquid, the front and back window of the flow cell were removed to keep perturbing influences to a minimum.

### 4.1.1 Patterned Cantilever

The cantilever used for the experiments presented here is shown in Fig. 3.10 on page 84. The spatial periodicity of the holes is 23.4 $\mu$m. The two-dimensional diffraction pattern of this cantilever captured with a digital camera at $\approx 1.5$ m distance can be seen in Fig. 1.16 on page 44. A one-dimensional diffraction pattern with Bragg peaks from the -15$^{\text{th}}$ to the +15$^{\text{th}}$ order is presented here in Fig. 4.1. It was recorded by rotating the transmission CCD in a circle at distance of 190 mm around the cantilever chip in 1 deg steps, acquiring the diffraction pattern at each position, and combining them again, taking into account the different exposure times. The asymmetry in the pattern stems firstly from the the fact that the extended support

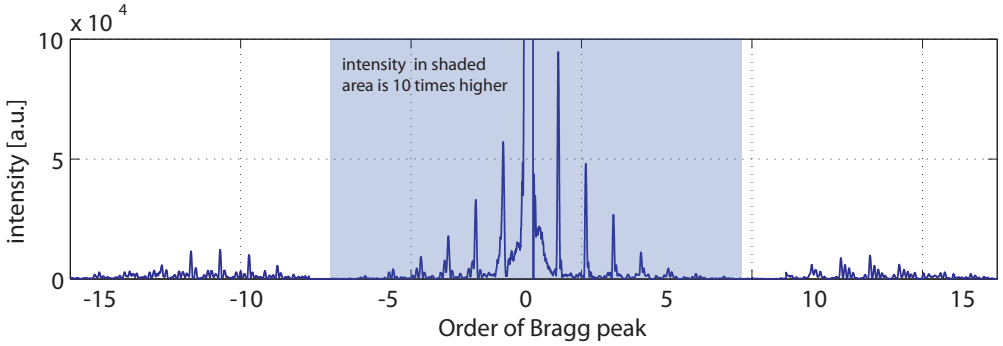


Figure 4.1: Diffraction pattern from -15$^{\text{th}}$ to +15$^{\text{th}}$ order. The intensity plotted in the shaded area has been displayed reduced by a factor 10 to increase the visibility of higher order Bragg peaks.

(see Fig. 3.8 on page 80) on one side of the cantilever is partially transparent and secondly from the milled diffraction grating which is not perfectly periodic.

#### 4.1.1.1 Tilting Experiment

The aim of this experiment is to test two claims made earlier in Sec. 2.4.1:

1. The change of the diffraction pattern in response to the tilt will increase as the order of the Bragg peak rises.

2. The diffraction pattern rotates in the opposite direction of the tilt rotation of the cantilever.

The goniometer upon which the flow cell is mounted was used to control the tilt of the cantilever chip. The influence of the tilt on the shift of the Bragg peaks from $-15^{\text{th}}$ to $15^{\text{th}}$ order was measured. In order to reduce the tilt error introduced through the backlash of the goniometer, care was taken that all positions were approached from the same direction, making the experimental procedure slightly more elaborate. First, the CCD mounted at a distance of 195 mm was moved to -28 degrees and then to -27 degrees and the goniometer was rotated to -17.4 mrad and then to 0 mrad. The diffraction pattern for the not tilted cantilever (at 0 mrad) was captured, and after tilting it with the goniometer by +1.34 mrad, a second pattern was captured. Now the CCD was moved to the next Bragg peak in the positive direction and the

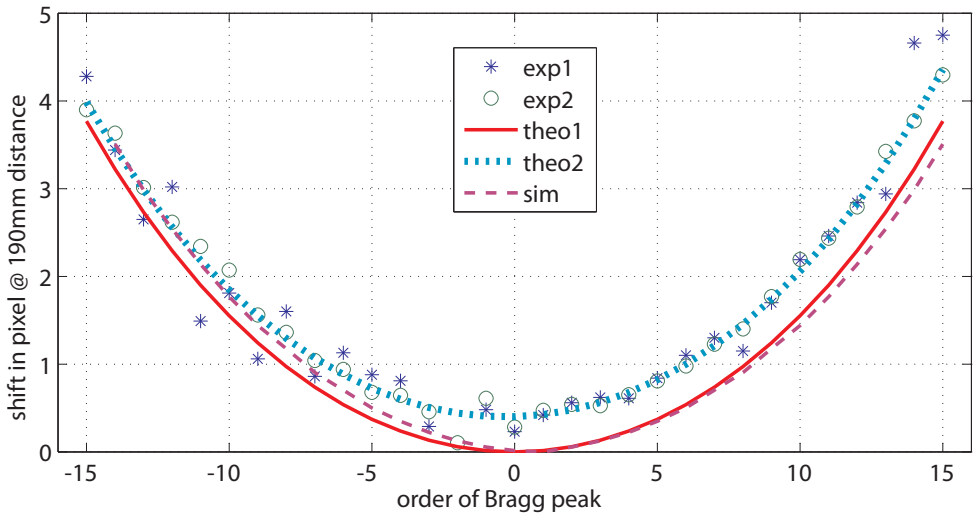


Figure 4.2: Peak shift as a function of the order of the Bragg peak. Comparing experimental results (exp 1, exp 2) with theoretical prediction for $\theta = 0$ (theo1) from Eq. 2.3 on page 59 and simulation (sim). Also plotted is a theoretical calculation for $\theta = 8.73\,\mathrm{mrad}$(theo2)

goniometer tilted first to -17.4 mrad and then to 0 mrad before recording the images for 0 mrad and +1.34 mrad tilt which is equivalent to a tilt of the cantilever with a deflection of its free end of 670 nm.

The theoretical shift of the Bragg peak $s_{Bp,m}$ has been calculated using Eq. 2.3 on page 59 for $\theta = 0$ (for notation see Sec. 2.4.2 on page 58):

$$s_{Bp,m} = \left( \frac{1}{\sqrt{1 - \left(\frac{m\lambda}{d}\right)^2}} - 1 \right) \mathrm{d}\theta \frac{\mathrm{CCD\_distance}}{\mathrm{pixel\_size}}$$

with $-15 \leq m \leq 15$, CCD_distance = 190 mm and pixel_size=6.54 $\mu$m.

The shifts of the Bragg peaks for two experiments have been determined and are plotted in Fig. 4.2 (stars and empty circles) together with the theoretical prediction $s_{Bp,m}$ (theo1) and results from a simulation (sim).

Experiment (exp1, exp2) , theory (theo1) and simulation (sim) almost agree, only two minor deviation can be observed from the experimental values exp1 and exp2:

1. The shift is not symmetric to the $0^{\mathrm{th}}$ order Bragg peak for exp1 and exp2. This is caused by the cantilever being tilted initially and not being perpendicular to

the incoming beam. The resulting asymmetry for slightly tilted cantilevers is also predicted by Eq. 2.3 on page 59.

2. The minimum of the shift does not go to zero for exp1 and exp2 as expected from the theory. Due to restrictions in the setup the cantilever hinge region could not exactly be placed at the centre of rotation of the goniometer which results in adding an offset to the shift.

Taking the two effects above into account, theoretical values have been calculated ($\theta = 8.73$ mrad, offset=0.4) which fit the experimental data better (theo2 in Fig. 4.2).

#### 4.1.1.2 Bending Experiments

In these temperature experiments, only gold coated cantilevers were used without an additional biochemical layer. The gold coating on top of the silicon imparts bimetallic properties on the cantilever. Heating or cooling will therefore change its bending. The temperature was recorded using a thermocouple which was attached to the front side of the flow cell. In the experiment shown here the temperature was cycled up and down (Fig. 4.3a) by switching the power supply for the peltier element on and off while recording the transmission diffraction pattern (Fig. 4.4a) as well as the deflection (Fig. 4.3b) of the free end of the cantilever with the optical lever technique. The direct response of the deflection to a change in temperature is shown in Fig. 4.3c.

The angle of observation for the transmission CCD was set to 29.5 degree to observe the $19^{\text{th}}$ order Bragg peak and subsidiary peaks. The distance between cantilever and CCD was 0.25 m. Changes in the diffraction pattern due to changes of the cantilever bending are minute, as has already been expected from the simulation. In order to examine the changes, a reference diffraction pattern for this experiment was chosen (Fig. 4.4a) and the difference to other diffraction patterns with a bending relative to the reference is plotted in Fig. 4.4b. A change in the diffraction pattern can be seen clearly in these plots even for a bending as low as 2.5 nm.

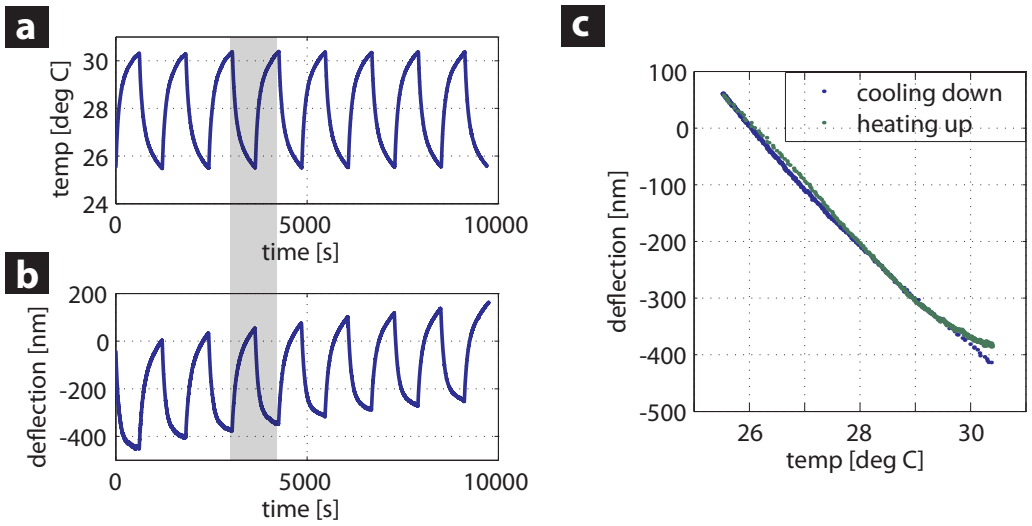


Figure 4.3: Response to temperature cycling. Measurements of temperature (a) and deflection (b) are shown. c) shows the direct response of the deflection to the temperature for the one cycle (shaded grey in a and b)

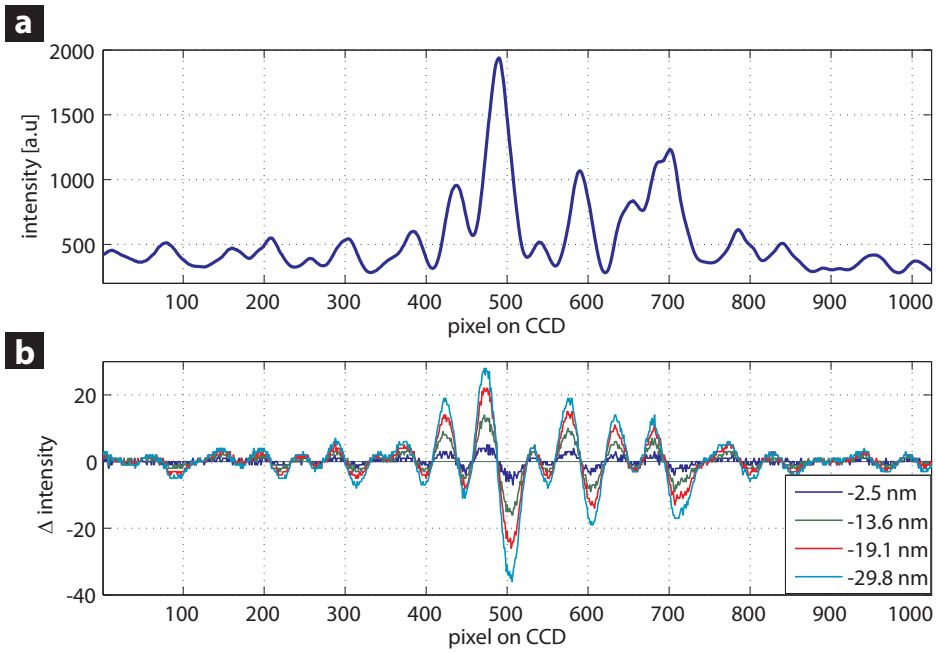


Figure 4.4: (a) Initial diffraction pattern showing the $19^{\text{th}}$ order Bragg peak and subsidiary peaks. (b) The difference of diffraction patterns to the initial pattern where the bending is relative to the initial bending.

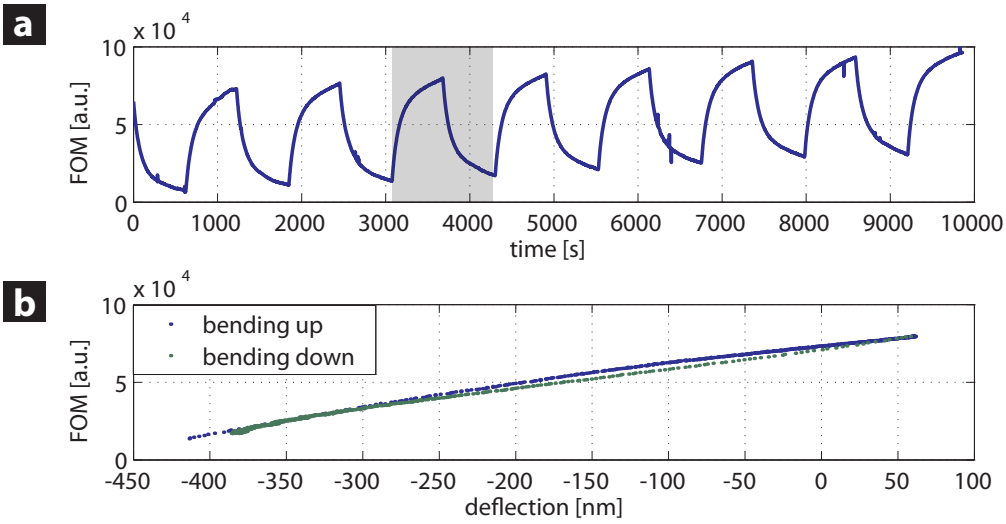


Figure 4.5: The response of the cantilever by cycling the temperature by $\approx \pm 5\,K$. a) Figure of merit ($FOM$) computed from diffraction pattern. (b) $FOM$ versus deflection for the cycle shaded in grey in a).

Analysing the difference of the diffraction pattern with the $FOM_k$ as defined in Eq. 2.4 on page 61 yields a curve similar to the cycling of the temperature or the deflection of the cantilever. The $FOM_k$ calculated in this way is shown in Fig. 4.5b.

Finally the $FOM_k$ is plotted against the deflection $\Delta z$ measured simultaneously with the optical lever technique (Fig. 4.5a). The observed hysteresis for the temperature cycle might be caused by the fact that in the heating up phase not only the cantilever is heated but the whole flow cell, including the clip that holds the cantilever chip in place. Heating up the clip causes the whole cantilever chip to tilt slightly in addition to the bimetallic effect of the individual cantilevers.

#### 4.1.1.3 Distinguish between Bending and Tilting

The previous two experiments have shown that it is possible to detect the tilting of the cantilever chip or the bending of a cantilever alone. However, is it possible to distinguish one from the other by analysing the transmission diffraction pattern?

To answer this question bending and tilting were performed in sequence, observing the $12^{\text{th}}$ and $13^{\text{th}}$ order diffraction peaks at a distance of 165 mm. It was hoped that the changes of two neighbouring Bragg peaks would give the information needed

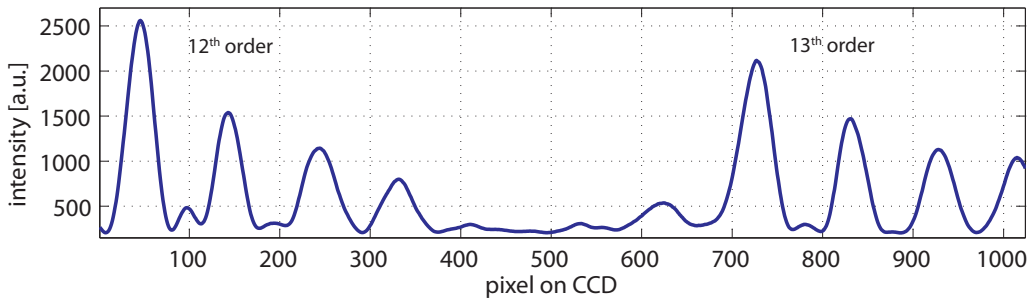


Figure 4.6: Diffraction pattern showing two Bragg peaks which are split up in multiple peaks due to the not perfectly periodic structure milled onto the cantilever. The split can also be caused by the common path interferometer effect which results from the partial transparency of the parts between the slits of the diffraction grating[122].

to distinguish between tilt and bending. First, the diffraction pattern for samples 1-17 was taken by increasing the tilt of the chip by +0.62 mrad for each sample and decreasing it by -0.62 mrad for sample numbers 18-33. In order to induce bending, the temperature was increased in +3 K steps (sample numbers 34-42) followed by -3 K steps for sample numbers 43-50.

The initial transmission diffraction pattern for sample number 1 is shown in Fig. 4.6. For an ideal strictly periodic structure (slits are fully transparent and the rest of the cantilever is fully opaque) a Bragg peak would not split into multiple peaks but remain as one. The partial transparency of the entire cantilever leads to the common path interferometer effect which causes the peaks to split [122].

All the different responses to tilts and changes in temperature are shown in Fig. 4.7. The responses to tilting (a, c, e, g) show almost no hysteresis whereas the responses to bending (b, d, f, h) exhibit small hysteresis. The is caused by the thermocouple and cantilever sensing the temperature at different positions. Furthermore, the thermocouple is attached to the metal of the flow cell whereas the cantilever is in air. Therefore, the cantilever cools down faster than the thermocouple.

The result of the optical lever technique is shown in Fig. 4.7a and b. It has to be remembered that the deflection $\Delta z$ of the cantilever is determined from inclination of the free end of the cantilever, i.e. the deflection of the laser beam is caused by a change of angle (see Fig. 1.7). The inclination angle of the free end of the cantilever

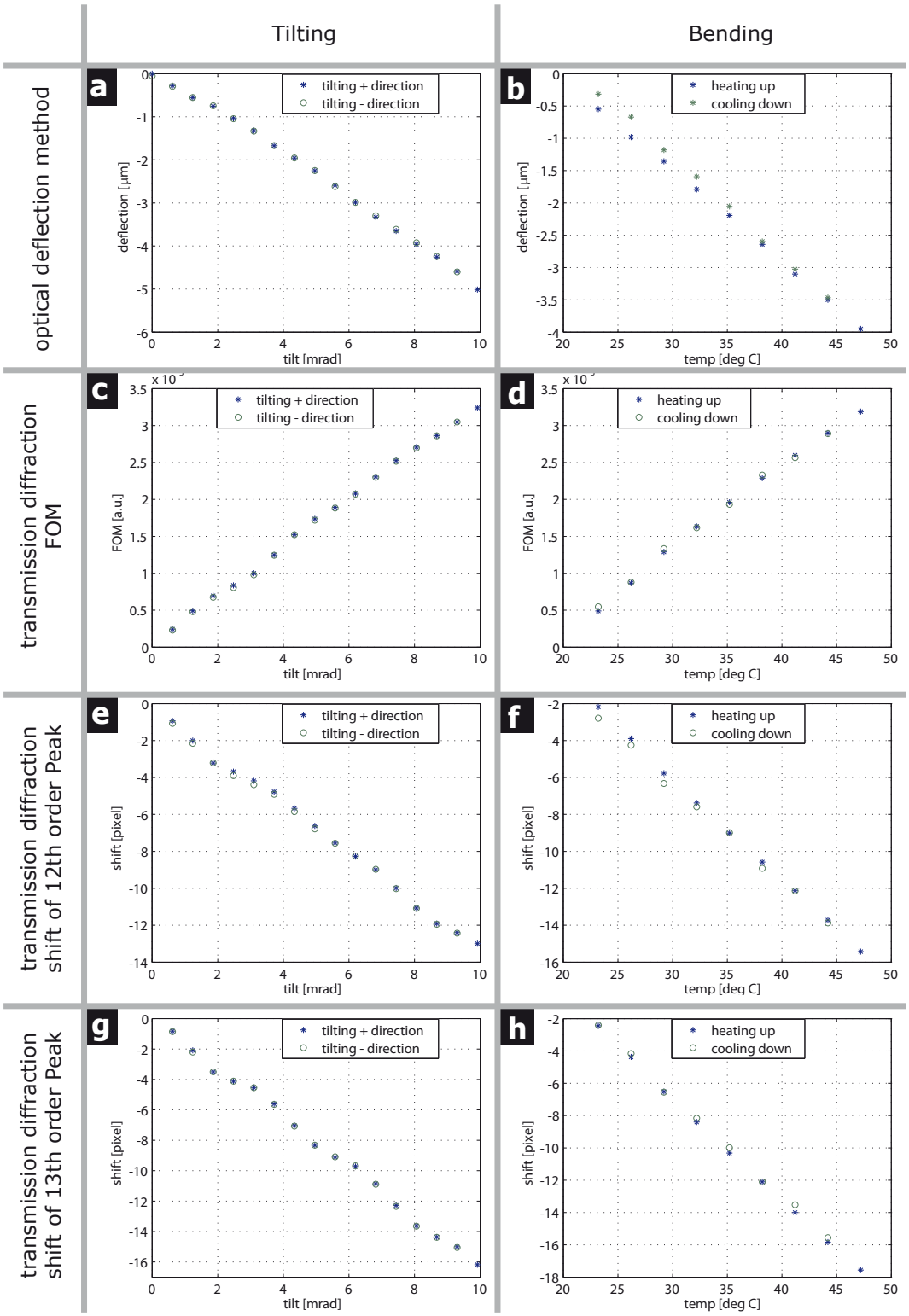


Figure 4.7: Responses measured to tilting the cantilever with the goniometer or bending it by changing temperature. Shown are the measurements for the optical deflection in a) and b), the *FOM* in c) and d), the shift of the 12th order Bragg peak in e) and f), and the shift of the 13th order Bragg peak in g) and h).

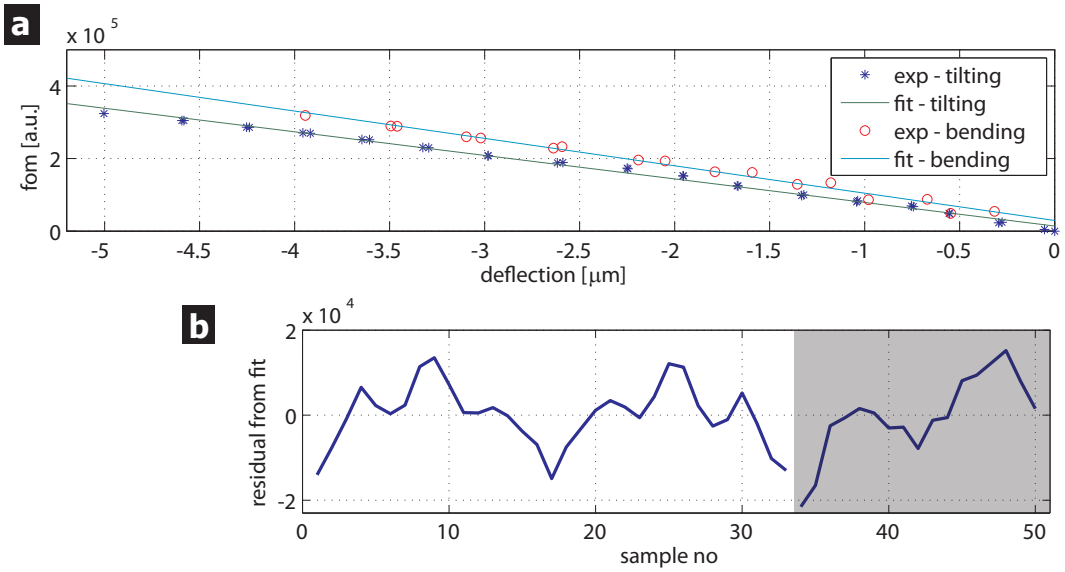


Figure 4.8: (a) Plot of $FOM$ against the deflection. (b) residues of the linear fit plotted against the sample number to see difference between tilt and bending. The shaded area in (b) labels the samples were the bending of the cantilever was changed. The non-shaded area labels the tilting.

is two times higher for bending than it is for tilting if the real deflection $\Delta z$ is the same. This is accounted for in the analysis. The response of the $FOM$ seems to be similar for tilting and bending (Fig. 4.7c and d). e-h show the response of the shift of the individual peaks at the $12^{\text{th}}$ and $13^{\text{th}}$ order Bragg peak position. As already seen previously, the response increases with the order of Bragg peak.

Looking at the $FOM$ extracted from the transmission experiment for tilting and bending separately, it seems that $FOM \propto \Delta z$, but with different proportionality constants for tilting and bending. Fitting a line to the $FOM$ depending on $\Delta z$ measured with the optical deflection technique confirms that the proportionality constant for bending is about 15% higher than for tilting as shown in (a) of Fig. 4.8. (b) shows the residuals of the fitting procedure which imply that the relation between $FOM$ and $\Delta z$ is not strictly linear.

It has to be concluded that the $FOM$ alone can not be used to distinguish between tilt and bending. But if the mode of surface change is known a priori, as it needs to be for the optical lever technique, than the $FOM$ can be used to quantify tilting and bending of the cantilever.

### 4.1.2 Non-Patterned Cantilever

Engraving a pattern in the cantilever modifies not only the mechanical properties of the cantilever but increases the complexity of cantilever fabrication. This section shows the feasibility of using non-patterned cantilevers but also brings to light its inferior resolution.

The non patterned cantilever is partially transparent and creates a diffraction pattern as described in Sec. 1.5.4 on page 41. Since a periodic structure is missing, the Bragg peaks are absent too but the fringes created from the finite length of the cantilever can still be observed at higher angles. The diffraction pattern shown and analysed for the non-patterned cantilever were captured at the same CCD position and with the same exposure times which were used for the experiments with the patterned cantilever above. This facilitates a direct comparison in terms of resolution. From Fig. 4.9a it is clear that the intensity of the peaks in the pattern is close to the background intensity ($\approx 200$ [a.u.]). Looking at the difference of the diffraction pattern (Fig. 4.9b) one sees that a bending in the range of 50 nm is needed to generate a visible change. The sensitivity using patterned cantilever is about 25 times higher (see Fig. 4.4). The $FOM$ in this case (Fig. 4.9d) does resemble the deflection measured with the conventional optical lever technique shown in Fig. 4.9c.

The responses to the temperature change are also shown in Fig. 4.10a and b. The thermocouple and cantilever are in different positions. The cantilever, surrounded by air, cools of more than the thermocouple, attached to the metal of the flow cell. This causes the hysteresis in the response curves a and b. The hysteresis vanishes almost completely when plotting the response of $FOM$ to the deflection measured (Fig. 4.10c).

### 4.1.3 Summary on Transmission Mode

The test experiments described above prove the feasibility of measuring bending or tilting of the cantilever with nanometre resolution. Since the shift of the peak was the predominant change in the diffraction pattern the resolution depends on

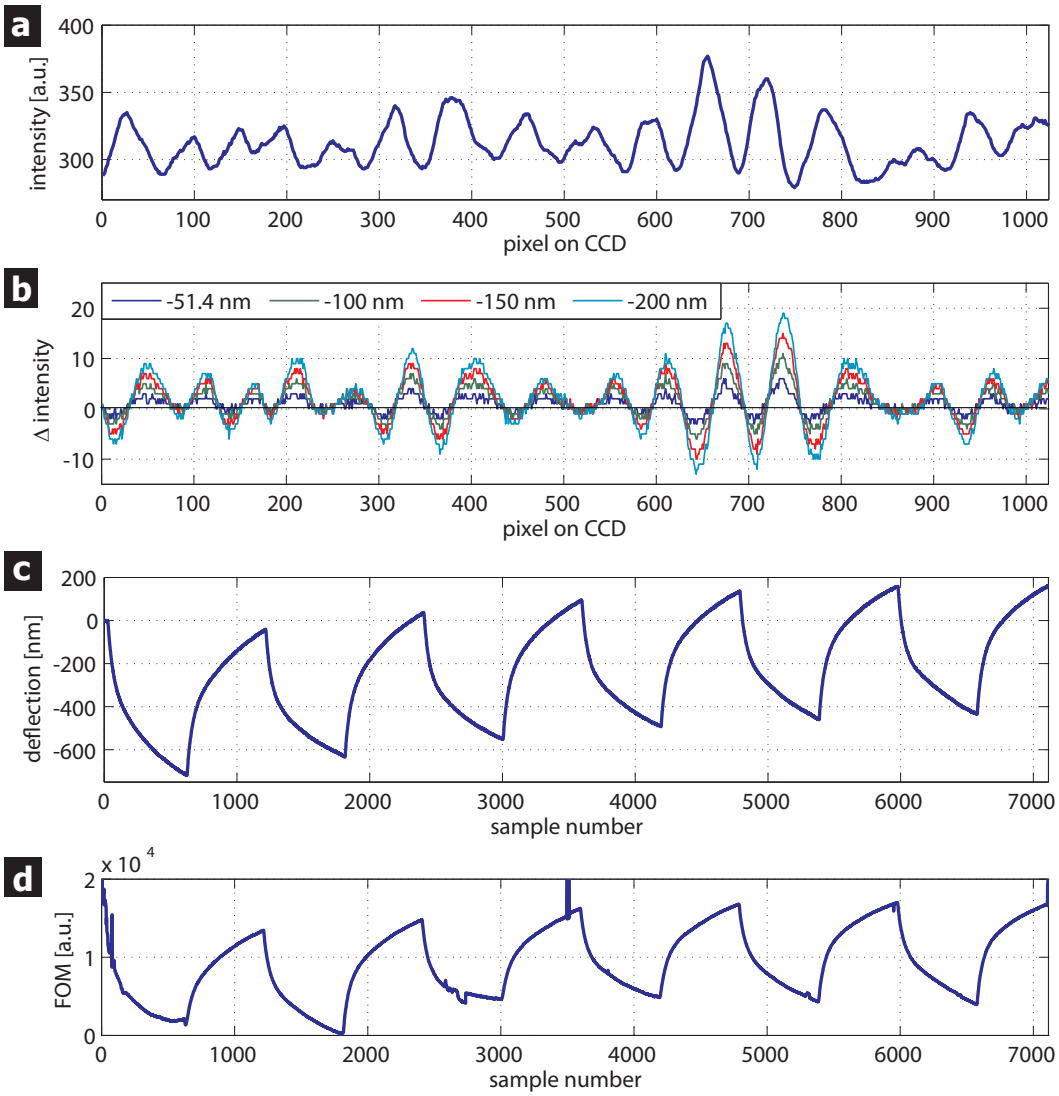


Figure 4.9: (a) Diffraction pattern of a non patterned cantilever in transmission mode recorded at an angle of 29.5 deg. (b) Difference of diffraction patterns with different bending of the cantilever. (c) Results from conventional optical deflection method. (d) Figure of merit $FOM$ calculated from transmission diffraction pattern

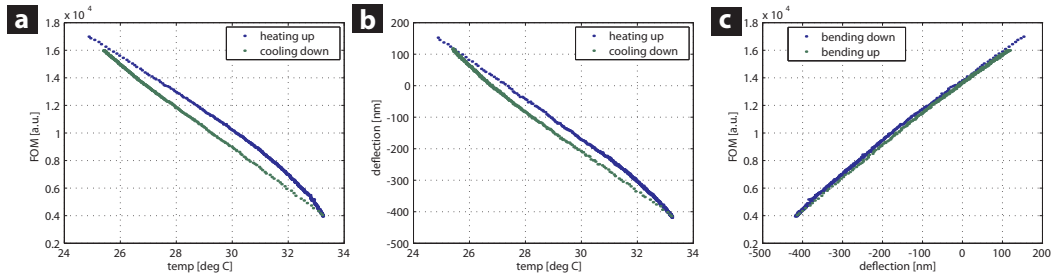


Figure 4.10: Response of $FOM$ (a) and deflection (b) to the heating of a non-patterned cantilever. (c) shows the direct response of $FOM$ to the deflection.

the distance of the recording CCD to the diffracting cantilever and on the angle of observation (i.e. higher order Bragg peaks). It is also advantageous to pattern the cantilever with a periodic diffracting structure because it maximises the amount of light diffracted to higher orders, thus improving the signal to noise ratio.

A feature that clearly distinguishes tilting and bending was not discovered. This might be due to the fact that changes in the transmission diffraction pattern are already quite small.

## 4.2 Reflection Mode

The experiments on transmission mode confirmed the finding from the simulation that it is not possibly to distinguish tilting from bending. To be able to make this distinction the simulations reflection mode measurements are needed. The objective to perform the experiments in reflection mode is to affirm the assumption that tilt and bending can be distinguished using reflection.

In this mode, the diffraction pattern is measured in reflection from the top side of the cantilever. The deflection of the cantilever is also measured with the optical lever technique with the laser being reflected from the underside of the cantilever. The following experiment was performed without liquid in the flow cell and the chip surface was partially illuminated in addition to the cantilever. The diffraction pattern was recorded using a CCD mounted at 100 mm distance. The cantilever chip was tilted with the goniometer and bending of the cantilever was induced by a change in temperature. As in the case for transmission, the one dimensional diffraction pattern is extracted from the two dimensional pattern at the position indicated by the dashed line in (a) of Fig. 4.11. The diffraction pattern for two different bendings of a cantilever are shown in (b) and for two different tilt angles in (c). These initial experimental results show the characteristics found earlier with the simulation (see Sec. 2.4.3.2 on page 64) which make it possible to distinguish between bending and tilting. The peak on the left of the diffraction pattern in Fig. 4.11b will be referred to as the reference peak in the following.

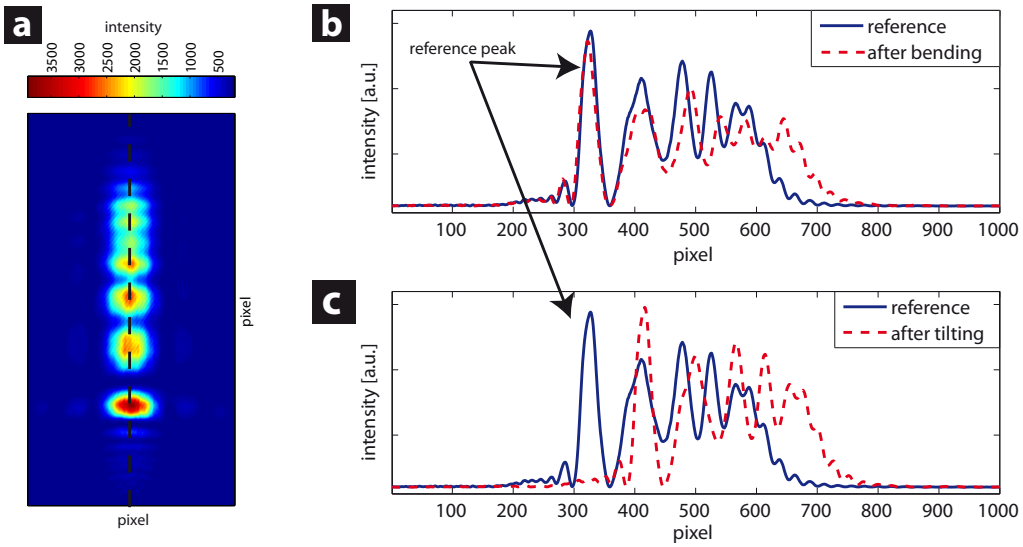


Figure 4.11: Effects of bending and tilting on the diffraction pattern from cantilever and chip base in reflection mode. (a) Two dimensional pattern for one state of bending. One dimensional pattern along the dashed line are shown for two different states of bending in (b) and tilting in (c).

To further test the capability to distinguish between tilting and bending, the following experiment was performed comprising three different phases. During the first phase the temperature was changed to induce bending only. In phase two the cantilever chip was tilted using the goniometer and keeping temperature changes to minimum. Finally, in the third phase the temperature was changed and the cantilever chip tilted at the same time. The deflection was measured with the reflective diffraction method the optical lever technique as an in-situ control. For the three phases, the changes of tilt through the goniometer and changes of bending through the Peltier element are shown in (a) of Fig. 4.12. The response measured with the conventional optical beam deflection method is shown in (b). The width and position of the diffracted peak have been extracted from the diffraction pattern and are shown in (c).

The conversion factors to translate the width to a deflection of the free end in units of nanometres and from the position to a tilting angle have been determined via the simulation. To do this, the simulation was initialised with the exact geometry of the experiment. By changing the deflection in the simulation and observing the

change in width of the diffraction pattern a conversion constant could be calculated which was then used in the analysis of the experiment.

Looking first at the optical deflection method shown in (b), it is apparent that the bending and tilting can be measured if occurring individually. But in order to determine the actual deflection the user needs to know a priori whether it is bending or tilting since the deflection of the cantilever is calculated based on the rotation of its free end. As mentioned above, the rotation of the free end is twice as big for the bending when compared with tilting of the same deflection $\Delta z$. In phase 3, when tilting and bending occur at the same time, it is impossible to distinguish between them since the measurement takes place only at one point of the cantilever.

Examining the diffraction pattern and extracting the width and position of the diffraction pattern yields the result shown in (c). The bending and tilting are determined correctly for phases 1 and 2 when both occur subsequently. But even when they occur simultaneously they can still be uncoupled and are measured correctly. It has to be noted that not only the relative bending but also the absolute can be recovered from the width of the diffraction pattern.

### 4.2.1 Reflective Diffraction Measurement in Liquid

After showing that the reflective diffraction technique could be used measuring in air, the results shown here prove that it can also be used with liquid in the flow cell. Another objective of this experiment is to show that parallelisation is possible with this readout.

After mounting a cantilever, the flow cell was filled with buffer solution. A power supply was directly connected to the Peltier element and set to a fixed current of 60 mA which results in a temperature change of 1.3 degrees Celsius after 20 min. Using the xyz-stage all 8 cantilevers were placed in the laser beam sequentially and their deflections recorded. Again, bending was measured simultaneously with the optical lever technique and the reflective diffraction technique for direct comparison.

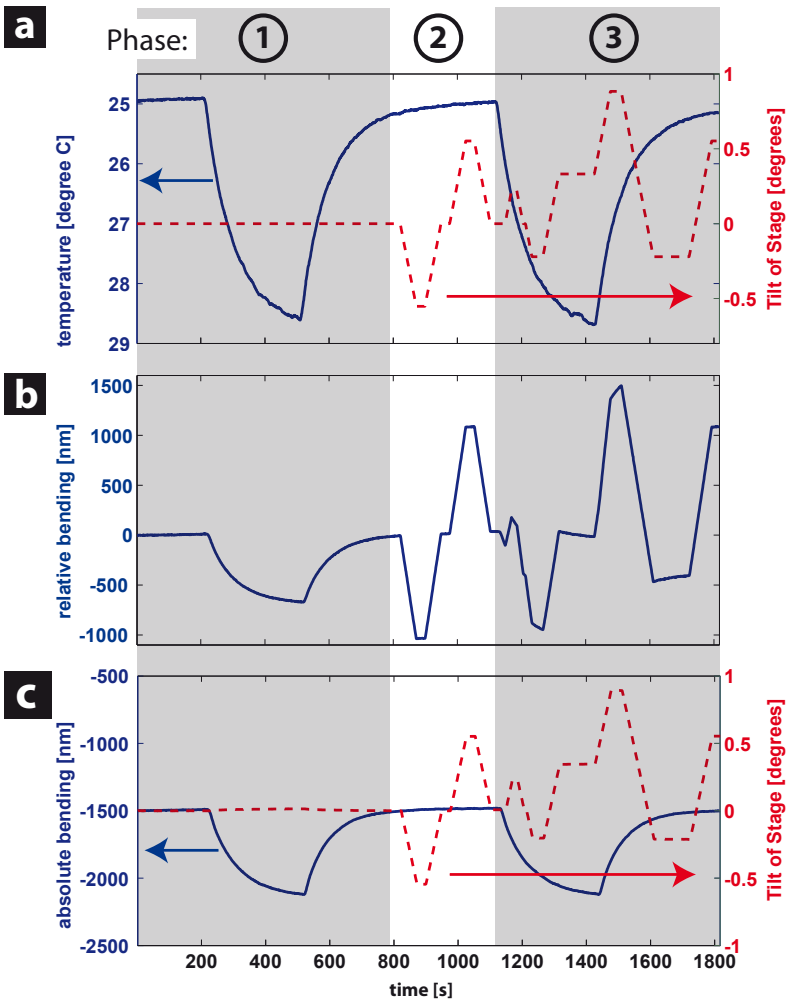


Figure 4.12: Comparison of optical lever technique with diffraction. Phase 1 shows bending only, phase 2 tilting only, and in phase 3 the cantilever is tilted and bent simultaneously. (a) shows the temperature and the angular position of the stage recorded as solid and dashed lines, respectively. (b) shows the bending signal of the cantilever measured with the optical beam deflection method, and (c) the bending and the tilt of the stage could be recovered independently from diffraction pattern plotted in solid and dashed line, respectively.

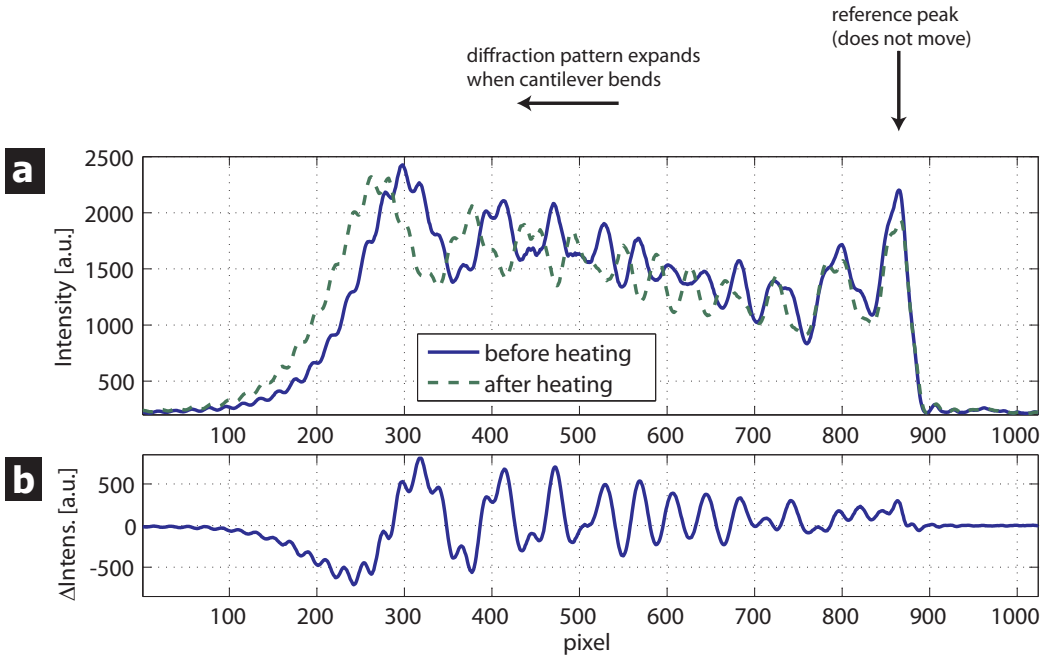


Figure 4.13: Results of testing the reflective diffraction technique in liquid. Illuminated is the cantilever and a part of the chip base. (a) Shown is a diffraction pattern taken before heating the chip (blue solid line) and after heating (green dashed line) by 1.3 degrees Celsius. In order to enhance the visibility of the changes between the two diffraction pattern, their difference is plotted in (b).

Two diffraction patterns representing the states of one cantilever before and after heating are shown in Fig. 4.13(a). If the cantilever bending increases, the diffraction pattern expands.

Fig. 4.14 shows the deflection measured simultaneously with the optical lever technique (a) and the reflective diffraction technique (b). Both measurements are in good agreement.

These experiments confirm that parallelisation is possible with the new diffractive reflection readout and that measurements in liquid can be performed with resolution comparable to the optical lever technique.

### 4.2.2 Concluding Remarks on the Reflection Mode Measurements

In reflection mode the fact has been exploited that the width of the diffraction peak is directly related to the bending of the cantilever for the given geometry. It can be

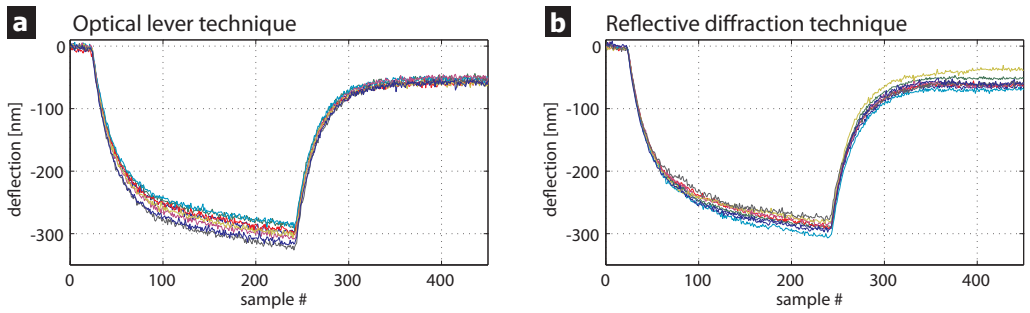


Figure 4.14: Changing the temperature by 1.3 degrees Celsius induced a bending of the cantilever of $-302\pm13$ nm measured with the optical lever technique (a) and $289\pm 9$ nm measured with the reflective diffraction technique (b). The deflection stated is the mean of the 8 cantilever deflections and the error is the standard deviation. The deviation is below 5%.

said, that the more the degree of bending, the wider the diffraction pattern. This has been observed in both simulation and experiment.

In order to get a reference peak in the diffraction peak which does not change position under bending but only under tilting, it is important that enough light is reflected from the chip base. Otherwise, the interference of the light coming from the bent cantilever will change the position of the reference peak. Using the simulation it has been found that a good reference for bending is achieved if the illuminated length of the chip base corresponds to the length of the cantilever. The IBM cantilever chips also exhibit a height difference between the chip base and the cantilever of 5 $\mu$m (Fig. 3.8 on page 80) which also helps to separate the reference peak from the rest of the diffraction pattern.

It should also be mentioned here that the cantilevers used in the experiments which are shown in this thesis were all bent initially from the fundamental asymmetry of the cantilevers coated on only one side. It increases when the cantilevers are functionalised with biomolecules. It has been observed that the bending can be either tensile or compressive, depending on the precise sample preparation conditions. Usually the initial deflection of the free end of the cantilever after evaporation is in the range of $-5\,\mu\text{m} \leq \Delta z \leq 5\,\mu\text{m}$. This initial bending helps to separate the reference peak from the peak resulting from the cantilever.

The other extreme which will cause problems occurs when the cantilevers are bent too much initially. If the bending exceeds $10\,\mu$m the recording diffraction pattern will become too wide, and the peak intensity reduces making it challenging either to capture the entire diffraction peak with the CCD or distinguish the diffraction peak from the noise. Using a converging lens will avoid the broad diffraction pattern being clipped by the finite size of the CCD chip but also reduces the resolution of the bending measurement. Alternatively, reducing the distance of the CCD to the cantilever can solve the problem too.

# 5

# Application - Detecting an Antibiotic

The aim of my research is to find a readout system which can take the successful cantilever biosensors out of university laboratories into pharmaceutical companies and hospitals. In the last chapter it was found that the reflective diffraction technique works in air and in liquid. This chapter presents a study of drug-target interaction involving the antibiotic vancomycin.

The last decades have witnessed a drastic decrease in the rate of discovery of new antibiotics [123]. At the same time it can be observed that through mutations, some of the bacteria become resistant to existing antibiotics. The most prominent examples, posing real challenges for hospitals, are the methicillin-resistant Staphylococcus aureus (MRSA) [111] and the vancomycin resistant Enterococci (VRE) [124].

Causes for the stagnation in the discovery of new potent antibiotics are manifold. They range from a lack of clearly defined standards by the Food and Drug Administration (FDA) [125] to absence of financial incentives for pharmaceutical companies [126]. But one of the main problems is the lack in chemical diversity of drug libraries combined with lack of physical tools to study antibiotics, particularly on the outer cell wall surface of bacteria - a major target for drug discovery because it is a conserved feature of bacteria and not present in humans.

Using cantilever based biosensors our group has shown that the binding interaction of the antibiotic vancomycin with the glycopeptide D*Ala* can be quantified [12].

Experiments are repeated here to find out whether the new reflective diffraction readout can be applied to a clinically relevant problem.

Vancomycin is the most potent antibiotic on the market against Gram-positive bacteria [112]. It works by inhibiting the formation of the bacterial cell wall [111, 112, 127], leading the cell to undergo lysis.

It has been proposed and observed that the bending of the cantilever induced by the interaction of vancomycin with D*Ala* on the cantilever surface can be explained by a chemical and a geometrical factor [12]. The chemical factor describes the local interaction of vancomycin with the cell wall target immobilised on the cantilever and the geometrical factor describes the interaction between the occupied binding sites. If all occupied binding sites are isolated from each other, no bending occurs. As soon as the connectivity of the occupied binding sites increases, a network of interactions is formed (percolation) [128] and the cantilever bends.

It is speculated that nanomechanical percolation may play an important role not only in sensor response but also in the glycopeptide antibiotic mode of action in real bacteria [12].

In the experiments shown here vancomycin passes through the flow cell and binds to the glycopeptides which are immobilised on the cantilever surface. Static mode measurements of the cantilever bending allows to study the in-plane forces that are generated when vancomycin binds to D*Ala* and this in turn helps to understand the nanomechanical influence of the antibiotic on the bacterial cell wall. Vancomycin shows a strong cooperative binding to D*Ala* via five hydrogen bonds as depicted in Fig. 5.1. *PEG* is known to passivate the surface (see Sec. 3.4) and therefore it was used as the coating for the reference cantilever.

Two different illumination conditions have been introduced in Sec. 2.4.3 on page 63. In the first case entire cantilever is illuminated and in the second case the entire cantilever plus a part of the chip base is illuminated. Before showing the results for both cases it will be shown how the cantilever bending is calculated.

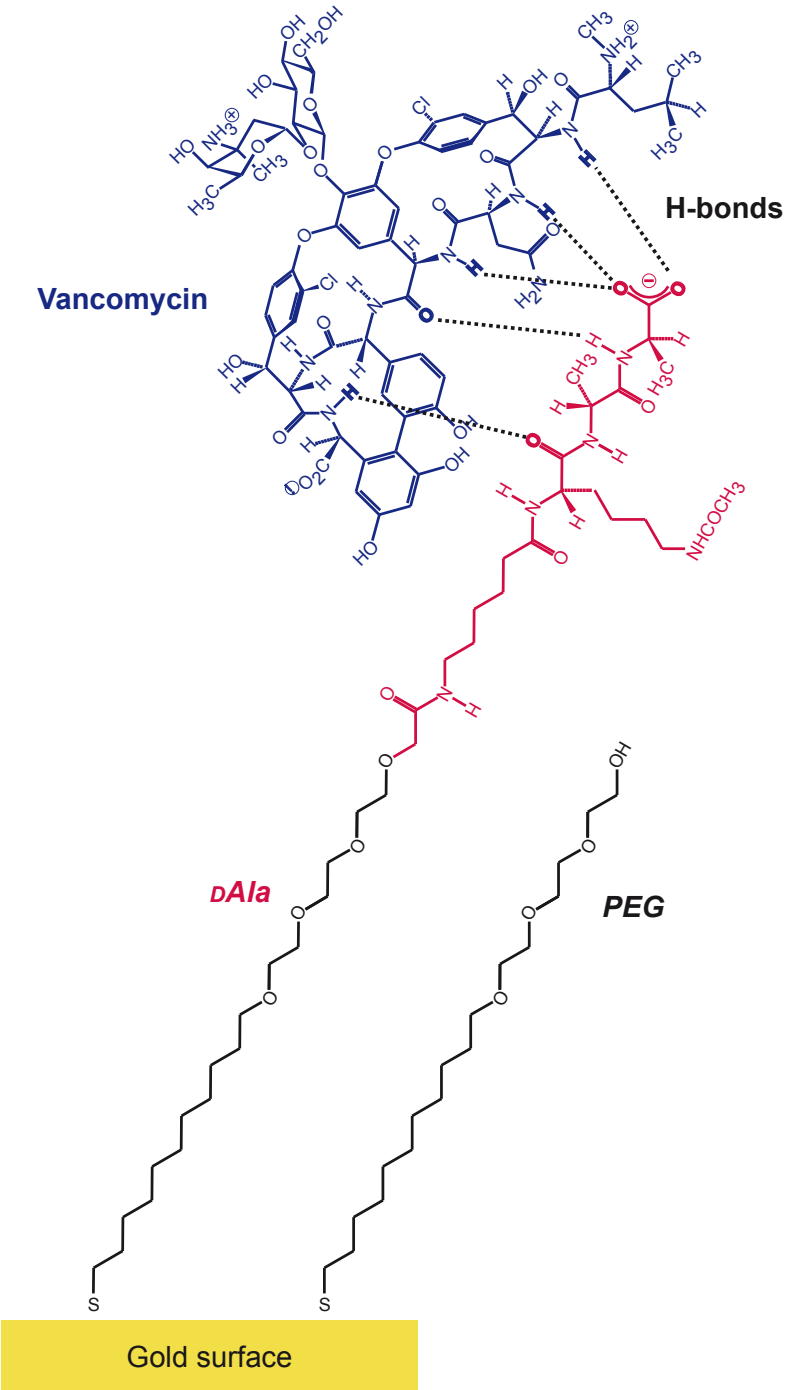


Figure 5.1: *PEG* and D*Ala* immobilised on a gold surface and interaction of vancomycin with D*Ala* (adapted from [12])

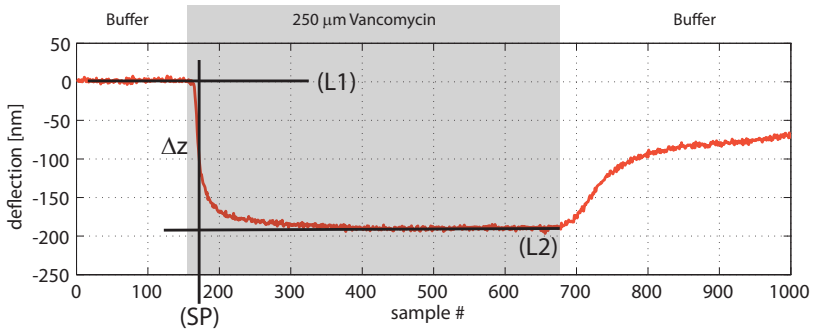


Figure 5.2: A typical deflection signal from a vancomycin experiment. The initial buffer injection is followed by 250 $\mu$M of vancomycin. Binding of the vancomycin molecules to the D*Ala* coating on the cantilever takes place and bending is induced as a consequence. After saturation buffer is injected again and, in this case, washes off a fraction of the bound vancomycin.

### Determining the Deflection $\Delta z$

A typical deflection signal for a reaction of 250 $\mu$M vancomycin with D*Ala* immobilised on a cantilever is shown in Fig. 5.2. After buffer has been injected into the flow cell, 250 $\mu$M vancomycin is flowed in, which leads to a deflection of the cantilever. Once the signal is saturated, buffer is flowed into the cell again.

Moyu Watari, a former member of our group, developed software to speed up analysis of deflection data and allow for better comparison between different measurements [45]. The method is depicted in Fig. 5.2. A straight line (L1) is fitted to a region of the initial buffer injection before the vancomycin is injected. Another straight line (L2) is fitted to the saturated part of the signal and finally the switching point (SP) is defined. The deflection $\Delta z$ is now determined by calculating the vertical distance between the fitted straight lines L1 and L2 at SP. This is the absolute deflection. In the case that more than one cantilever is read out, the mean of the deflections is calculated and the standard deviation is used as the error.

Environmental influences like temperature changes will distort the deflection measurements or cause drift in the deflection signal. Therefore using a reference cantilever provides a baseline for the results. To take into account the environmental effects, the deflection of the reference cantilever is determined. Subtracting the deflection of the reference cantilever from the measuring cantilever yields the differential de-

flection signal. Thus, if the environmental changes influences the measurement and reference cantilever to the same extent, its influence is cancelled in the differential signal.

However previous work in our group has shown that small temperature changes can influence the bending of the cantilevers, for example differences in chain length or end group of a simple SAM [45, 46]. In principle the best reference coating should be a chiral enantiomer – that is a molecule which has the same physical groups, density, solubility etc but these groups are spatially arranged in left and right handed forms which leads to highly specific interactions with chiral receptors. Unfortunately L*Ala* chiral reference coatings were unavailable for these experiments but previous work by Ndieyira et al. in our group had found no substantive difference in the thermal expansion of D*Ala* and *PEG* reference coatings [12, 70].

The deflection signal as shown in Fig. 5.2 originates from a measurement with the optical lever deflection. If the diffraction technique is used, the deflection signal has to be obtained from analysing the changes in the diffraction pattern.

## 5.1 Illumination of the Cantilever without the Chip Base

The measurement was performed by illuminating the cantilever only and not the chip base. This test experiment presented here was made with a chip whose initial cantilever bending was high ($\approx 20\,\mu$m). Therefore a lens had to be used in order to capture the diffraction pattern.

The diffraction pattern for *PEG* and D*Ala* are shown in Fig. 5.3. In (a) and (c) almost no change is visible for the *PEG* coated cantilever when 250 $\mu$M vancomycin is injected into the cell, whereas in (b) and (d) a change in the diffraction pattern is observed for the D*Ala* coated cantilever.

The conversion constant to translate the shift into a bending in nanometres could not be determined with the simulation since the exact illumination condition of the cantilever was not recorded and a lens was used in the reflected laser beam. Instead the data from the diffraction measurements were scaled to fit the optical

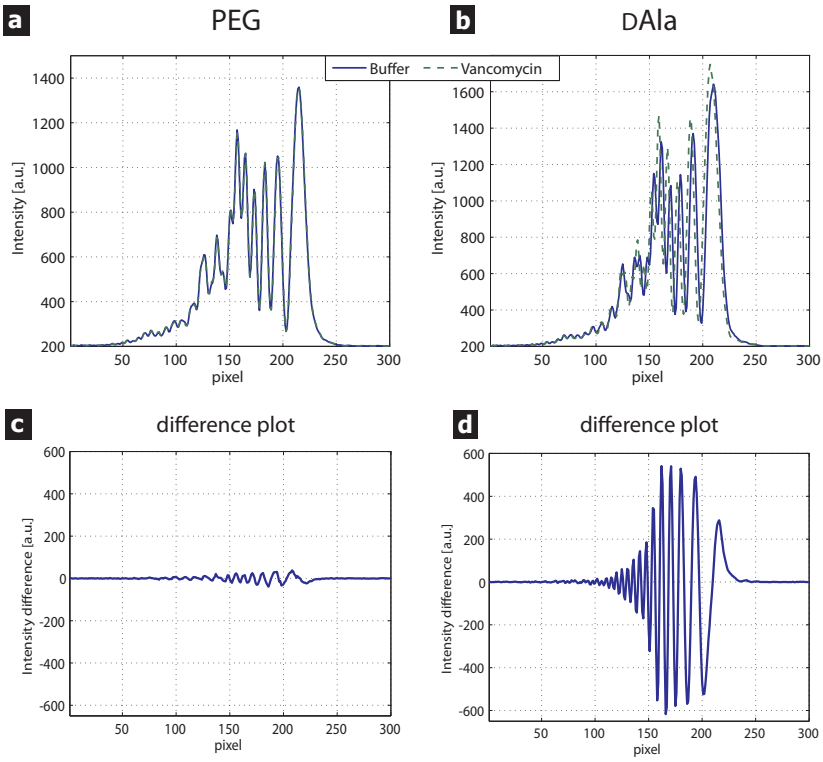


Figure 5.3: Reflective diffraction pattern for (a) *PEG* and (b) D*Ala* coated cantilever while buffer is running (blue solid line) and after the injection of 250 $\mu$M vancomycin (green dashed line). (c) and (d) show the difference of the diffraction plots from (a) and (b), respectively.

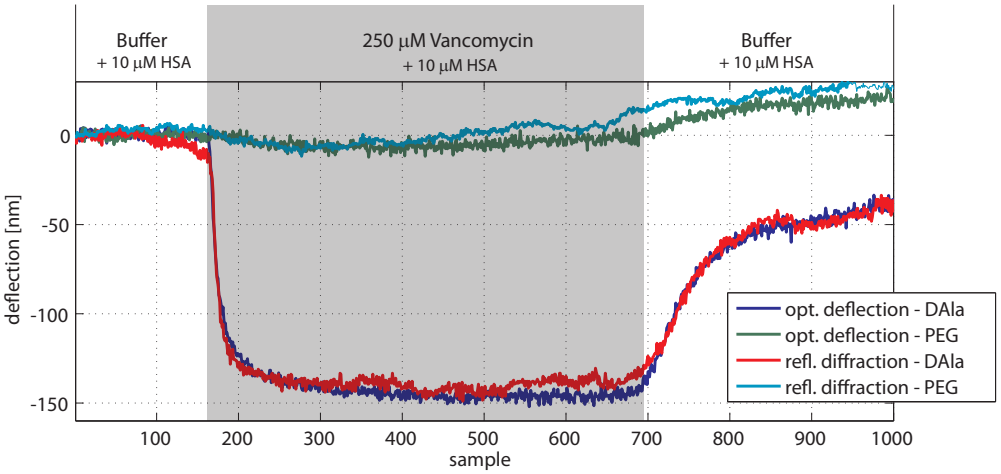


Figure 5.4: Shown are the absolute signals measured on one D*Ala* and one *PEG* coated cantilever upon injection of 250 $\mu$M of vancomycin. 10 $\mu$M of human serum albumin (HSA) was added to buffer and vancomycin solution to reduce drift. Measured simultaneously with the optical lever technique and the reflective diffraction technique.

lever deflection measurement. The scaling factor $s$ was determined by minimising the sum of the squared differences $f(s)$ of the two D*Ala* measurements:

$$\frac{\partial f}{\partial s} = 0$$

$$\text{with} \qquad f(s) = \sum_{i=1}^{\text{sample}_{\max}} \left( \Delta z_{\text{ol},i} - s \cdot \Delta z^*_{\text{dr},i} \right)^2$$

$\Delta z_{\text{ol},i}$ and $\Delta z^*_{\text{dr},i}$ is the deflection at sample $i$ measured with the optical lever technique and the diffractive reflection technique, respectively. $\text{sample}_{\max}$ is the number of samples measured and $s$ the scaling factor. The shift of the peak on the right side of the diffraction pattern (see Fig. 5.3(a)&(b)) was used as a measure for the bending. A shift of one pixel corresponds to a bending of $\Delta z = 57.6\,\text{nm}$. The Matlab routine shown in Appendix B.3 on page 159 was used to perform the calculation. Using another numerical calculation (see Sec. 2.5 on page 65) it could be confirmed that the magnitude of the scaling factor is in a reasonable range. The measurement results are plotted in Fig. 5.4 showing good agreement of both techniques.

### $K_d$ Measurement

The objective of these measurements is to measure the binding constants for a model drug-target system with the classic optical readout and diffractive readout and compare the results to surface plasmon resonance results.

$K_d$ is the equilibrium dissociation constant which is defined as the ratio of the off-rate $k_d$ and the on-rates $k_{on}$ of a reaction [129]:

$$K_d = \frac{k_{off}}{k_{on}}$$

It is used here as a measure for the binding affinity of vancomycin to the D*Ala* peptide on the cantilever surface. In order to determine the $K_d$, the differential deflection ($\Delta z\,(\text{D}Ala) - \Delta z\,(PEG)$) for the following vancomycin concentrations was determined: 0.05, 1, 3, 5, 10, 50, 100, 250, 500 $\mu$M. Evaluated were three D*Ala* and two *PEG* coated cantilevers on one chip. The differential deflections measured are listed in Table 5.1.

| concentration [$\mu$M] | optical deflection method deflection [nm] | reflective diffraction method deflection [nm] |
|---|---|---|
| 0.05 | 27±5 | 37±8 |
| 1 | 76±16 | 52±9 |
| 3 | 87±10 | 91±13 |
| 5 | 90±14 | 88±7 |
| 10 | 104±18 | 71±12 |
| 50 | 125±17 | 108±11 |
| 100 | 133±21 | 126±14 |
| 250 | 148±20 | 148±25 |
| 500 | 132±13 | 91±9 |

Table 5.1: Comparison of cantilever deflection measured for different vancomycin concentrations with the optical deflection method and the reflective diffraction method. The deflection stated is the mean of the differential deflection and the error is the standard deviation.

The $K_d$ can be determined by fitting the Langmuir adsorption isotherm to the deflection data for different concentrations (adapted from [12]):

$$\Delta z\left([\mathrm{Van}]\right) = \frac{a \cdot [\mathrm{Van}]}{K_d + [\mathrm{Van}]}$$

with $a$ being the maximum deflection, [Van] the vancomycin concentration and $\Delta z\left([\mathrm{Van}]\right)$ the deflection of the cantilever for [Van] at saturation. The data and fitted curves are shown in Fig. 5.5 which yield $a = 131 \pm 7\,\mathrm{nm}$ and $K_d = 1.2 \pm 0.4\,\mu\mathrm{M}$ for the optical lever readout and $a = 113 \pm 12\,\mathrm{nm}$ and $K_d = 1.2 \pm 0.8\,\mu\mathrm{M}$ for the reflective diffraction readout. Although the $a$ values are about half of the expected value, they agree fairly well with each other. Both $K_d$ values agree quite well with each other and with previously published values measured on cantilevers ($K_d = 1.0 \pm 0.3\,\mu\mathrm{M}$; ref. [12]) and with surface plasmon resonance measurements ($K_d = 1.1 \pm 0.1\,\mu\mathrm{M}$; ref. [130]).

Interestingly Fig. 5.5 shows a slight fall for the concentration of 500 $\mu$M. This is most probably because of inefficient HCl regeneration of the active D*Ala* coated cantilever at high vancomycin concentrations. However intriguingly this was not observed in the classic reflection data. Future work should try to investigate this effect further.

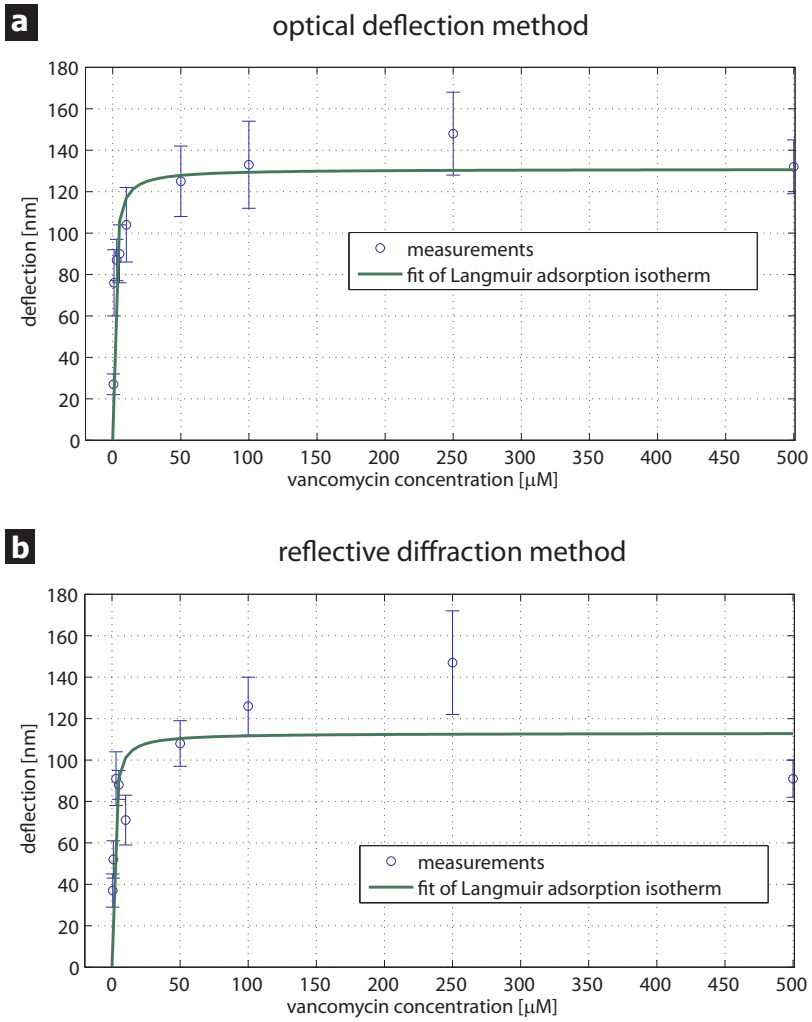


Figure 5.5: Fit of Langmuir adsorption isotherm to deflection data. (a) The fit for the optical deflection method yielded $a = 131 \pm 7\,\text{nm}$ and $K_d = 1.2 \pm 0.4\,\mu\text{M}$. (b) The fit for the reflective diffraction method yielded $a = 113 \pm 12\,\text{nm}$ and $K_d = 1.2 \pm 0.8\,\mu\text{M}$.

## 5.2 Illumination of the Cantilever and Chip Base

If the cantilever and additionally a part of the chip base is illuminated, the expansion or contraction of the diffraction pattern that is measured in reflection can be analysed to obtain the deflection signal as described in chapter 2. This kind of illumination has the advantage that a reference signal can be seen in the diffraction pattern itself, which makes the entire readout more robust.

A preliminary experimental result for bending induced by vancomycin is shown in Fig. 5.6. When the cantilever bends, the whole diffraction pattern expands but the reference peak does not move. From the width of the diffraction pattern under buffer flow (blue solid line) one can estimate the initial cantilever bending using the simulation to be $\approx -4\,\mu$m. Once 1 $\mu$M vancomycin is flowed over the cantilever and the signal has saturated the diffraction pattern is expanded (green dotted line).

The simulation is used to determine the conversion factor that translates the expansion of the diffraction pattern into deflection of the free end of the cantilever in units of nanometres. Thus, an expansion of 1 pixel of the diffraction pattern corresponds to 8.9 nm deflection of the free end of the cantilever.

The result of the analysis is shown in Fig. 5.7 and shows good agreement for the differential deflection (c).

### Summary of Vancomycin Measurements

Presented in this chapter are different "proof of concept" experiments performed with cantilevers coated with *PEG* and D*Ala*. The first part shows results for experiments with the entire cantilever being illuminated by a laser. The initial bending of the cantilevers was very high. Nonetheless, the deflection of the cantilever could still be recorded by using a lens to capture the diffraction pattern. The proportionality constant in this case had to be obtained using the optical lever technique. The second part shows the results from the experiments where not only the entire cantilever is illuminated but additionally a part of the chip base. Using the conversion constant obtained with the simulation to convert the expansion of the diffraction pattern

into bending in units of nanometre reveals good agreement between the reflective diffraction technique and the optical lever technique.

The measurements with vancomycin show that the reflective diffraction method can be used to determine the bending of the cantilever for clinically relevant measurements, such as quantifying drug-target interactions to tackle drug-resistant infectious diseases.

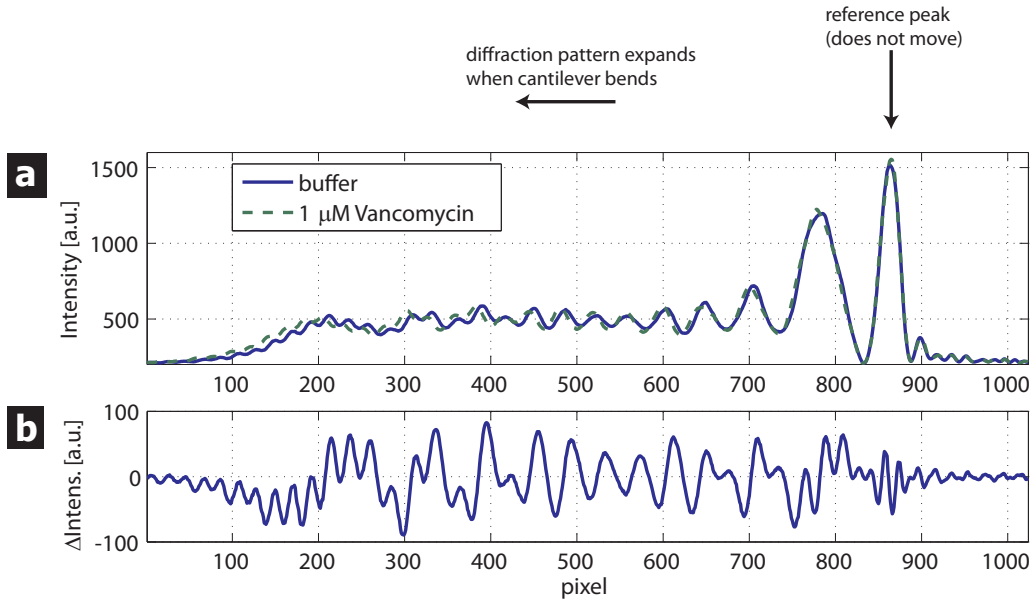


Figure 5.6: (a) Reflective diffraction pattern for two different deflections of the cantilever. The width of the diffraction pattern corresponds to the bending of the cantilever. It increases with growing deflection. The solid line shows the diffraction pattern when buffer is flowing. The dashed line shows the pattern when 1 $\mu$M vancomycin is flowing through the measuring cell and has bound to the cantilever. The binding of vancomycin increases the bending. (b) shows the difference between of the diffraction pattern shown in (a) to enhance the visibility of the changes.

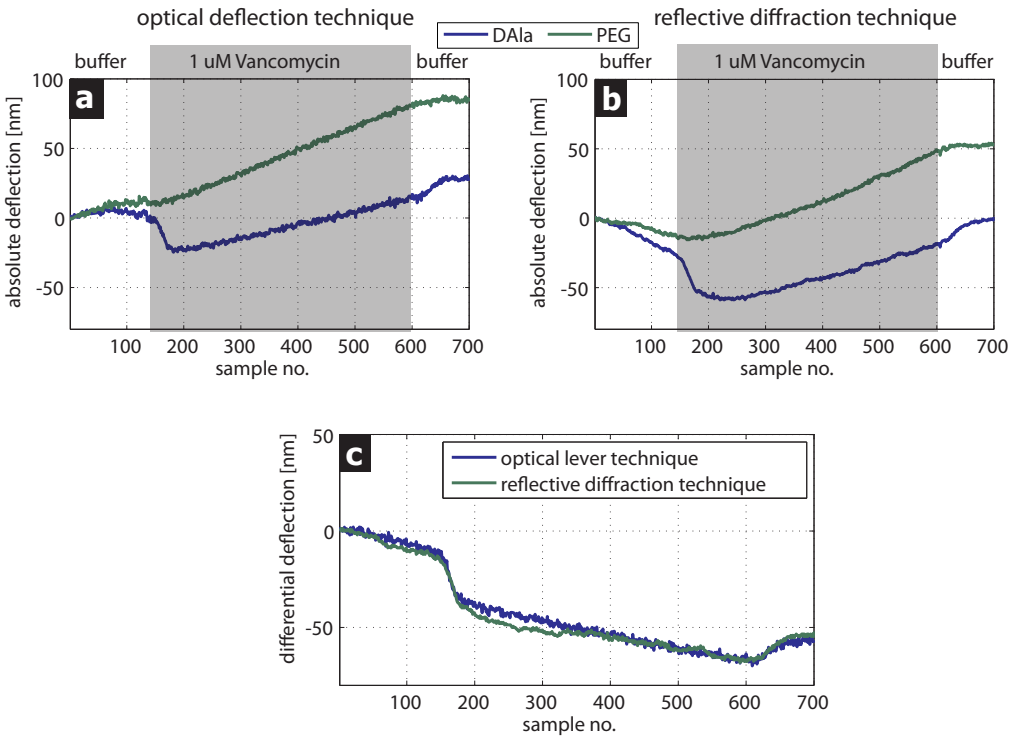


Figure 5.7: Comparison of deflection measurements with the optical deflection technique (a) and the reflective diffraction technique (b) showing the absolute bending signal in. The differential signal (DAla-PEG) is shown in (c) and shows good agreement of both measurements.

# 6

# Conclusion & Outlook

This thesis presents a diffractive readout method for cantilever-based biosensors. It can be operated in transmission and reflection mode, in air and in liquid. It was discovered using the simulation presented in chapter 2 and then tested by performing experiments with the newly designed and built experimental setup introduced in chapter 3.

In all experiments the deflection of the cantilever was measured simultaneously with the conventional optical lever technique as a control and a means of having a direct comparison with a long established readout system. Comparing the changes of the diffraction pattern acquired in transmission and reflection mode, showed that for the latter, not only the resolution is higher, but also the readout of the bending is unaffected by a potential tilting of the cantilever chip if the illuminated region contains the entire chip and a part of the chip base. Therefore, the reflection mode of the diffractive technique should be considered as the readout of choice and should be the focus of further development efforts.

The resolution of the reflective diffraction technique is comparable with the optical lever technique. The alignment for the latter is time consuming and also a source of error for quantitative measurements since the exact position where the focused laser spot hits the cantilever has to be known in order to obtain a correct conversion from the angular rotation measured to the actual deflection in units of nanometre at the free end of the cantilever [131, 132]. Since the spot of the laser

| | resolution (1 nm) | distinguish tilt./bend. | alignment | miniaturi-sation | paralleli-sation |
|---|---|---|---|---|---|
| diffractive optical readout in reflection mode | + | + | + | TBC | + |

Table 6.1: Benchmark for the new diffractive optical readout. + / - denotes whether the requirement is fully met/not met. Miniaturisation has not been experimental shown yet and needs to be confirmed (TBC) with future experiments.

beam for the diffractive technique is larger than the cantilever, alignment becomes very easy. It is not necessary to know the exact position of the cantilever in the laser beam. It has only to be ensured that the entire cantilever and a part of the chip base reflect the laser. This means, that the alignment procedure is almost superfluous and therefore saves 30-120 mins per measurement which have to be spend for the optical lever technique. Coming back to the six properties mentioned in the beginning the performance of the optical diffractive readout is shown in table 6.1. It is assumed that miniaturisation is not an obstacle to the diffractive readout since it relies on diffraction which becomes more pronounced for smaller objects. Results of the simulation also support the assumptions (see Fig. 6.1c&d). Since alignment with this readout is straightforward, parallelisation for even more than eight cantilevers should not be too difficult to be obtained either. Assuming that miniaturisation and parallelisation is possible without problems, the diffractive readout developed and presented in this thesis is another step towards the translation of cantilever based biosensors technique from laboratories into industry and hospitals.

The future work mentioned in the next chapter should concentrate on optimising the reflection mode which offers several advantages when compared with the transmission mode, as mentioned above.

## 6.1 Future Work

After reviewing the experiments and results presented in this thesis it becomes obvious that optimisation is the next necessary task. Optimisation has to be performed

in several areas, ranging from the experimental setup and the flow cell to the optical readout and the analysis of the diffraction pattern.

### 6.1.1 The Experimental Setup

The experimental setup is very versatile and useful for testing all different kinds of optical configurations. (More optical configurations can be found in the patent filed [15] which is also reprinted in Appendix A.)

One drawback with the current setup is that the flow cell is mounted ≈25 cm above the optical table requiring all optical equipment to be mounted on high posts which amplify vibrations. For further optimisation a dedicated experimental prototype has to be built.

The next step should be to miniaturise the experimental setup and incorporate all components, the chip, laser and CCD, into one frame for higher stability.

### 6.1.2 The Flow Cell

The flow cell used was designed with a front and a back window allowing for transmission measurements (see items 4 and 7 in drawing on page 170). Since the findings point towards the reflection method, a back window is not needed anymore.

Also, the volume of the current flow cell is fairly large ($\approx 200\,\mu$l). This means that a lot of reagent is needed. In order to reduce cost and save reagents the volume of the fluid cell can be reduced to about $10\,\mu$l by having only the cantilevers and a part of the chip base protruding into the measuring chamber.

### 6.1.3 Laser and Optical Readout

The current setup uses an xyz-stage to move the cantilevers into the light beam for the measurements. This can introduce disturbances in the liquid which can be avoided by changing the illumination of the cantilever in a way that no movement of the flow cell is needed anymore.

An idea which has to be tested is, to expand the illuminating laser beam so that it covers all cantilevers and the parts of the chip base too. This of course will result in a complex interference of all cantilevers which, in the absence of suitable software, might make it difficult to extract the bending of individual cantilevers. The significant advantage of course is, that the difference between the reference and measuring cantilevers can be determined from a single CCD image. Until a method is found to do this, a cylindrical lens could be used which only influences the light in the dimension perpendicular to the long axis of the cantilever. This would separate the individual diffraction pattern. The advantage over the previous method where the cantilever chip is moved is that the bending of all eight cantilevers can now be read out simultaneously instead of sequentially.

### 6.1.4 The Cantilever Chip

To facilitate consistent use of the proposed readout method it is advantageous to use a mask while evaporating the gold onto the cantilever chip to define the reflective area on the chip body precisely. This would enable a better comparison between results from different chips. Another improvement would be to etch a well defined diffraction grating into the chip body. When the cantilever and the chip body are illuminated, the diffraction grating will create an optical ruler which can be used, firstly, to determine the distance between chip and the recording CCD and, secondly, to measure the width of the diffraction peak more accurately. The intensity of the diffraction from the grating has to be tuned in a way that it does not shadow the diffraction generated by the bending cantilever.

## 6.2 Holographic Approach to the Diffraction Pattern

It is already mentioned in Sec. 2.6 on page 68 that the reflective diffraction measurement could be regarded as a holographic technique. The reflection from the chip base corresponds to the reference beam with the field $E_R$ and the reflection from the cantilever corresponds to the object beam with the field $E_O$. Both beams

will interfere at the position of the CCD, resulting in an interference pattern. The CCD does not record the phase of the wave but the time-average intensity of the superposition of both beams. The intensity distribution at the CCD can be split into three components [94]. The first two are the intensities for reference and object beam separately which are proportional to $E_R^2$ and $E_O^2$, respectively and the third represents the interference between both beams and is proportional to $E_R \cdot E_O$. In the following it is referred to as the mixed term.

Fig. 6.1(a) and (b) show simulation results for the intensity of individual parts of the reflected beam. The length of the cantilever and the illuminated array is 500 $\mu$m each and the bending simulated is $\Delta z = -1\,\mu$m in terms of deflection of the free end of the cantilever. The individual parts of the reflected beam shown in (a) can be recognised in the intensity pattern for the entire reflected beam in (c). This suggests that the mixed term plays a minor role when compared to $E_O^2$ and $E_R^2$. Comparing the dimensions of the illuminated area of 1 mm to the distance of the CCD of 100 mm which was used in experiments and the simulation here it can be concluded that the measurements were performed in the optical near-field. For these dimensions the far-field starts at $\approx$1.6 m.

Changing the dimension of the cantilever or the chip base in the simulation will have an effect on the influence of each one of the three components. Fig. 6.1(c) and (d) show the simulation for a cantilever and illuminated flat region of the chip, both of length 50 $\mu$m. In this case the CCD is very close to the Fraunhofer region and the overall intensity pattern of cantilever is governed by the mixed term.

Both simulations were made for a symmetrical illumination of cantilever and chip base. Miniaturising the dimensions of the cantilever, changes the influence from the terms for the individual beams and the mixed term. By using asymmetrical illumination conditions the relative contributions of the reference beam $E_R$ and the object beam $E_O$ could be shifted too.

These simulations show how the different terms influence the overall resulting intensity pattern and how individual terms can be pronounced. New ways can be

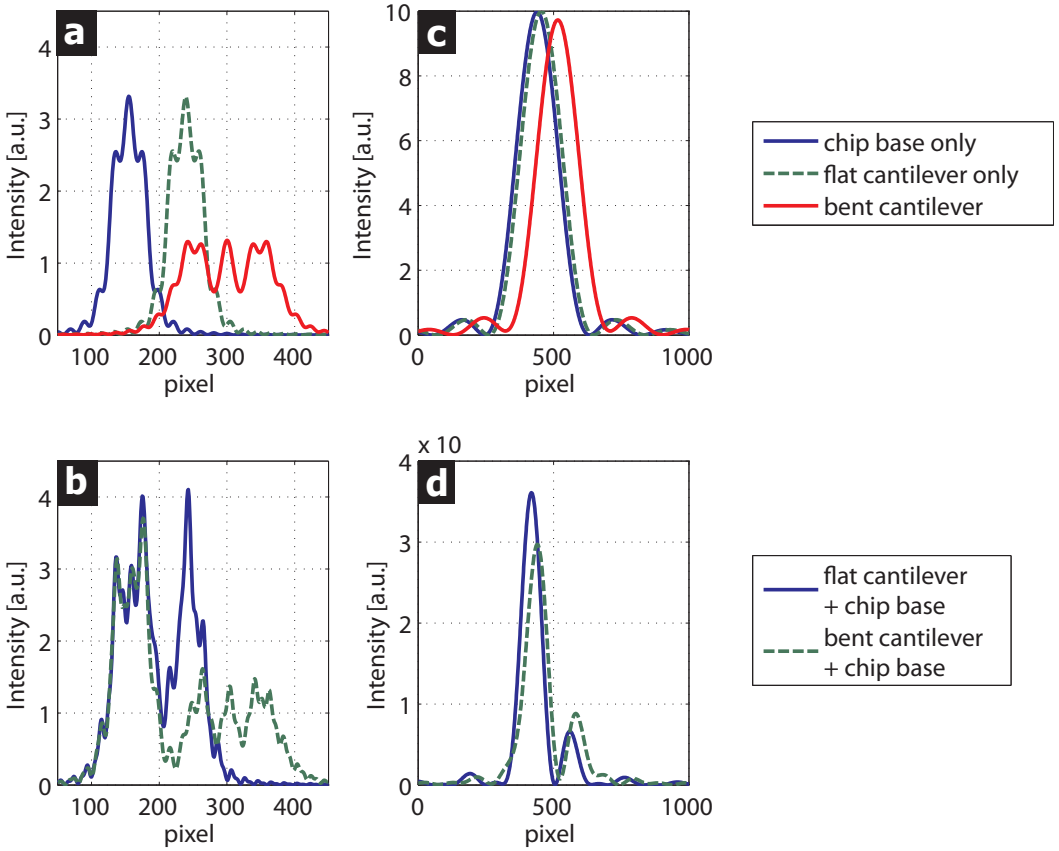


Figure 6.1: Simulation of different parts of the reflected beam for two different cases. The cantilever and the illuminated part of the chip base for the simulated patterns in (a) and (b) have a length of 500 $\mu$m each. The cantilever deflection is -1 $\mu$m. (a) shows the intensity pattern of the reflected intensities for individual parts of the cantilever and (b) shows the overall intensity pattern for the beam reflected from chip base and cantilever. The cantilever and the illuminated part of the chip base for the simulated patterns in (c) and (d) have a length of 50 $\mu$m each. The cantilever deflection is -100 nm. (c) shows the intensity pattern of the reflected intensities for individual parts of the cantilever and (d) shows the overall intensity pattern for the beam reflected from chip base and cantilever.
The cantilever is 500 $\mu$m long chip look for chip with a 50 $\mu$m long cantilever that contribute to the overall intensity pattern.

developed to read out the deflection of cantilevers which are too small to be measured by the conventional optical beam deflection technique. Choosing the right dimensions to maximise the influence of the mixed term $E_R \cdot E_O$ could make it easier to solve the inverse scattering problem to directly calculate not only the bending but the whole bending profile.

## 6.3 Vision

The diffractive readout can be used to determine the bending of small cantilevers which cannot be read out with the conventional optical lever technique anymore, which relies on the precise illumination of a small spot exactly at the free end of the cantilever. This opens up new possibilities in shrinking down the measuring device and using cantilever based biosensors in handheld point-of-care devices (see Fig. 6.2).

Also, the reflective diffraction technique and the included improvements presented here would enable a radical departure from the approach with cantilevers being attached to a chip base. Having an independent measure of the tilt in the diffraction pattern, one should be able to measure the strains of free floating cantilevers, detached from the chip base. The idea is to fabricate a rectangular board (shown in Fig. 6.3) which is free to flow in a liquid channel or tubing. The middle part is thicker than the two ends which act as cantilevers. A diffraction grating engraved in the middle part could act as an optical ruler as mentioned in the last chapter and be used as a diffracting bar code [133] to identify individual chips.

If proven reliable, the new diffractive readout combined with these cantilevers which could be further miniaturised and flow through microfluidic channels, has the potential to generate a new class of biosensors based on the cantilever principle. Scaling up the numbers would be accomplished by adding more cantilevers into the channels. One readout could determine the bending of all the cantilevers flowing past it, like a till at the supermarket checkout.


Figure 6.2: A point of care device based on rigidly mounted microcantilever array biosensor and a two-dimensional readout.

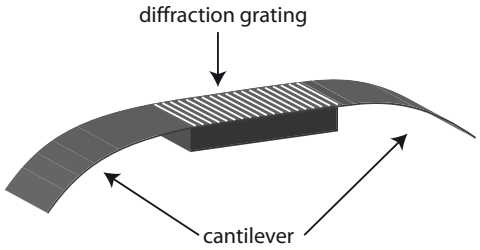


Figure 6.3: Second generation of cantilever based biosensors. Such chips can be freely suspended in solutions passing via microfluidic channels through optical readers.

# Appendix

# A

# Patent

(12) INTERNATIONAL APPLICATION PUBLISHED UNDER THE PATENT COOPERATION TREATY (PCT)

(19) World Intellectual Property Organization
International Bureau

(43) International Publication Date
30 October 2008 (30.10.2008)

PCT

(10) International Publication Number
WO 2008/129272 A1

(51) International Patent Classification:
*G12B 21/20* (2006.01)

(21) International Application Number:
PCT/GB2008/001375

(22) International Filing Date: 17 April 2008 (17.04.2008)

(25) Filing Language: English

(26) Publication Language: English

(30) Priority Data:
0707470.1 18 April 2007 (18.04.2007) GB

(71) Applicant *(for all designated States except US)*: **UNIVERSITY COLLEGE LONDON** [GB/GB]; Gower Street, London WC1E 6BT (GB).

(72) Inventors; and
(75) Inventors/Applicants *(for US only)*: **AEPPLI, Gabriel** [CH/GB]; University College London, Gower Street, London WC1E 6BT (GB). **DUECK, Benjamin** [DE/GB]; University College London, Gower Street, London WC1E 6BT (GB).

(74) Agent: **TYSON, Robin, Edward**; J.A. Kemp & Co., 14 South Square, Gray's Inn, London WC1R 5JJ (GB).

(81) Designated States *(unless otherwise indicated, for every kind of national protection available)*: AE, AG, AL, AM, AO, AT, AU, AZ, BA, BB, BG, BH, BR, BW, BY, BZ, CA, CH, CN, CO, CR, CU, CZ, DE, DK, DM, DO, DZ, EC, EE, EG, ES, FI, GB, GD, GE, GH, GM, GT, HN, HR, HU, ID, IL, IN, IS, JP, KE, KG, KM, KN, KP, KR, KZ, LA, LC, LK, LR, LS, LT, LU, LY, MA, MD, ME, MG, MK, MN, MW, MX, MY, MZ, NA, NG, NI, NO, NZ, OM, PG, PH, PL, PT, RO, RS, RU, SC, SD, SE, SG, SK, SL, SM, SV, SY, TJ, TM, TN, TR, TT, TZ, UA, UG, US, UZ, VC, VN, ZA, ZM, ZW.

(84) Designated States *(unless otherwise indicated, for every kind of regional protection available)*: ARIPO (BW, GH, GM, KE, LS, MW, MZ, NA, SD, SL, SZ, TZ, UG, ZM, ZW), Eurasian (AM, AZ, BY, KG, KZ, MD, RU, TJ, TM), European (AT, BE, BG, CH, CY, CZ, DE, DK, EE, ES, FI, FR, GB, GR, HR, HU, IE, IS, IT, LT, LU, LV, MC, MT, NL, NO, PL, PT, RO, SE, SI, SK, TR), OAPI (BF, BJ, CF, CG, CI, CM, GA, GN, GQ, GW, ML, MR, NE, SN, TD, TG).

**Published:**
— *with international search report*

(54) **Title:** APPARATUS AND METHOD FOR MEASURING DEFORMATION OF A CANTILEVER USING INTERFEROMETRY

FIG. 2A

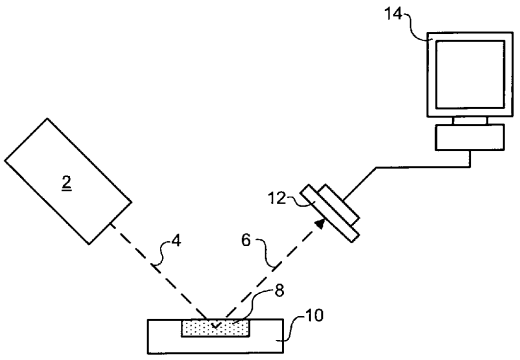


(57) **Abstract:** Apparatus and method for measuring the deformation of a tethered or untethered cantilever by projecting a radiation beam onto the cantilever, detecting an interference pattern reflected from or transmitted through the cantilever, and calculating the deformation of the cantilever by measuring the intensity variation within at least a portion of the interference pattern.

WO 2008/129272 A1

WO 2008/129272 PCT/GB2008/001375

# APPARATUS AND METHOD FOR MEASURING DEFORMATION OF A CANTILEVER USING INTERFEROMETRY

The present invention relates to the problem of measuring the deformation of cantilevers, and in particular micro-cantilevers.

The accurate measurement of cantilever deformation is a key issue in a number of different applications. For example, the atomic force microscope has for some time used deflection of a cantilever at the tip to measure the force between tip and sample.

More recently, arrays of cantilevers have been used as biosensors. It has been shown that when biochemically specific interactions occur between a ligand immobilized on one side of a cantilever and a receptor in solution, the cantilever bends due to a change in surface stress, which can be detected optically.

More generally, sensor arrays are very promising for application in disease diagnosis, drug screening, sensitive detection of very small concentrations of different substances, NOSE applications, fluid/gas flow, pressure sensors, and for temperature measurements. A nanomechanical actuation mechanism may be used, according to which cantilevers are microfabricated by standard low-cost silicon technology and, by virtue of the size achievable, are extremely sensitive to the presence of small molecule chemical and biological interactions, e.g. detecting femtomoles of biomolecules of DNA, and many other chemicals, including explosives.

The ability to detect multiple biomolecules has been limited to the number of fixed-end cantilevers that can be microfabricated. In addition, everyday clinical use has been challenging because the physical measurement apparatus could not be separated from the biochemical environment. Also, as in all fixed array-based combinatorial methods where scale-up is derived from increasing the number and density of elements in the array, chemical cross-contamination and physical cross-talk represent significant hurdles. These issues are discussed in E. D. Isaacs, M. Marcus, G. Aeppli, X. D. Xiang, X. D. Sun, P. Schultz, H. K. Kao, G. S. Cargill, and R. Haushalter, "Synchrotron x-ray microbeam diagnostics of combinatorial synthesis", Applied Physics Letters 73(13), 1820 (1998).

Figure 1 illustrates a typical prior art optical detection method, which relies on

shining a fixed laser onto the free end of a tethered cantilever. However, such methods provide no information about the profile of bending and have limited scalability for microarray technology.

A number of different methods have been published describing how to measure the profile of cantilevers.

Tada et al. (H. Tada, A. E. Kumpel, R. E. Lathrop, J. B. Slanina, P. Nieva, P. Zavracky, I. N. Miaoulis, and P. Y. Wong, "Novel imaging system for measuring microscale curvatures at high temperatures", Review of Scientific Instruments 71(1), 161 (2000)) disclose a method in which the deflection of a 100 μm cantilever is detected with a resolution of 1.5 μm. Since deflections for cantilever biosensors are expected to be below 200 nm (based on a 500 micron long, 100 micron wide, 1 micron thick silicon cantilever with a spring constant of 0.02 N/m, which corresponds to a surface stress change of approximately 30mN/m), the technique of Tada et al is not suitable for such applications.

S. Jeon and T. Thundat, "Instant curvature measurement for microcantilever sensors", Applied Physics Letters 85(6), 1083 (2004) discloses an approach using a multiple-point deflection technique, where eight light-emitting diodes are focused on various positions of a cantilever. The main drawbacks for this method are the difficulty of aligning the eight lasers as well as evaluating large number of cantilevers.

J. Mertens, M. Alvarez, and J. Tamayo, "Real-time profile of microcantilevers for sensing applications", Applied Physics Letters 87(23) (2005) discloses a technique in which the bending profile is acquired by optically rastering the cantilever. Drawbacks for this method are, first, the error introduced mechanically through the raster process and second, even more significant, the movement of the cantilever itself during the measurement.

Two methods have been published using optical interference.

Firstly, in the method disclosed in G. G. Yaralioglu, A. Atalar, S. R. Manalis, and C. F. Quate, "Analysis and design of an interdigital cantilever as a displacement sensor", Journal of Applied Physics 83(12), 7405 (1998), interdigitated cantilevers are used, which allow for detecting the deflection of the free end of the cantilever only.

Secondly, in the method disclosed in M. Helm, J. J. Servant, F. Saurenbach, and R. Berger, "Read-out of micromechanical cantilever sensors by phase shifting

interferometry", Applied Physics Letters 87(6) (2005), the bending profile of the whole cantilever can be determined. However, the disclosed method relies on: a) the use of a point of reference on the cantilever support; and b) the interference of two beams, a reference beam and the reflected beam from the cantilever. The arrangement is complex and only applicable to tethered cantilevers.

It is an aim of the present invention to overcome some of the above-mentioned problems with the prior art.

According to an aspect of the present invention, there is provided an apparatus for measuring deformation of a cantilever, comprising: a projection system for projecting a radiation beam onto a cantilever; and a measurement system for detecting radiation transmitted through or reflected from said cantilever, wherein said projection system is arranged such that the radiation transmitted through or reflected from said cantilever forms an interference pattern; said measurement system is configured to measure the spatial variation in intensity within at least a portion of said interference pattern; and said apparatus further comprises a deformation calculating system for calculating a deformation of said cantilever from the spatial variation in intensity measured by said measurement system.

According to an alternative aspect of the invention, there is provided a method of measuring deformation of a cantilever, comprising: projecting a radiation beam onto a cantilever; and detecting radiation transmitted through or reflected from said cantilever, wherein: said the radiation beam is projected onto said cantilever in such a way as to form an interference pattern; and said method further comprises: measuring the spatial variation in intensity within at least a portion of said interference pattern; and calculating a deformation of said cantilever from the measured spatial variation in intensity.

In other words, information concerning the nature and/or extent of the cantilever deformation (for example, bending and/or other changes in shape – rather than orientation – of the cantilever) is extracted from a change in the structure or content of an interference pattern (i.e. a change in the spatial variation in intensity within the pattern) generated by interaction of an incident beam with the cantilever (e.g. reflection from, or transmission through, the cantilever). For example, changes in the shape of peaks and/or troughs in the interference pattern relative to the interference pattern for an undistorted cantilever are

analysed to obtain information about the cantilever deformation.

This approach avoids the alignment problems intrinsic to prior art methods that monitor the deflection of the reflected or transmitted radiation. As a consequence, scaling up to deal with large numbers of cantilevers can be achieved more efficiently. Sensitivity sufficient for biosensing applications can also be achieved more easily.

The method can be implemented using only one laser beam reflected or transmitted from the cantilever. An additional reference beam is not necessary. Furthermore, a point of reference on a cantilever support is not necessary. The present arrangement can therefore be implemented more efficiently.

The problems of chemical cross-contamination and physical cross-talk mentioned above for fixed array-based combinatorial methods, where scale-up is derived from increasing the number and density of elements in the array, can be avoided by untethering the cantilevers from the substrate which anchors them in the traditional scheme, and measuring their deformation when they are free objects in solution, e.g. flowing through a microchannel or suspended in a static solution. The present arrangement is ideally suited to perform this measurement task. The profile of a free floating cantilever can be detected because the information about bending is completely contained in the change of its own interference pattern. The tilt (or change in orientation) of the free floating cantilever can simply be removed from the interference pattern by shifting the signal obtained with the measurement system (CCD).

Embodiments in which the interference pattern is formed by transmission through the cantilever offers particular advantages for confined microfluidic geometries, thus making everyday clinical use less challenging.

Furthermore, the method makes it possible to distinguish between tilting (change in orientation) and deformation (change in shape) of the cantilevers in a single step by deconvolving the interference pattern into these components.

The interference pattern may be formed from the whole of the cantilever. For example, where the cantilever has a broadly rectangular form (in a plane orthogonal to the incident radiation), the interference pattern may resemble a "single-slit" (sinc squared) diffraction pattern. Additionally or alternatively, a micropattern may be formed in the cantilevers and the measurement system may be configured to monitor the intensity variations in

the interference pattern resulting from radiation reflected from or transmitted through the micropattern. In other words, the micropattern may be defined by regions of high relative reflectivity (where the pattern is to be produced by reflection) or by regions of high transmittance (where the pattern is to be produced by transmission). Regions of high transmittance may be produced by chemical etching or mechanical incisions, for example.

Because a micropattern yields a full diffraction pattern with as many numerical intensities as there are pixels in the detector, the deformation of the cantilever can, in principle, be determined with as great a resolution as performing angle of reflection measurements at a number of points on the cantilever similar to the number of aforementioned pixels. Another advantage of the interference method proposed here is that it will work with cantilevers which are largely transparent, or opaque and/or matte (not shiny)

The micropattern may comprise at least one of the following: a regular or irregular array of reflective or transmissive slits; a regular or irregular array of transmissive or reflective spots; a two dimensional array, and combinations thereof.

A two dimensional array is a micropattern which causes the diffraction pattern to have structure in two dimensions rather than just one dimension. This allows information about bending along different axes to be extracted simultaneously from a single interference pattern. Full cantilever curvature tensors and mean tilt can in principle be extracted from such patterns.

Identification information may be added to the micropattern to identify individual cantilevers. The identification information may be extracted from the interference pattern produced by the micropattern as part of the deformation calculating process, for example. Thus, the identity of individual cantilevers can be determined efficiently without additional hardware and/or without further method steps. The same interference pattern can be used both to determine cantilever deformation and to identify the cantilever. This may be particularly important where an array containing a large number of different cantilevers is being measured and/or where the cantilevers are not tethered to a substrate. For example, in a biosensing application, it may be desirable to screen for a large number of different substances simultaneously.

Various optical configurations are possible. One coherent beam or multiple

coherent beams (for example, two, three or more) can be employed to illuminate the cantilever. The effect produced by using multiple coherent beams can be achieved also with a single coherent beam if the cantilever is patterned with a suitable reflective or transmissive diffraction grating.

The use of multiple beams (and/or multiple slits or reflecting elements in a micropattern) produces multiple peaks. This enhances the accuracy of the measurement since tracking multiple peaks at the same time instead of just one peak is better than performing multiple measurements one after another because of the possibility of motion of the cantilever between such measurements and the desire for fast readout.

As mentioned above, atomic force microscopes rely on monitoring the displacements of a cantilever attached to a tip. The bending of the cantilever is measured by detecting the displacement of a reflected laser spot. The interferometric methods proposed here, especially if a two-dimensional pattern is collected, will have many advantages over prior art methodologies. In particular, lateral forces can be inferred from the curvature tensor for the cantilever, and the vertical displacement of the tip can be determined more accurately by measuring the locations of the multiple interference fringes.

Embodiments of the invention will now be described, by way of example only, with reference to the accompanying schematic drawings in which corresponding reference symbols indicate corresponding parts, and in which:

Figure 1 is a schematic depiction of a prior art arrangement for measuring the tilt of a tethered cantilever;

Figure 2A is a schematic illustration of an embodiment of the present invention in which deformations of untethered cantilevers suspended in a static solution are measured;

Figure 2B is a magnified schematic view showing radiation incident on and reflected from cantilevers suspended in a flowing solution;

Figure 3A to 3C show different optical geometries for the radiation projected onto the cantilevers;

Figures 3D and 3E compare bending and tilt of a tethered cantilever (Figure 3D), and bending of an untethered cantilever (Figure 3E);

Figure 3F illustrates an embodiment in which the interference pattern is produced via transmission through a micropattern formed in the cantilever;

Figure 3G illustrates the formation of a two-dimensional interference pattern from a two-dimensional micropattern formed on the cantilever;

Figures 4A to 4E show the results of numerical calculations to predict interference patterns for different cantilever deformation magnitudes: Figure 4A shows the case for a tethered cantilever and single incident beam, Figure 4B shows the case for a rigid tethered cantilever (which can only tilt) and a single incident beam, Figure 4C shows the case for an untethered cantilever and single beam, and Figures 4D and 4E show the situation for multiple incident beams (respectively, two and three); and

Figures 5A to 5H show the results of numerical calculations to predict interference patterns for various geometries of incident radiation and illustrates the use of different metrics to quantify changes in the structure of the interference patterns with deformation of the cantilever.

Figure 1 shows a prior art arrangement for determining the tilt of a tethered cantilever 9. The cantilevers 9 are fixed (tethered) at one end to a chip or substrate 16. A projection system 1 projects a laser beam 5 onto a localized spot on the cantilever 9. A detector 3 detects the reflected beam 7. The angle at which the reflected beam 7 leaves the cantilever 9 is a function of the amount of tilt of the cantilever 9. Measuring the position at which the reflected beam 7 is incident onto the detector can therefore determine the amount of tilt of the cantilever 9. This method depends on accurate alignment of the laser, chip and detector. The method cannot be applied where the cantilevers are untethered, e.g. floating in a static solution or carried in a flow.

Figure 2A shows an apparatus for measuring deformation of a cantilever according to an embodiment of the invention. A projection system 2 is provided for projecting a beam of radiation onto a cantilever to be measured. According to the embodiment, the cantilever to be measured is suspended within a static fluid medium 8 contained in container 10. According to alternative embodiments, the cantilever to be measured may be suspended within a non-static or flowing fluid, in vacuum or in any other gas, including air. The cantilever may also

be fixed at one end to a support (i.e. tethered).

Figure 2B shows a close-up view of a variation in which the cantilevers 18 are suspended in a moving fluid (depicted schematically by arrows 17) rather than a static fluid (as in Figure 2A).

In both cases, the properties of the laser are such that a reflected beam 6 causes an interference pattern from the cantilever to be formed on a detection plane in a measurement system 12. The measurement system 12 is capable of measuring the spatial variation in intensity of the interference pattern. The measurement system 12 may be a charge-coupled device (CCD), for example.

The measurement system 12 is configured so that data can be transferred to a deformation calculating system 14, which is configured to calculate a deformation of the cantilever from the spatial variation in intensity measured in one or two dimensions by the measurement system 12. The deformation calculating system 14 may be implemented using a desktop computer or a dedicated integrated circuit, for example.

The deformation of the cantilever can be extracted from the measured intensity variations in the interference pattern by comparing the measured variations with variations predicted using numerical models and/or calibration measurements.

The results of some numerical studies are discussed further below. Examples of useful metrics for quantifying changes in the interference pattern are also discussed.

Figure 3A shows an arrangement in which the whole of a cantilever 18 is illuminated with a single coherent beam of radiation. In this case, the form of the interference pattern may be defined by the outline of the cantilever 18 (and its deformation). For the flat cantilever, the observed interference pattern is known in the literature as Fraunhofer interference. This arrangement has the advantage of being simple to implement and analyse. The form of the interference pattern, where the cantilever has an elongated rectangular profile, may resemble the sinc-squared pattern formed by diffraction from a single slit. See the discussion below regarding Figures 4A to 4C.

Alternatively or additionally, the projection system 2 may be configured to illuminate only a portion of the cantilever. For example, in the case where the cantilever has a strip-like form, the projection system may be configured to illuminate the cantilever over the

whole of the width of the cantilever for at least a portion of the length of the cantilever. Information about bending of the cantilever about an axis perpendicular to the width may therefore be extracting in detail from the cantilever's interference pattern. In general, the cantilever can have an arbitrary shape, but it may be convenient from a manufacturing point of view to produce rectangular cantilevers. In this case, the width referred to above would correspond to the shortest dimension of the rectangle and the length to the longest dimension.

Figures 3B and 3C show arrangements in which the cantilever is illuminated respectively with two and three coherent laser beams. It is also possible to use even more beams. The coherent beams can be produced by beam splitters. The interference pattern from the reflection of multiple beams can as well be achieved by using the one beam illumination method (Fig. 3A) and micropattern the cantilever with a specific reflective pattern (diffraction grating).

Another implementation of interferometry to measure the bending of microcantilevers is the use of slits, produced e.g. by chemical etching or mechanical incisions, rather than reflecting surfaces, of the cantilevers and to view the associated interference patterns in transmission rather than reflection. Figure 3F illustrates such an arrangement.

These diffraction gratings can also be used as a barcode to identify individual functionalised cantilevers. In this case, a cantilever identification device may be provided to analyse the interference pattern and extract the cantilever identity therefrom. The cantilever identification device functionality may be implemented in software on the desktop computer (e.g. 14 in Figure 2A), for example. Alternatively or additionally, separate hardware for this process may be provided.

The pattern of beams and/or reflecting and/or transmitting areas on the cantilevers can be two-dimensional rather than one-dimensional, resulting in two-dimensional interference patterns from which mean tilt and full curvature tensors can be extracted. Figure 3G illustrates the formation of such a two-dimensional interference pattern.

The proposed systems have been evaluated using numerical simulations. Without loss of generality the simulations have been performed for one-dimensional reflecting patterns, e.g. lines of shiny spots or bars on the cantilevers. For all simulations the following parameters were kept constant. Figs. 3A, B, and C show the geometries and corresponding definitions of parameters. The wavelength was $\lambda = 655$ nm and the CCD was mounted at a

distance of d = 4 cm. For simplicity but without loss of generality the angles were $\theta = \beta = 0$ and $\gamma = \pi / 2$. The cantilever length for all experiments was c = 100 μm.

The results of the simulations are shown in Figure 4, in which the five graphs each contain two or more curves representing interference patterns for different amounts of deformation Δz (i.e. Δz = 0 nm, 100 nm, 500 nm, and 600 nm; see legend).

The first simulation presents the case of a tethered cantilever (illustrated in Figure 3D). The results (Figure 4A) show that in addition to the displacement of the maximum, due to the tilt of the surface normal, there is a change of the peak shape due to the modified Fraunhofer interference pattern from the bending of the cantilever. Two further simulations have been performed to clarify this matter. In one case the cantilever consists of one rigid piece which is attached to a hinge on the chip which cannot bend but can just tilt (see dotted line in Figure 3D). The recorded pattern (Figure 4B) reveals that the entire Fraunhofer pattern is merely shifted. The other case is an untethered cantilever (illustrated in Figure 3E) which just bends but does not tilt. The results (Figure 4C) clearly indicate that only the shape of the interference pattern changes but the pattern does not shift for different Δz. (For small Δz it can be derived that Δz = 4 * Δh.) This shows that the interference pattern can be deconvolved with one part attributed to the tilt of the cantilever while the other part represents the bending only.

The interference pattern for the configuration with two or three laser beams (Figures 4D and 4E) shows the comb–like structure characteristic of multi-slit interferometers. As the cantilever bends, these structures change in easily measurable ways. Most notably, for the two beam/mirror/slit pattern, most of the nodes are lifted from the horizontal axis and assume a sinusoidal pattern (highlighted by the dashed line in Figure 4D), while for the three beam/mirror/slit configuration, the apparent symmetry of the pattern changes (note the evolution from a single peak with maximum intensity to two peaks apparently attaining the maximum, as well as the outlaying peaks gaining intensity on the right hand side of the pattern). Additionally all peak shapes are subject to alteration in respect to Δz. This change is particularly enhanced at the outer peaks.

Again the tilt and the bending have been simulated separately for these optical configurations (Figures 3B and 3C) and confirm that the displacement of the peak can be attributed to the tilt and the change of the peak shape to the bending of the cantilever. The results

are not shown here.

Figure 5 shows the dependence of various metrics derivable from the interference patterns measured on the detector plane. All of the interference patterns shown (Figures 5A, 5C and 5E) result from the bending of the cantilever only, i.e. there is no average tilt. The situation corresponds to the geometry shown in Figure 3E for an untethered cantilever.

Figure 5A shows the interference pattern for reflection from a cantilever according to the optical geometry of Figure 3A, for two different $\Delta z$. Figure 5B shows the amplitudes $A_0$ (solid line) and $A_1$ (dashed line) of the primary and second peaks in intensity of the interference pattern of Figure 5A as a function of $\Delta z$.

Figure 5C shows the interference pattern for reflection from a cantilever according to the optical geometry of Figure 3B. Figure 5D shows the amplitude $A_0$ of the trough marked in Figure 5C as a function of $\Delta z$.

Figure 5E shows the interference pattern for reflection from a cantilever according to the optical geometry of Figure 3C. Figure 5F shows the ratio of the two amplitudes $A_0$ and $A_1$ (corresponding to the heights of the primary peak and a secondary peak in the pattern of Figure 5E). Figure 5G shows the variation of amplitude $A_2$ (the height of a further secondary peak in the pattern of Figure 5E) with $\Delta z$. Figure 5H shows the variation of amplitude $A_3$ (the intensity value in a particular trough in the pattern of Figure 5E) with $\Delta z$.

The various amplitude metrics presented are normalised to the corresponding amplitude at $\Delta z = 0$.

Other metrics could also be used to characterise the shapes of the curves in the interference patterns and provide a measure of deformation-induced changes to the interference patterns. Where the interference pattern has a large amount of structure (e.g. the pattern of Figure 5E in comparison to that of Figures 5A and 5C), in which case it may sometimes also be referred to as a 'speckle pattern', it may be appropriate to use more complex and/or numerous metrics to characterize the pattern. This may be more complicated to implement but may also yield more accurate and/or detailed information about the nature of the deformation of the cantilever.

More generally, metrics of the kind described in the examples above represent

simple algorithms that can be incorporated into software to independently determine average cantilever tilt and curvature.

Embodiments of the present invention can be applied to atomic force microscopes, systems for detecting the presence or absence of a target substance in a fluid (e.g. biosensors), temperature sensors and pressure sensors.

For example, an atomic force microscope may be provided having a cantilever tethered at one end to the tip of a probe and configured to deform as a function of the separation between the tip of the probe and a sample (due to the "tip sample interaction"). An apparatus according to one or more of the embodiments discussed above could conveniently be used to measure the deformation and thereby determine the separation between the tip and sample. Alternatively or additionally, determination of the deformation may yield other useful information about the tip environment.

A system for detecting the presence or absence of a target substance in a fluid may be provided, in which a cantilever is deployed so as to be in contact with the fluid and to deform as a function of the presence or absence of the target substance. An apparatus according to one or more of the embodiments discussed above could conveniently be used to measure (detect) any deformation of the cantilever to thereby detect the presence or absence of the target substance. A plurality of such cantilevers could be deployed to detect the presence or absence of a range of different target substances. The same measurement system could be applied to simultaneously measure the distortions of all or a subset of the cantilevers. Alternatively or additionally, more than one measurement system may be provided.

A temperature sensor may be provided comprising a cantilever which is configured to deform as a function of its temperature. An apparatus according to one or more of the embodiments discussed above could conveniently be used to measure the deformation of the cantilever and thereby determine the temperature of the cantilever. Such a system would also be effective for determining the temperature of an environment and/or neighbouring object(s) with which the cantilever is in thermal equilibrium.

A pressure sensor may be provided comprising a cantilever which is

configured to deform as a function of a pressure gradient in a fluid (or fluids) surrounding at least a portion of the cantilever. The pressure gradient may be at the edge of a fluid conduit or within a fluid, for example. An apparatus according to one or more of the embodiments discussed above could conveniently be used to measure the deformation of the cantilever and thereby measure the pressure gradient or pressure gradients to which the cantilever is subject.

CLAIMS

1. An apparatus for measuring deformation of a cantilever, comprising:

a projection system for projecting a radiation beam onto a cantilever; and

a measurement system for detecting radiation transmitted through or reflected from said cantilever, wherein

said projection system is arranged such that the radiation transmitted through or reflected from said cantilever forms an interference pattern;

said measurement system is configured to measure the spatial variation in intensity within at least a portion of said interference pattern; and

said apparatus further comprises a deformation calculating system for calculating a deformation of said cantilever from the spatial variation in intensity measured by said measurement system.

2. An apparatus according to claim 1, wherein at least a portion of said interference pattern is formed as a result of a transmissive or reflective micropattern formed in or on said cantilever.

3. An apparatus according to claim 2, wherein said micropattern comprises at least one of the following: a regular or irregular array of reflective or transmissive slits; a regular or irregular array of transmissive or reflective spots; a two-dimensional array.

4. An apparatus according to any one of the preceding claims, wherein said micropattern comprises identity information for identifying individual cantilevers, and said apparatus further comprises a cantilever identification device configured to determine the identity of said cantilever by reading the identity information contained in said micropattern.

5. An apparatus according to claim 4, wherein said identification device is configured to read said identity information from the interference pattern measured by said

measurement system.

6. An apparatus according to any one of the preceding claims, wherein the cantilever is freely suspended and/or travelling through a fluid, vacuum or a gas.

7. An apparatus according to any one of the preceding claims, wherein, where said cantilever is formed from a strip of material of arbitrary shape, the projection system is configured to illuminate the cantilever with a coherent beam of radiation that spans the entire width of the cantilever, for at least a portion of the cantilever.

8. An apparatus according to any one of the preceding claims, wherein the projection system is configured to illuminate the whole cantilever with a coherent beam of radiation.

9. An apparatus according to any one of the preceding claims, wherein the projection system is configured to project a plurality of beams onto said cantilever, said interference pattern being formed from said plurality of beams.

10. An apparatus according to any one of the preceding claims, wherein said deformation calculating system is configured to calculate a deformation based on one or more of the following characteristics of the measured spatial variation in intensity:

(i) the shape of at least one intensity peak or intensity trough;

(ii) the width of at least one intensity peak or intensity trough; and

(iii) intensity values at identifiable positions in the interference pattern,

including at least one of a maximum intensity value of an nth order peak, and a minimum intensity value between an nth and an (n+1)th order peak, where n is any integer.

11. An atomic force microscope, comprising:

a cantilever tethered at one end to the tip of a probe and configured to deform as a function of the separation between the tip of the probe and a sample; and

an apparatus for measuring the deformation of the cantilever according to any one of the preceding claims to determine the deflection of the tip because of tip sample interaction.

12. A system for detecting the presence or absence of a target substance in a fluid, comprising:

a cantilever in contact with the fluid and configured to deform as a function of the presence or absence of said target substance; and

an apparatus for measuring the deformation of the cantilever according to any one of claims 1 to 10 to determine the presence or absence of said target substance.

13. A temperature sensor, comprising:

a cantilever configured to deform as a function of its temperature; and

an apparatus for measuring the deformation of the cantilever according to any one of claims 1 to 10 to determine the temperature of the cantilever.

14. A pressure sensor, comprising:

a cantilever configured to deform as a function of a pressure gradient, either at the edge of a fluid conduit or within a fluid; and

an apparatus for measuring the deformation of the cantilever according to any one of claims 1 to 10 to determine said pressure gradient.

15. A method of measuring deformation of a cantilever, comprising:

projecting a radiation beam onto a cantilever; and

detecting radiation transmitted through or reflected from said cantilever, wherein:

said radiation beam is projected onto said cantilever in such a way as to form an interference pattern in said transmitted or reflected radiation; and

said method further comprises:

measuring the spatial variation in intensity within at least a portion of said

interference pattern; and

calculating a deformation of said cantilever from the measured spatial variation in intensity.

16. A method according to claim 15, wherein said interference pattern is formed as a result of a transmissive or reflective micropattern formed in or on said cantilever.

17. A method according to claim 15 or 16, wherein said micropattern comprises identity information for identifying individual cantilevers, and said method further comprises determining the identity of said cantilever by reading the identity information contained in said micropattern.

18. A method according to claim 17, wherein said identity information is read from the measured interference pattern.

19. A method according to any one of claims 15 to 18, further comprising providing said cantilever freely suspended and/or travelling in a fluid, vacuum or a gas.

20. A method according to any one of claims 15 to 18, further comprising providing said cantilever tethered at one end to a substrate.

21. A method according to any one of claims 15 to 20, further comprising projecting a plurality of beams onto said cantilever, said interference pattern being formed from said plurality of beams.

22. Apparatus for measuring deformation of a cantilever constructed and arranged to operate substantially as hereinbefore described with reference to and as illustrated in the accompanying drawings.

23. Method of measuring deformation of a cantilever substantially as hereinbefore

described with reference to and as illustrated in the accompanying drawings.

WO 2008/129272 PCT/GB2008/001375



FIG. 1

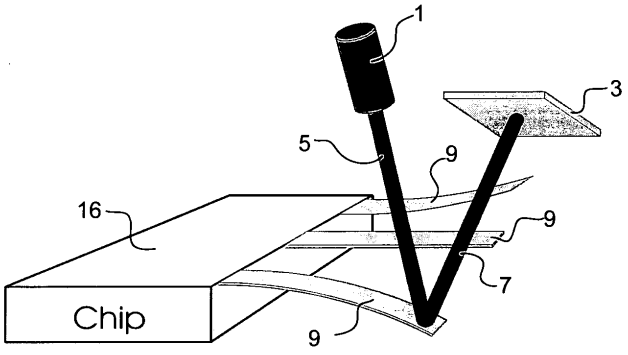


PRIOR ART

WO 2008/129272 PCT/GB2008/001375



FIG. 2A

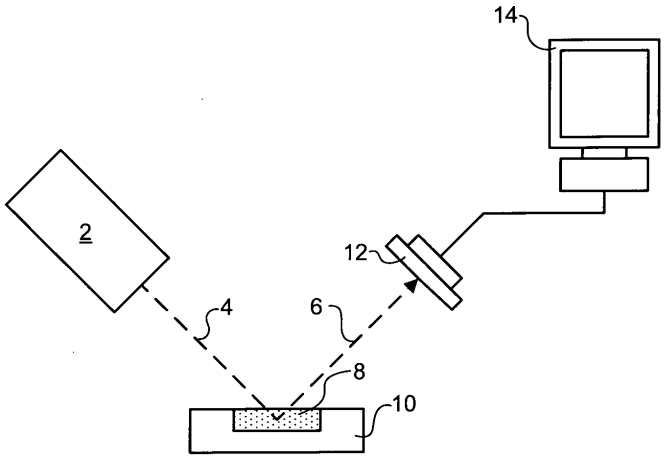


FIG. 2B

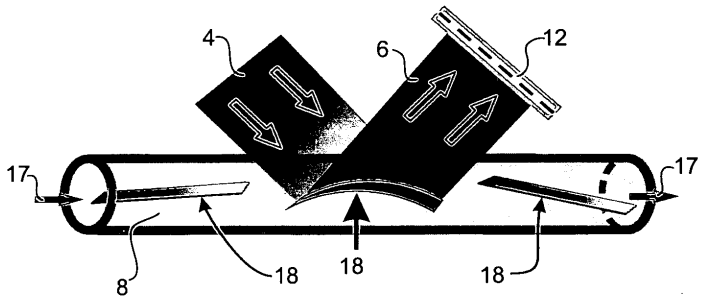

WO 2008/129272 PCT/GB2008/001375



FIG. 3

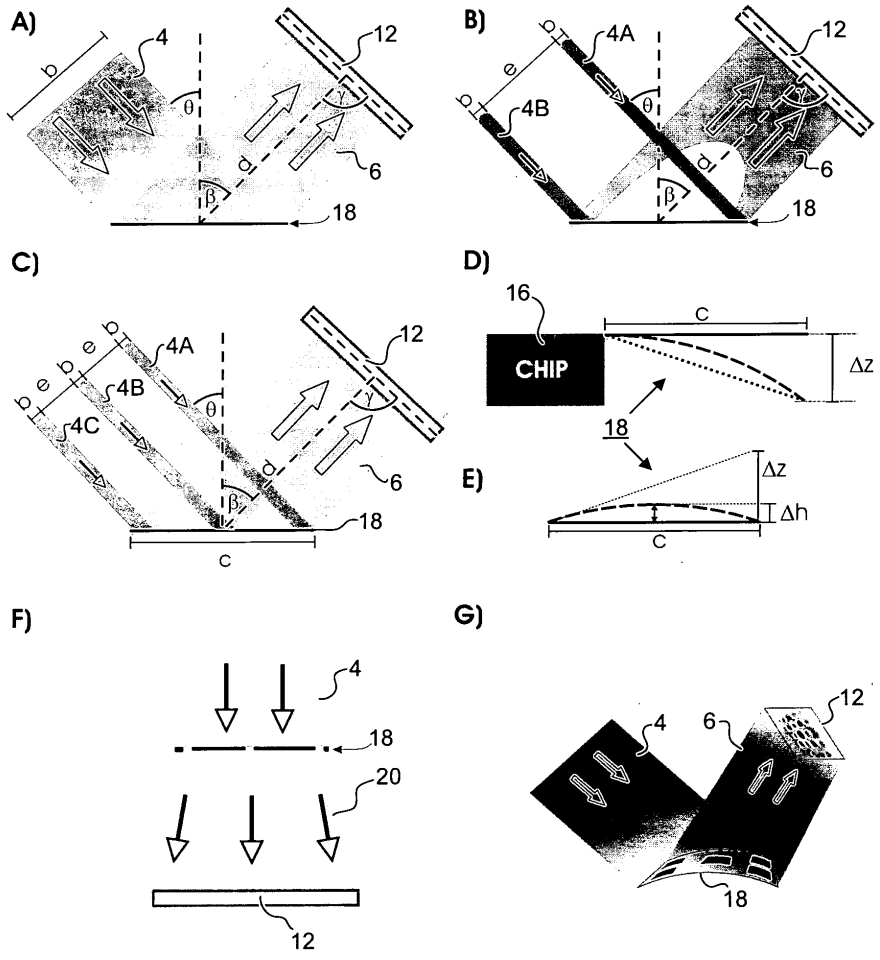

FIG.4

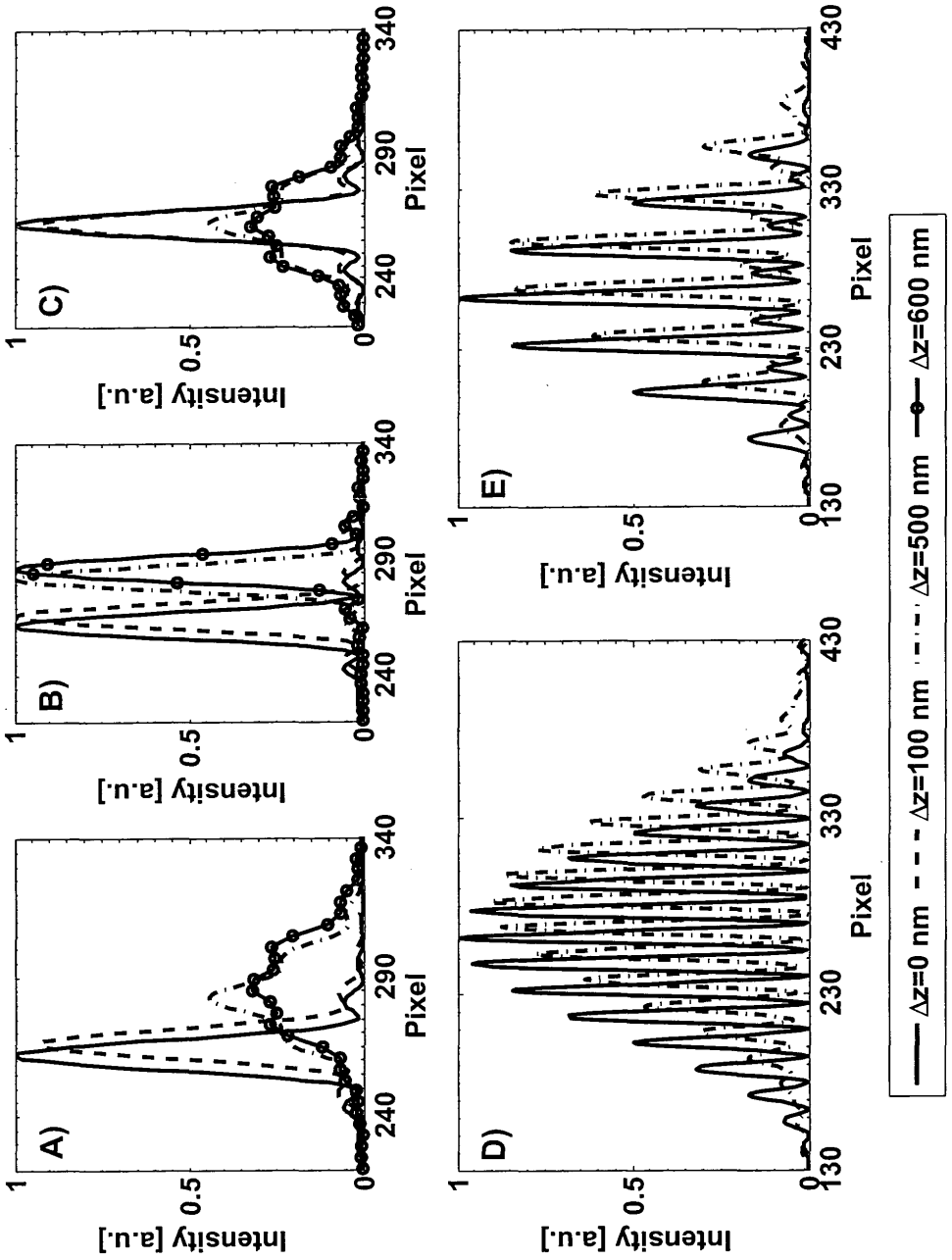

FIG.5

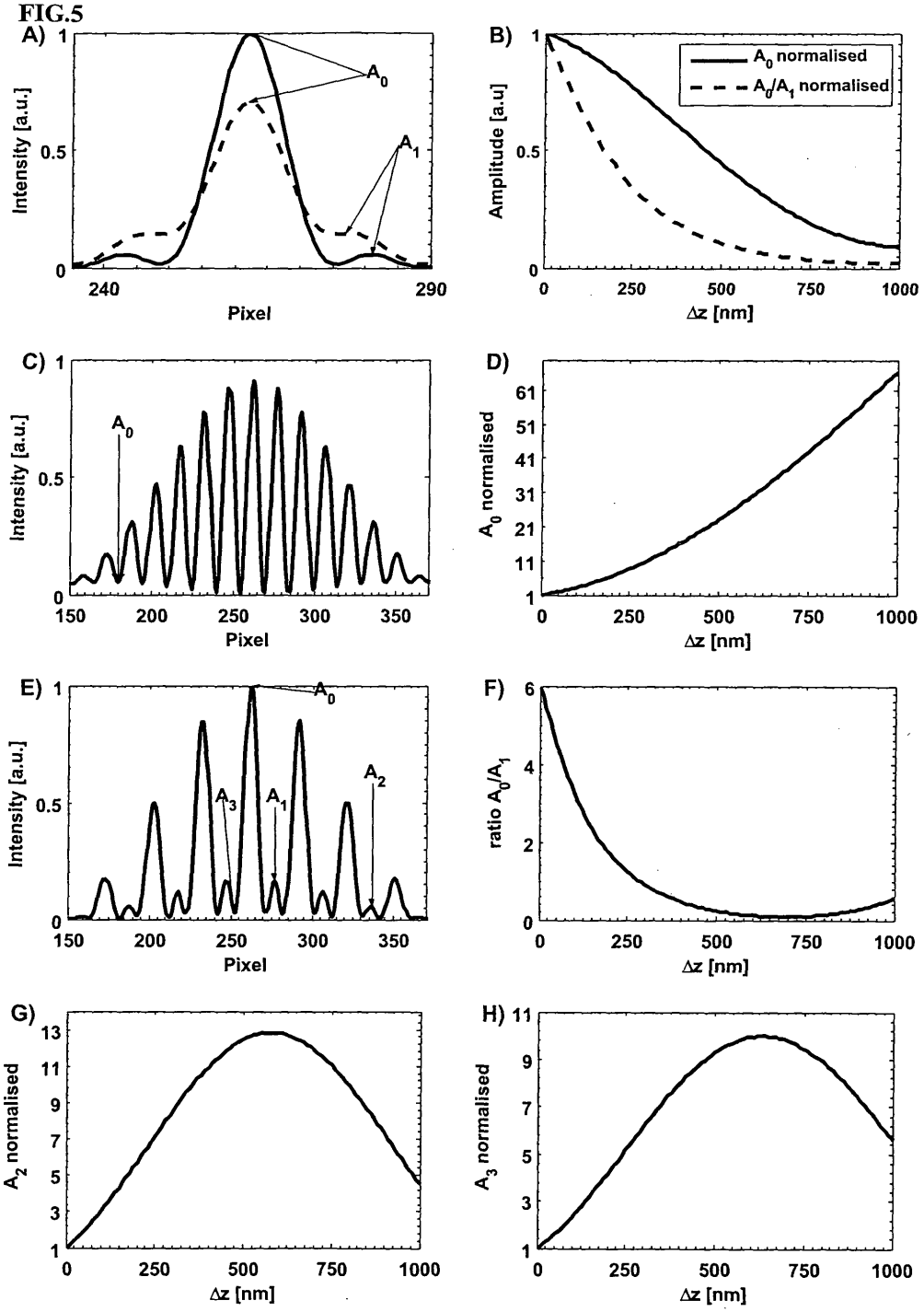
A)
Intensity [a.u.]
Pixel
$A_0$
$A_1$
B)
Amplitude [a.u]
Δz [nm]
$A_0$ normalised
$A_0/A_1$ normalised
C)
Intensity [a.u.]
Pixel
$A_0$
D)
$A_0$ normalised
Δz [nm]
E)
Intensity [a.u.]
Pixel
$A_0$
$A_1$
$A_2$
$A_3$
F)
ratio $A_0/A_1$
Δz [nm]
G)
$A_2$ normalised
Δz [nm]
H)
$A_3$ normalised
Δz [nm]

# INTERNATIONAL SEARCH REPORT

International application No
PCT/GB2008/001375

**A. CLASSIFICATION OF SUBJECT MATTER**
INV. G12B21/20

According to International Patent Classification (IPC) or to both national classification and IPC

**B. FIELDS SEARCHED**

Minimum documentation searched (classification system followed by classification symbols)
G01B G12B

Documentation searched other than minimum documentation to the extent that such documents are included in the fields searched

Electronic data base consulted during the international search (name of data base and, where practical, search terms used)
EPO-Internal, WPI Data

**C. DOCUMENTS CONSIDERED TO BE RELEVANT**

| Category* | Citation of document, with indication, where appropriate, of the relevant passages | Relevant to claim No. |
|---|---|---|
| X | US 6 196 061 B1 (ADDERTON DENNIS M [US] ET AL) 6 March 2001 (2001-03-06)<br>figures 1-4<br>column 7, line 60 - column 8, line 54 | 1-3,6,7,<br>10-16,<br>19,20,<br>22,23 |
| Y | claims 8,13 | 1-23 |
| X | US 6 075 585 A (MINNE STEPHEN CHARLES [US] ET AL) 13 June 2000 (2000-06-13)<br>figure 15b<br>column 13, line 54 - line 62 | 1,11,15,<br>20,22,23 |
| Y | | 1-23 |
| Y | EP 0 706 052 A (MATSUSHITA ELECTRIC IND CO LTD [JP]) 10 April 1996 (1996-04-10)<br>column 22, line 7 - line 13 | 12-14 |

-/--

[X] Further documents are listed in the continuation of Box C. [X] See patent family annex.

* Special categories of cited documents :

"A" document defining the general state of the art which is not considered to be of particular relevance
"E" earlier document but published on or after the international filing date
"L" document which may throw doubts on priority claim(s) or which is cited to establish the publication date of another citation or other special reason (as specified)
"O" document referring to an oral disclosure, use, exhibition or other means
"P" document published prior to the international filing date but later than the priority date claimed
"T" later document published after the international filing date or priority date and not in conflict with the application but cited to understand the principle or theory underlying the invention
"X" document of particular relevance; the claimed invention cannot be considered novel or cannot be considered to involve an inventive step when the document is taken alone
"Y" document of particular relevance; the claimed invention cannot be considered to involve an inventive step when the document is combined with one or more other such documents, such combination being obvious to a person skilled in the art.
"&" document member of the same patent family

| Date of the actual completion of the international search | Date of mailing of the international search report |
|---|---|
| 19 June 2008 | 27/06/2008 |
| **Name and mailing address of the ISA/**<br>European Patent Office, P.B. 5818 Patentlaan 2<br>NL – 2280 HV Rijswijk<br>Tel. (+31–70) 340–2040, Tx. 31 651 epo nl,<br>Fax: (+31–70) 340–3016 | **Authorized officer**<br>Grand, Jean-Yves |

3

Form PCT/ISA/210 (second sheet) (April 2005)

**INTERNATIONAL SEARCH REPORT**

International application No
PCT/GB2008/001375

C(Continuation). DOCUMENTS CONSIDERED TO BE RELEVANT

| Category* | Citation of document, with indication, where appropriate, of the relevant passages | Relevant to claim No. |
|---|---|---|
| Y | US 5 103 174 A (WANDASS JOSEPH H [US] ET AL) 7 April 1992 (1992-04-07) column 16, line 43 - line 52 | 12-14 |

## INTERNATIONAL SEARCH REPORT

Information on patent family members

International application No
PCT/GB2008/001375

| Patent document cited in search report | Publication date | Patent family member(s) | Publication date |
|---|---|---|---|
| US 6196061 B1 | 06-03-2001 | US 6279389 B1 | 28-08-2001 |
| US 6075585 A | 13-06-2000 | NONE | |
| EP 0706052 A | 10-04-1996 | DE 69529446 D1 | 27-02-2003 |
| | | DE 69529446 T2 | 02-10-2003 |
| | | US 5679888 A | 21-10-1997 |
| US 5103174 A | 07-04-1992 | NONE | |

Form PCT/ISA/210 (patent family annex) (April 2005)

# B

# Matlab Codes

## B.1 Ray Tracing the Reflected Beam

For all experiments I used the conventional beam deflection method as a built in control to benchmark all the different diffraction approaches. Since a lens was placed between the cantilever and the CCD in the beam which was reflected from the cantilever surface I wrote a ray tracing procedure to calculate the calibration constant which relates the deflection measured in pixel to a deflection $\Delta z$ of the free end of the cantilever in units of meter. The ray tracing approach uses Snell's law to calculate the refraction at all surface between the cantilever to the CCD. This is described in chapter 6.2 of the textbook "Optics" by Eugene Hecht [94].

```
%%%%%%%%%%%%% BEGIN %%%%%%%%%%%%%
function output=raytrace_reflection_optics(bending,show_ray)

  %constant apply to lens order no LB1471-A (Thorlabs Ltd/UK)
  thickness_lens=5.3e-3;
  focal_length=50.2e-3;
  BK7=1.51509; %for 632.8nm

  %distance between cantilever and lens
  dist_canti_lens=50.0e-3;

  %distance between lens and CCD
  dist_lens_CCD=135e-3;

  pixel_size_CCD=4.65e-6;

  refrac_index_lens=BK7;
  refrac_index_air=1;

  delta_z=bending;

  alpha_i1=delta_z*4/500e-6;
  D1=(refrac_index_lens-refrac_index_air)./focal_length;
  y1=alpha_i1*dist_canti_lens;
  alpha_t1=(refrac_index_air*alpha_i1-D1*y1)/refrac_index_lens;
  y2=y1+alpha_t1*thickness_lens;
  alpha_i2=-alpha_t1;
```

```
28    D2=(refrac_index_air-refrac_index_lens)./(focal_length);
29    alpha_t2=(refrac_index_lens*alpha_i2-D2*y2)/refrac_index_air;
30    y3=y2-alpha_t2*dist_lens_CCD;
31
32    if show_ray==true  %then show raytrace in figure
33      plot([0 dist_canti_lens dist_canti_lens+thickness_lens
34      dist_canti_lens+thickness_lens+dist_lens_CCD],[0 y1 y2 y3])
            ;
35    end
36
37  output(1,:)={'bending␣in␣pixel' 'm␣per␣pixel'};
38  output(2,:)={num2str(y3/pixel_size_CCD) ..
39                .. num2str(bending/(y3/pixel_size_CCD))};
40  %%%%%%%%%%%%% END %%%%%%%%%%%%%
```

## B.2 Extract the Shift of Peaks

This function allows to track the shift of peaks between two diffraction pattern by calculating the least square difference and fitting a parabola to the area of the minimum to achieve sub-pixel accuracy.

```
1   %%%%%%%%%%%%% BEGIN %%%%%%%%%%%%%
2   function [pattern_new shift] = unshift(pattern_orig, pos,
        hwidth)
3
4   res = 1e-2;
5
6   % this factor determines how much bigger the part is with which
        the
7   % template is compared
8   buffer_factor = 1.3;
9
10  % determine the nr of diffraction pattern
11  sample_nr = size(pattern_orig,1);
12
13  % initialise the array which stores the shift of each pattern
14  shift(1:sample_nr) = 0;
15
16  % init pattern
17  reg_template = (pos-hwidth):1:(pos+hwidth);
18  reg_template_interp = (pos-hwidth):res:(pos+hwidth);
19  pattern_template = interp1(reg_template,pattern_orig(1,
        reg_template),reg_template_interp);
20
21  for k=1:sample_nr
22
23      % this is the size of buffer pattern
24      reg_buffer = (pos-round(hwidth*buffer_factor)):1:(pos+round
            (hwidth*buffer_factor));
25      reg_buffer_interp = (pos-round(hwidth*buffer_factor)):res:(
            pos+round(hwidth*buffer_factor));
26
27      % variable holds the difference between difference
28      temp_diff(1:(2*round(hwidth*(buffer_factor-1))))=0;
29
30      % create interpolated pattern for comparison
```

```
31      pattern_buffer = interp1(reg_buffer,pattern_orig(k,
            reg_buffer),reg_buffer_interp);
32
33      % slide template over buffer and record the difference for
            each
34      % position
35      for j=1:(2*round(hwidth/res*(buffer_factor-1)))
36          temp_diff(j)=sum(sqrt( (pattern_buffer(j+(0:round(
                hwidth/res*2)))-pattern_template).^2 ));
37
38      end
39
40      [x y]=min(temp_diff);
41
42      shift(k)=(y-1 - round(hwidth*(buffer_factor-1))/res);
43      pos = pos + round(shift(k)*res);
44
45      if k>1
46          shift(k)=shift(k-1)+shift(k);
47      end
48
49      % the template
50      reg_template = (pos-hwidth):1:(pos+hwidth);
51      reg_template_interp = (pos-hwidth):res:(pos+hwidth);
52      pattern_template = interp1(reg_template,pattern_orig(k,
            reg_template),reg_template_interp);
53
54      k
55  end
56
57  max_shift=max(abs(shift));
58
59  % length of pattern
60  pattern_length = size(pattern_orig,2);
61
62
63  for k=1:sample_nr
64
65      pattern_buffer=interp1(pattern_orig(k,:),1:res:(
            pattern_length+1),'spline');
66
67      pattern_new_interp(round((max_shift-shift(k)))+(1:((
            pattern_length-1)/res)))=pattern_buffer(1:round((
            pattern_length-1)/res));
68
69      pattern_new(k,:)=pattern_new_interp(1:100:((pattern_length
            -1)/res));
70  end
71
72
73  end
74  %%%%%%%%%%%%% END %%%%%%%%%%%%%
```

## B.3 Analyse the Expansion and Shift of Peaks

The width of the diffraction peak could be determined for the reflective diffraction technique by tracking the shift of both ends of the peak and calculate the width by subtracting one from the other. Sometimes it is difficult to determine both ends exactly and therefore the following code using affine mapping was used to determine the stretching of one diffraction pattern in comparison to a reference.

```
%%%%%%%%%%%%% BEGIN %%%%%%%%%%%%%
function min_lq_error = affine_mapping(pattern_orig, pattern_2,
     x_shift, x_scale, y_shift, y_scale)

interp_method='linear';

min_lq_error=[1e30 0 0 0 0];
if size(x_shift,2) > 1
  x_shift_res=abs(x_shift(2)-x_shift(1));
else
  x_shift_res=1;
end

%x shift
for c_xshift=1:size(x_shift,2)
  %x scaling
  for c_xscale=1:size(x_scale,2)
    %y shift
    for c_yshift=1:size(y_shift,2)
      %y scaling
      for c_yscale=1:size(y_scale,2)

        %perform the y scaling and y shift
        pattern_temp=pattern_orig*y_scale(c_yscale)+y_shift(
            c_yshift);

        %perform the x scaling - starting from 0 otherwise we
            add a             %shift to the stretching.
        if x_scale(c_xscale) ~= 1
          pattern_temp=interp1(pattern_temp,1:(1/x_scale(
              c_xscale)):(size(pattern_temp,2))/x_scale(
              c_xscale), interp_method);
          pattern_temp=pattern_temp(~isnan(pattern_temp));
        end

        %interpolate to shift by sub pixel values
        if x_shift(c_xshift) < 0
          if x_shift_res ~= 0
            pattern_temp=interp1(pattern_temp, 1:x_shift_res:
                size(pattern_temp,2), interp_method);
          end
          pattern_orig_temp=pattern_temp( 1+round((abs(x_shift(
              c_xshift)./x_shift_res))):round(1/x_shift_res):(
              size(pattern_temp,2)));
          if size(pattern_2,2)>size(pattern_orig_temp,2)
            pattern_2_temp=pattern_2(1:size(pattern_orig_temp
                ,2));
          else
```

```
40              pattern_orig_temp=pattern_orig_temp(1:size(
                    pattern_2,2));
41              pattern_2_temp=pattern_2;
42            end
43          elseif x_shift(c_xshift) > 0
44            if x_shift_res ~= 0
45              pattern_2_t1=interp1(pattern_2,1:x_shift_res:size(
                    pattern_2,2), interp_method);
46            end
47            pattern_2_temp=pattern_2_t1(1+(round(abs(x_shift(
                  c_xshift)./x_shift_res))):round(1/x_shift_res):(
                  size(pattern_2_t1,2)));
48
49            if size(pattern_2_temp,2)>size(pattern_temp,2)
50              pattern_2_temp=pattern_2_temp(1:size(pattern_temp
                    ,2));
51              pattern_orig_temp=pattern_temp;
52            else
53              pattern_orig_temp=pattern_temp(1:size(
                    pattern_2_temp,2));
54            end
55          else
56            if size(pattern_temp,2)>size(pattern_2,2)
57              pattern_2_temp=pattern_2;
58              pattern_orig_temp=pattern_temp(1:size(pattern_2,2))
                    ;
59            else
60              pattern_2_temp=pattern_2(1:size(pattern_temp,2));
61              pattern_orig_temp=pattern_temp;
62            end
63          end
64          lq_error(c_xshift,c_xscale,c_yshift,c_yscale)=sum(((
                pattern_2_temp-pattern_orig_temp).^2/size(
                pattern_2_temp,2)));
65          if min_lq_error(1)> lq_error(c_xshift,c_xscale,c_yshift
                ,c_yscale)
66            min_lq_error(:)=[lq_error(c_xshift,c_xscale,c_yshift,
                  c_yscale) x_shift(c_xshift) x_scale(c_xscale)
                  y_shift(c_yshift) y_scale(c_yscale)];
67          end
68        end
69      end
70    end
71  end
72  %%%%%%%%%%%%%% END %%%%%%%%%%%%%%
```

## B.4 Diffractive Readout with Lens

The Matlab code shown below numerically calculates a diffraction pattern for the following case: $z_1 = 52\,\text{mm}$, $z_2 = 95\,\text{mm}$, $f = 50.2\,\text{mm}$ and a deflection of $\Delta z = -1\,\mu\text{m}$ at the free end of the cantilever. The definition of the variables and the derivation of the calculation can be found in Sec. 2.5.

```
1  % Calculate the diffraction pattern and changes in it due to deformation
2  % of the cantilever, including of placing a converging lens in the beam
3  % between the cantilever and the CCD
```

```
4  %
5  % (C) by Benjamin Dueck (2009)
6  % initialise parameters ******************************************
7
8  %sampling resolution for cantilever and lens
9  sampling_res=1e-7;
10
11 %cantilever - lens distance
12 z1=52e-3;
13 %lens - ccd distance
14 z2=95e-3;
15
16 %properties of laser
17 laser_lambda=632.8e-9;
18 laser_k=2*pi/laser_lambda;
19
20 %properties of cantilever
21 cantilever_base_length=500e-6;
22 cantilever_length=500e-6;
23 cantilever_base_height=5e-6;
24 cantilever_deflection=-10e-6;
25
26 %properties of lens
27 lens_f=50.2e-3;
28 lens_pupil=10e-3;
29 lens_coordinate=(0:sampling_res:lens_pupil)-lens_pupil/2;
30
31 %properties of CCD
32 CCD_pixelsize=6.54e-6;
33 CCD_pixels=500;
34 CCD_length=CCD_pixelsize*CCD_pixels;
35 CCD_coordinate=(0:CCD_pixelsize:CCD_length)-CCD_length/2;
36 %initalise CCD
37 CCD_image(1:CCD_pixels)=0;
38 image_plane(1:CCD_pixels)=0;
39
40 %generate field of a planewave just being reflected from the cantilever
       and
41 %chipbase, the amplitude will be set to zero and the phase of the wave
42 %depends on the deformation of the cantilever
43 %the phase is set to zero at chip surface level
44 cantilever_field(1,1:round(cantilever_base_length/sampling_res))=(0:
       sampling_res:(cantilever_base_length-sampling_res));
45 cantilever_field(2,1:round(cantilever_base_length/sampling_res))=1;
46 %cantilever length
47 cantilever_field(1,round(cantilever_base_length/sampling_res)+(1:round(
       cantilever_length/sampling_res)))=(cantilever_base_length+(
       sampling_res:sampling_res:cantilever_length));
48 cantilever_field(2,round(cantilever_base_length/sampling_res)+(1:round(
       cantilever_length/sampling_res)))=exp(i*laser_k*2*(
       cantilever_base_height+cantilever_deflection*((0:sampling_res:(
       cantilever_length-sampling_res))/cantilever_length).^2));
49
50 for CCD_iter=1:CCD_pixels
51     tic
52     for cantilever_iter=1:size(cantilever_field,2)
53         for lens_iter=1:size(lens_coordinate,2)
```

```
54              buf_fac1=exp(i*laser_k/(2*z1)*cantilever_field(1,
                    cantilever_iter)^2);
55              buf_fac2=exp(i*laser_k/2*(1/z1+1/z2-1/lens_f)*lens_coordinate
                    (lens_iter).^2);
56              buf_fac3=exp(-i*laser_k*(cantilever_field(1,cantilever_iter)/
                    z1+CCD_coordinate(CCD_iter)/z2)*lens_coordinate(lens_iter)
                    );
57
58              image_plane(CCD_iter)=image_plane(CCD_iter)+buf_fac1*buf_fac2
                    *buf_fac3*cantilever_field(2,cantilever_iter);
59          end
60
61      end
62      toc
63      [CCD_iter cantilever_iter lens_iter]
64      CCD_image(CCD_iter)=image_plane(CCD_iter).*conj(image_plane(CCD_iter)
            );
65  end
```

# C

# Different Bending Profiles

Beam theory distinguishes between different loading models of cantilevers which lead to different bending profiles [134]. The coordinate system used here is defined in Fig. 1.14a on page 40.

First, the uniform load model is used when the force $F$ acting on a cantilever is uniform over its length $l$ along the $x$-axis, i.e. $\mathrm{d}F/\mathrm{d}x{=}0$. The deflection $z$ as a function of $x$ is described by

$$z\left(x\right) \propto x^4 - 4x^3 l + 6x^2 l^2$$

Second, the point load model is used when a force acts only at the free end of the cantilever which is described by

$$z\left(x\right) \propto x^3 - 3lx^2$$

Third, the applied moment model deals with cases where a bending moment is applied at the free end of the cantilever. Its bending is described by

$$z\left(x\right) \propto x^2$$

As the equations reveal, all three cases lead to a different bending profile as shown in Fig. C.1.

When the cantilever bending is induced by temperature change or changes in surface stress the cantilever exhibits a constant curvature. This has also been confirmed experimentally previously by our group [45, 53]. The homogeneous bending is also a necessary condition for Stoney's equation (Eq. 1.1) to hold true.

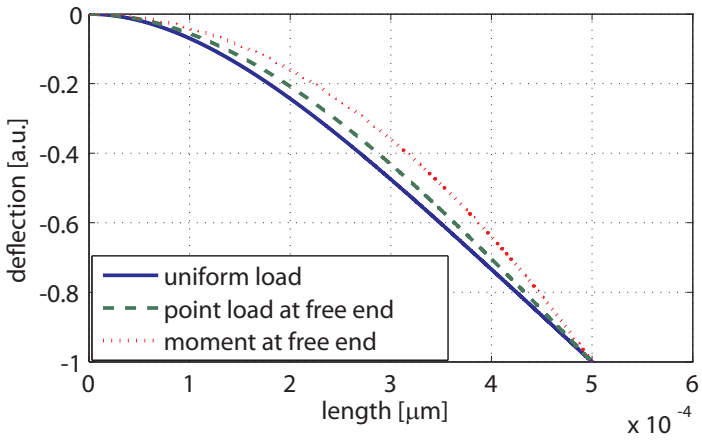


Figure C.1: Different cantilever bending profiles for the same deflection at the free end of the cantilever.

# D

# List of Parts and Supplier Details

Table D.1 lists the contact details of every company which supplied parts for the experimental setup. The parts used are listed in Table D.2.

| **Supplier no** | **Company name** | **Address** |
|---|---|---|
| 1 | Bio-Chem Fluidics | 2 College Park<br>Coldhams Lane<br>Cambridge CB1 3HD<br>United Kingdom<br>www.biochemfluidics.com |
| 2 | Carl Zeiss Ltd. | PO Box 78<br>Welwyn Garden City<br>Herts AL7 1LU<br>United Kingdom<br>www.micro-shop.zeiss.com |
| 3 | Conrad Electronic UK Ltd | PO Box 1318<br>Barking IG11 1ES<br>United Kingdom<br>www.conrad-uk.com |
| 4 | Edmund Optics Inc. | Tudor House<br>Lysander Close<br>York YO30 4XB<br>United Kingdom<br>www.edmundoptics.com |
| 5 | Electron Dynamics | Unit 11 Kingsbury House<br>Kingsbury Road, Bevios Valley<br>Southampton, SO14 0JT<br>United Kingdom<br>www.electrondynamics.co.uk |

| Supplier no | Company name | Address |
|---|---|---|
| 6 | Hamamatsu Photonics UK Ltd | 2 Howard Court, 10 Tewin Road<br>Welwyn Garden City<br>Hertfordshire AL7 1BW<br>United Kingdom<br>www.hamamatsu.co.uk |
| 7 | Hamilton Bonaduz AG | P.O. Box 26<br>CH-7402 Bonaduz, GR<br>Switzerland<br>www.hamiltoncompany.com |
| 8 | Newport Ltd | 4329 First Avenue<br>Newbury Business Park<br>London Road, Newbury<br>Berkshire RG14 2PZ<br>www.newport.com |
| 9 | Pico Technology | James House, Marlborough<br>Road Colmworth Business Park<br>Eaton Socon, St Neots<br>Cambridgeshire PE19 8YP<br>United Kingdom<br>www.picotech.com |
| 10 | The Imaging Source Europe GmbH | Sommerstrasse 36<br>28215 Bremen<br>Germany<br>www.theimagingsource.com |
| 11 | Thermo Electric Devices | Unit 1<br>Draycott Business Centre<br>Draycott Gloucestershire GL56<br>9JY<br>United Kingdom<br>www.thermoelectricdevices.co.uk |
| 12 | Thorlabs Ltd | 1 Saint Thomas PlaceEly<br>Cambridgeshire CB7 4EX<br>United Kingdom<br>www.thorlabs.com |
| 13 | WZW OPTIC AG | Wegenstrasse 18<br>Postfach 42<br>CH-9436 Balgach<br>Switzerland<br>www.wzw.ch |

| Supplier no | Company name | Address |
|---|---|---|
| 14 | Polymax LTD | Polymax Ltd<br>Building 90, SEME<br>Budds Lane, Bordon<br>Hampshire GU35 0JE<br>United Kingdom<br>www.polymax.co.uk |

Table D.1: List of Suppliers

| No | Description | Supplier no | Stock no. | Price |
|---|---|---|---|---|
| | **Optical equipment** | | | |
| | Spherical lens f=50 mm | 12 | LB1471-A | £22.76 |
| | Spherical lens f=250 mm | 12 | LB1056-A | £21.23 |
| | Cylindrical lens f=100 mm | 4 | LA1050-A | £22.10 |
| | Microscope objective 2.5x/0.06 | 2 | 441010-9901-000 | |
| | Neutral density filters | 4 | FW1AND | £205.10 |
| | Back window for cell | 13 | see drawing p.176 | €150.00 |
| | Back window (AR coating) for cell | 13 | n.A. | €220.00 |
| | Front window (AR coating) | 13 | RS20X2-01 | €54.00 |
| | **Lasers, CCD and power supplies** | | | |
| | HeNe - Laser | 12 | HRR050 | £511.00 |
| | Diode Laser | 12 | NT57-108 | £245.00 |
| | Power Supply for diode Laser | 3 | PS2403-0 | |
| | Hamamatsu CCD Camera | 6 | C4742-80-12AG | ≈£15,000 |
| | Firewire CCD Color Camera | 10 | DFK-31AF03 | €590.00 |
| | **Temperature Control** | | | |
| | Peltier with Centre Hole | 11 | SH1.0-95-05L | £22.25 |
| | Temperature Controller Module TCM 10 | 5 | TCM 10-MOD | £320.00 |
| | Power Supply for Peltier and Controller Module | 5 | PSUB 15V20A | £95.00 |
| | Temperature Sensor for TCM 10 | 5 | TCM-PT1000-2M | £25.00 |
| | Temperature Logger Picotech | 9 | TC-08 USB | £249.00 |

| No | Description | Supplier no | Stock no. | Price |
|---|---|---|---|---|
| | Thermocouple for picotech (k-Type) | 9 | SE027 | £8.00 |
| | **Fluidics** | | | |
| | Hamilton Valve Controller - MVP | 7 | 77808 | |
| | Distribution Valve (6 ports) | 7 | 36760 | |
| | Semi-Rigid PTFE tubing (1/16 x 0.031 PTFE tubing - 20m) | 1 | 008T16-080-20 | £17.50 |
| | Tube connectors to fluid cell (Omni-Lok Type S) | 1 | 008FK16 | £14.65 |
| | Manual 3-way valve | 1 | 002422 | £50.60 |
| | O-Rings | 14 | n.A. | |
| | **Stage** | | | |
| | Kinematic stage according to quote QJBR1170 | 8 | Quote | £28,174.53 |

Table D.2: List of Parts

# E

# Drawings

This chapter contains drawings for all parts of the fluid cell. These drawings can be found as AutoCAD®files on the DVD accompanying this publication.

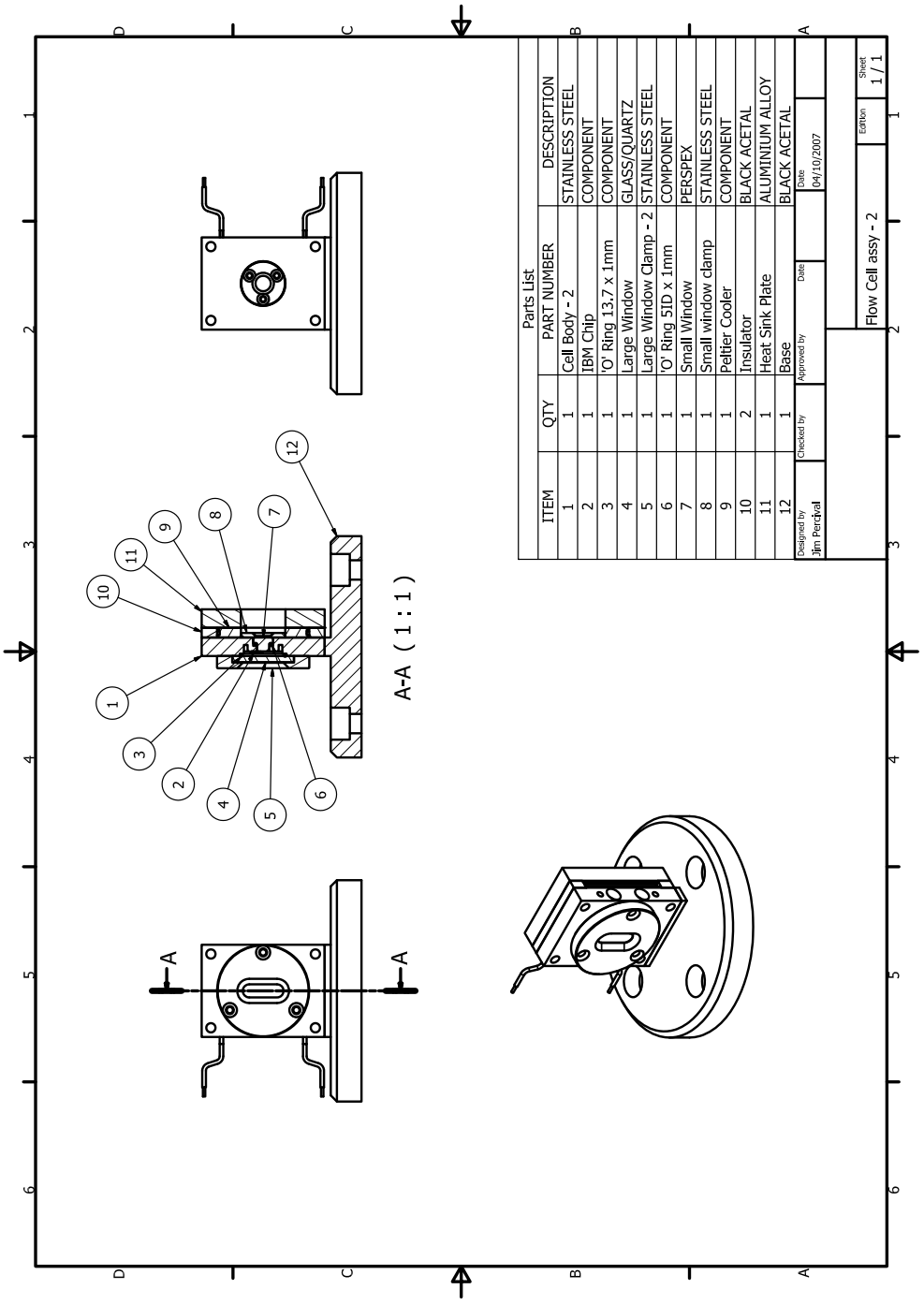


Figure E.1: Assembly drawing of the flow cell

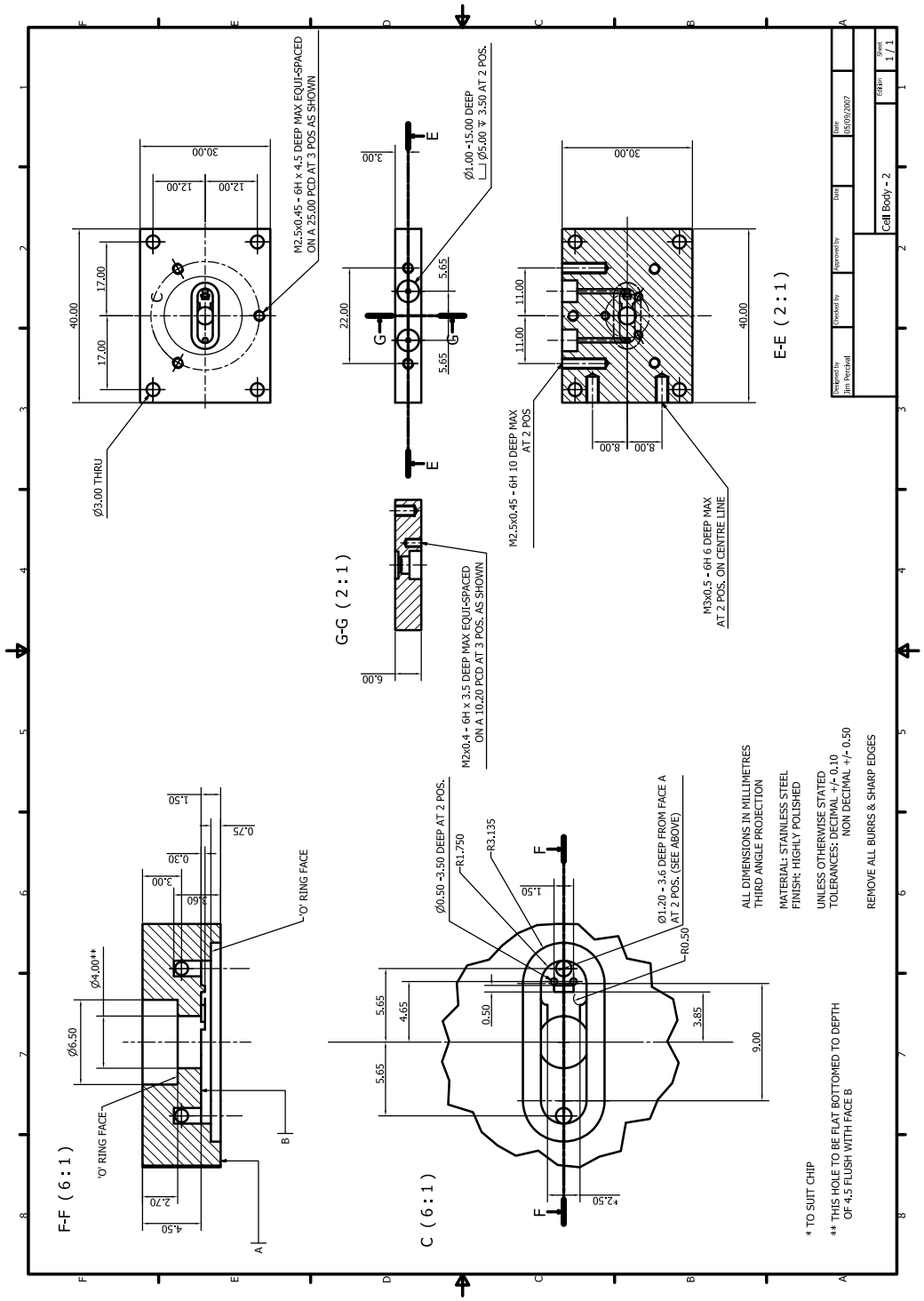


Figure E.2: Body of the flow Cell

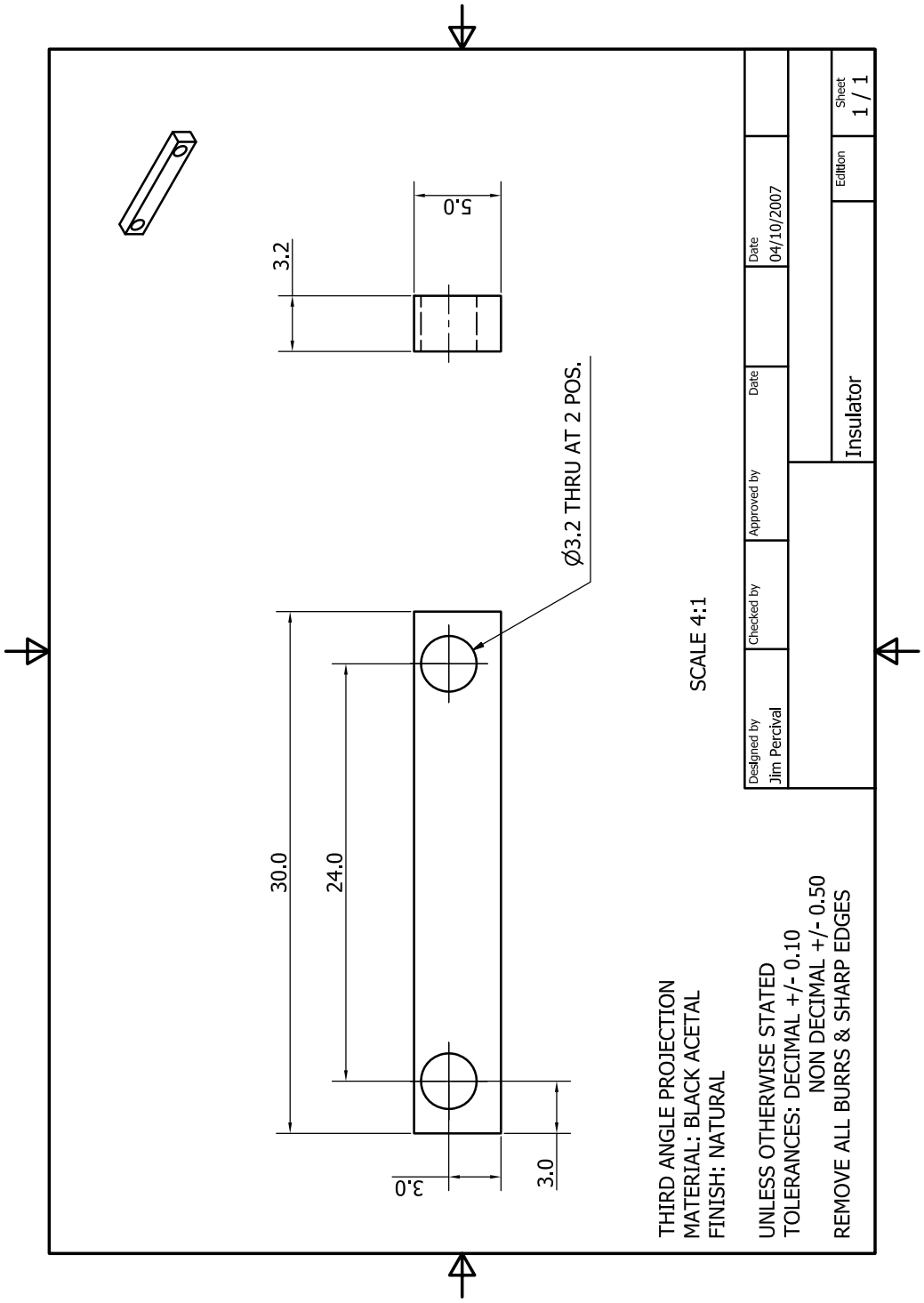


Figure E.3: Insulator to uncouple cell body and heat sink

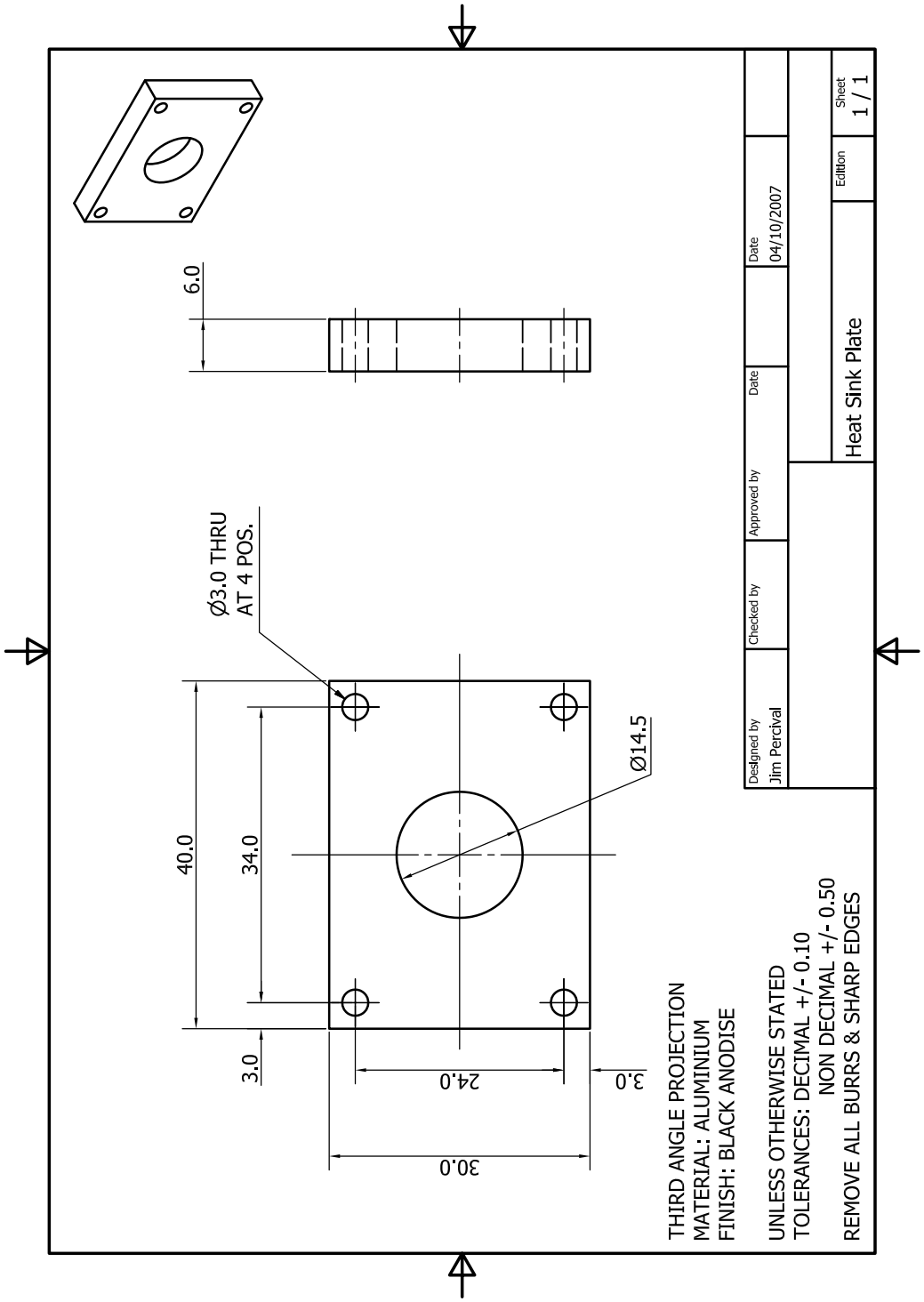


Figure E.4: Heat sink plate

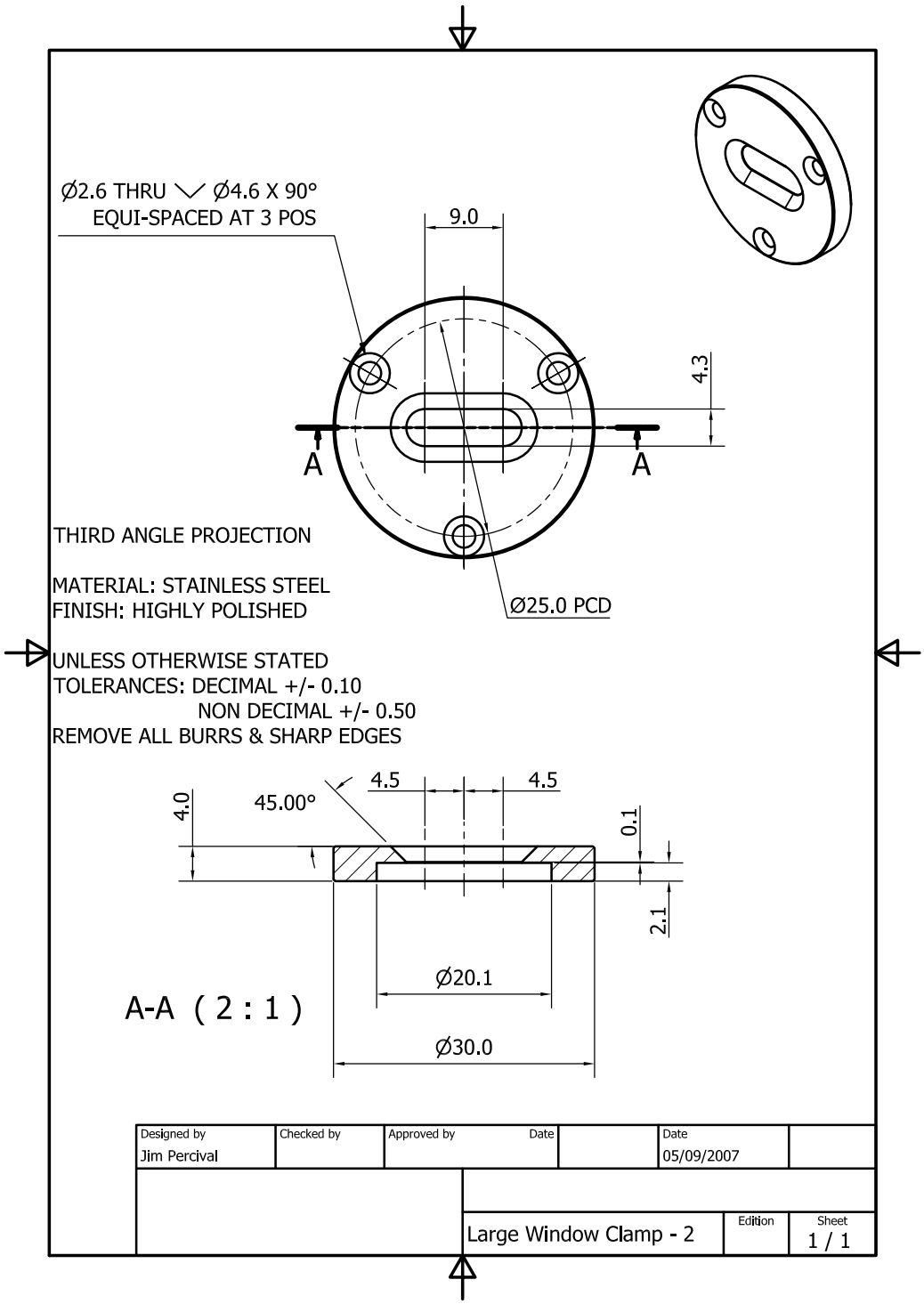


Figure E.5: Large window clamp (front)

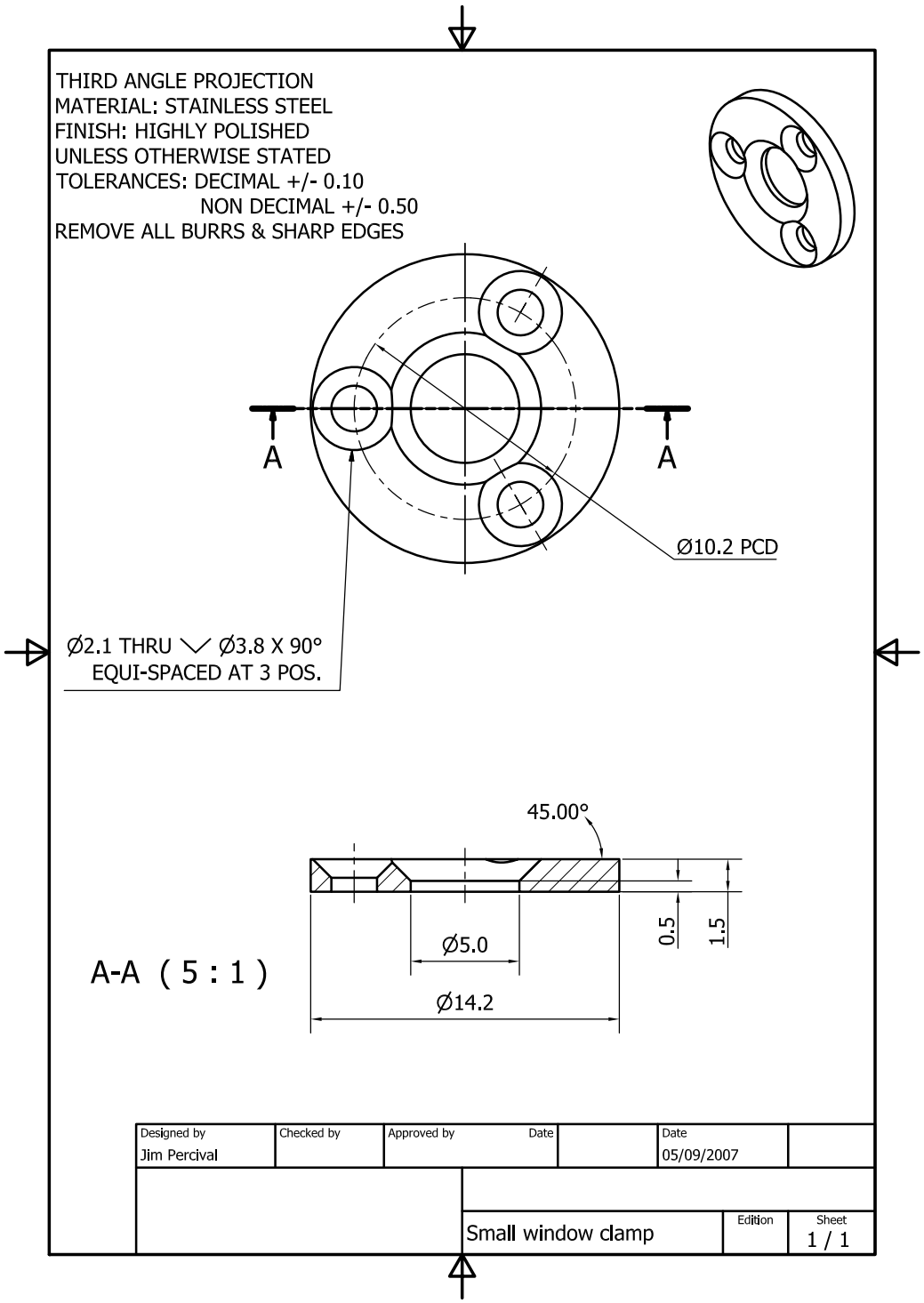


Figure E.6: Small window clamp (back)

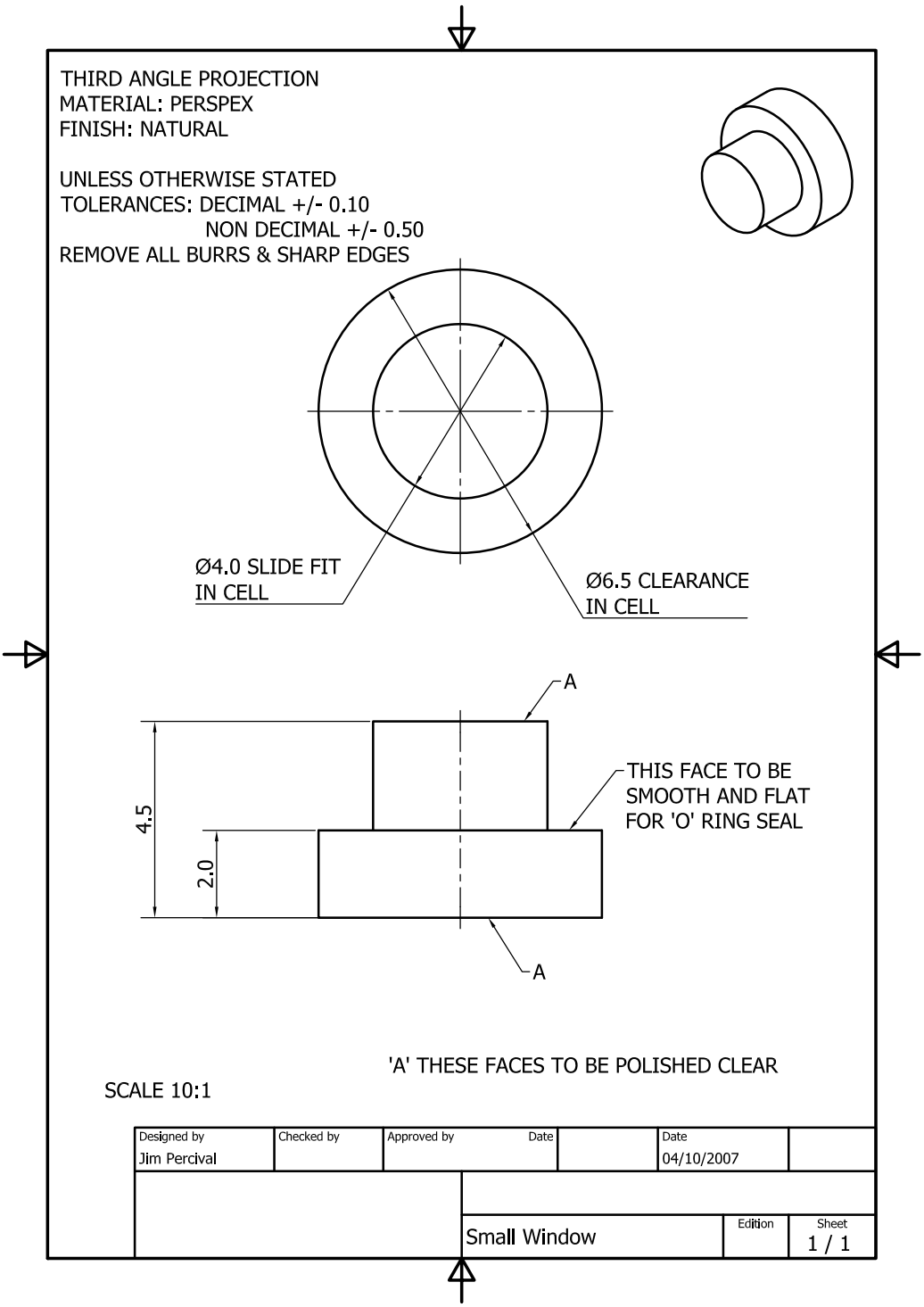


Figure E.7: Small window (back)

# F

# Contents of Accompanying DVD

The following files can be found on the accompanying DVD:

**Electronic version of the thesis** in the directory `Thesis/` (as a PDF file)

**Experimental results** in the directory `Experiments/` (raw data)

**MATLAB simulation** in the directory `Simulation/`

**LabView code** in the directory `LabView_Software/`

**Purchase orders** in the directory `Purchase_Orders/` (PDF files)

**Drawings** in the directory `Drawings/` (as PDF and DWG files)

# G

# Glossary of terms

**1D** One-dimensional

**2D** Two-dimensional

**3D** Three-dimensional

**AFM** Atomic force microscope

**CCD** Charge-coupled device

**CPU** Central processing unit

**D*Ala*** Lysine-D-Alanine-D-Alanine

**DNA** Deoxyribonucleic acid

**ELISA** Enzyme-linked immunosorbent assay

**FDA** Food and Drug Administration

**FIB** Focused ion beam

$FOM_k$ Figure of merit for sample number $k$

$GF$ Gauge factor

**HSA** Human serum albumin

$K_d$ Equilibrium dissociation constant, which is defined as $K_d = k_d/k_a$ with $k_a$ being the association constant and $k_d$ the dissociation constant.

**LOI** Line of interest

**MOSFET** Metal-oxide-semiconductor field-effect transistor

**MRSA** Methicillin-resistant staphylococcus aureus

**PCR** Polymerase chain reaction

***PEG*** Triethylene glycol

**ppm** Parts per million

**PSD** Photo sensitive detector

**ROI** Region of Interest

**VOC** Volatile organic component

**VRE** Vancomycin-resistant enterococcus

**VSE** Vancomycin-susceptible enterococcus

# Index

# Bibliography


[1] Moyu Watari. *In-plane Mechanochemistry at Model Biological Interfaces*. PhD thesis, London Centre for Nanotechnology & University College London, 2007.

[2] K Mullis, F Faloona, S Scharf, R Saiki, G Horn, and H Erlich. Specific enzymatic amplification of dna invitro- the polymerase chain-reaction. *Cold Spring Harbor Symposia on Quantitative Biology*, 51(Part 1):263–273, 1986.

[3] KB Mullis and FA Faloona. Specific synthesis of dna invitro via a polymerase-catalyzed chain-reaction. *Methods in Enzymology*, 155:335–350, 1987.

[4] http://web.mit.edu/invent/iow/mullis.html (received 07-sep-09).

[5] Eva Engvall and Peter Perlmann. Enzyme-linked immunosorbent assay (elisa) quantitative assay of immunoglobulin g. *Immunochemistry*, 8(9):871 – 874, 1971.

[6] B.K. Van Weemen and A.H.W.M. Schuurs. Immunoassay using antigen–enzyme conjugates. *FEBS Letters*, 15(3):232 – 236, 1971.

[7] S Avrameas and B Guilbert. Enzyme immunological determination of proteins using immunoadsorbants and enzyme labeled antigens.

[8] Rudolf M Lequin. Enzyme immunoassay (eia)/enzyme-linked immunosorbent assay (elisa). *Clin Chem*, 51(12):2415–2418, Dec 2005.

[9] Stratis Avrameas. Historical background of the invention of eia and elisa. *Clin Chem*, 52(7):1430–1; author reply 1431, Jul 2006.

[10] J Comley. Label-free detection. *Drug Discovery World*, page 74, 2004/5.

[11] G. Binnig, C.F. Quate, and C. Gerber. Atomic force microscope. *Physical Review Letters*, 56(9):930–933, 1986.

[12] Joseph Wafula Ndieyira, Moyu Watari, Alejandra Donoso Barrera, Dejian Zhou, Manuel Vogtli, Mattew Batchelor, Matthew A. Cooper, Torsten Strunz, Mike A. Horton, Chris Abell, Trevor Rayment, Gabriel Aeppli, and Rachel A.

Mckendry. Nanomechanical detection of antibiotic mucopeptide binding in a model for superbug drug resistance. *Nature Nanotechnology*, 3(11):691–696, NOV 2008.

[13] Nickolay V. Lavrik, Michael J. Sepaniak, and Panos G. Datskos. Cantilever transducers as a platform for chemical and biological sensors. *Review of Scientific Instruments*, 75(7):2229–2253, 2004.

[14] G.G. Yaralioglu, A. Atalar, S.R. Manalis, and C.F. Quate. Analysis and design of an interdigital cantilever as a displacement sensor. *Journal of Applied Physics*, 83(12):7405–7415, 1998.

[15] Gabriel Aeppli and Benjamin Dueck. Patent: Apparatus and method for measuring deformation of a cantilever using interferometry (wo/2008/129272), 2008.

[16] R. McKendry, J.Y. Zhang, Y. Arntz, T. Strunz, M. Hegner, H.P. Lang, M.K. Baller, U. Certa, E. Meyer, H.J. Guntherodt, and C. Gerber. Multiple label-free biodetection and quantitative dna-binding assays on a nanomechanical cantilever array. *Proceedings of the National Academy of Sciences of the United States of America*, 99(15):9783–9788, 2002.

[17] T. R. Albrecht, S. Akamine, T. E. Carver, and C. F. Quate. Microfabrication of cantilever styli for the atomic force microscope. *Journal of Vacuum Science & Technology A: Vacuum, Surfaces, and Films*, 8(4):3386–3396, 1990.

[18] C.A. Savran, A.W. Sparks, J. Sihler, Jian Li, Wan-Chen Wu, D.E. Berlin, T.P. Burg, J. Fritz, M.A. Schmidt, and S.R. Manalis. Fabrication and characterization of a micromechanical sensor for differential detection of nanoscale motions. *Microelectromechanical Systems, Journal of*, 11(6):703 – 708, dec 2002.

[19] G. K. Binnig, H Rohrer, and P Vettiger. Patent: Mass-storage applications of local probe arrays (no. 5,835,477), 1998.

[20] M. I. Lutwyche, M. Despont, U. Drechsler, U. Dürig, W. Häberle, H. Rothuizen, R. Stutz, R. Widmer, G. K. Binnig, and P. Vettiger. Highly parallel data storage system based on scanning probe arrays. *Applied Physics Letters*, 77(20):3299–3301, 2000.

[21] David Maraldo, Kishan Rijal, Gossett Campbell, and Raj Mutharasan. Method for label-free detection of femtogram quantities of biologics in flowing liquid samples. *ANALYTICAL CHEMISTRY*, 79(7):2762–2770, APR 1 2007.

[22] Claes Nylander, Bo Liedberg, and Tommy Lind. Gas detection by means of surface plasmon resonance. *Sensors and Actuators*, 3:79 – 88, 1982-1983.

[23] Bo Liedberg, Claes Nylander, and Ingemar Lunström. Surface plasmon resonance for gas detection and biosensing. *Sensors and Actuators*, 4:299 – 304, 1983.

[24] C. K. O'Sullivan and G. G. Guilbault. Commercial quartz crystal microbalances - theory and applications. *Biosensors and Bioelectronics*, 14(8-9):663 – 670, 1999.

[25] L. A. Pinnaduwage, D. L. Hedden, A. Gehl, V. I. Boiadjiev, J. E. Hawk, R. H. Farahi, T. Thundat, E. J. Houser, S. Stepnowski, R. A. McGill, L. Deel, and R. T. Lareau. A sensitive, handheld vapor sensor based on microcantilevers. *Review of Scientific Instruments*, 75(11):4554–4557, 2004.

[26] J.K. Gimzewski, Ch. Gerber, E. Meyer, and R.R. Schlittler. Observation of a chemical reaction using a micromechanical sensor. *Chemical Physics Letters*, 217(5-6):589 – 594, 1994.

[27] HP Lang, R Berger, F Battiston, JP Ramseyer, E Meyer, C Andreoli, J Brugger, P Vettiger, M Despont, T Mezzacasa, L Scandella, HJ Guntherodt, C Gerber, and JK Gimzewski. A chemical sensor based on a micromechanical cantilever array for the identification of gases and vapors. *Applied Physics A-Materials Science & Processing*, 66(Part 1 Suppl. S):S61–S64, MAR 1998. 9th International Conference on Scanning Tunneling Microscopy/Spectroscopy and Related Techniques, HAMBURG, GERMANY, JUL 20-25, 1997.

[28] G. Y. Chen, T. Thundat, E. A. Wachter, and R. J. Warmack. Adsorption-induced surface stress and its effects on resonance frequency of microcantilevers. *Journal of Applied Physics*, 77(8):3618–3622, 1995.

[29] T Thundat, GY Chen, RJ Warmack, DP Allison, and EA Wachter. Vapor detection using resonating microcantilever. *Analytical Chemistry*, 67(3):519–521, FEB 1 1995.

[30] T Thundat, EA Wachter, SL Sharp, and RJ Warmack. Detection of mercury-vapor using resonating microcantilever. *APPLIED PHYSICS LETTERS*, 66(13):1695–1697, MAR 27 1995.

[31] F. M. Battiston, J. P. Ramseyer, H. P. Lang, M. K. Baller, Ch. Gerber, J. K. Gimzewski, E. Meyer, and H. J. Güntherodt. A chemical sensor based on a microfabricated cantilever array with simultaneous resonance-frequency and bending readout. *Sensors and Actuators B: Chemical*, 77(1-2):122 – 131, 2001.

[32] Christiane Ziegler. Cantilever-based biosensors. *Anal Bioanal Chem*, 379(7-8):946–959, Aug 2004.

[33] Philip S Waggoner and Harold G Craighead. Micro- and nanomechanical sensors for environmental, chemical, and biological detection. *Lab Chip*, 7(10):1238–1255, 2007.

[34] L.G. Carrascosa, M. Moreno, M. Álvarez, and L.M. Lechuga. Nanomechanical biosensors: a new sensing tool. *Trends in Analytical Chemistry*, 25(3):196 – 206, 2006.

[35] Karen M. Goeders, Jonathan S. Colton, and Lawrence A. Bottomley. Microcantilevers: Sensing chemical interactions via mechanical motion. *Chemical Reviews*, 108(2):522–542, 2008.

[36] S. Timoshenko. Analysis of bi-metal thermostats. *J. Opt. Soc. Am.*, 11(3):233–233, 1925.

[37] JR Barnes, RJ Stephenson, ME Welland, C Gerber, and JK Gimzewski. Photothermal spectroscopy with femtojoule sensitivity using a micromechanical device. *Nature*, 372(6501):79–81, NOV 3 1994.

[38] A. M. Moulin, R. J. Stephenson, and M. E. Welland. Micromechanical thermal sensors: Comparison of experimental results and simulations. *Journal of Vacuum Science & Technology B: Microelectronics and Nanometer Structures*, 15(3):590–596, 1997.

[39] W Haiss. Surface stress of clean and adsorbate-covered solids. *Reports on Progress in Physics*, 64(5):591–648, MAY 2001.

[40] R Shuttleworth. The surface tension of solids. *Proceedings of the Physical Society. Section A*, 63(5):444, 1950.

[41] H Ibach. The role of surface stress in reconstruction, epitaxial growth and stabilization of mesoscopic structures. *SURFACE SCIENCE REPORTS*, 29(5-6):195–263, 1997.

[42] G Stoney. The tension of metallic films deposited by electrolysis. *Proceedings of the Royal Society of London.Series A*, 82:172–176, 1909.

[43] HJ Butt. A sensitive method to measure changes in the surface stress of solids. *Journal of Colloid and Interface Science*, 180(1):251–260, JUN 1 1996.

[44] K ROELL. Analysis of stress and strain distribution in thin-films and substrates. *Journal of Applied Physics*, 47(7):3224–3229, 1976.

[45] Moyu Watari, Jane Galbraith, Hans-Peter Lang, Marilyne Sousa, Martin Hegner, Christoph Gerber, Mike A Horton, and Rachel A McKendry. Investigating the molecular mechanisms of in-plane mechanochemistry on cantilever arrays. *J Am Chem Soc*, 129(3):601–609, Jan 2007.

[46] Maria L. Sushko, John H. Harding, Alexander L. Shluger, Rachel A. McKendry, and Moyu Watari. Physics of Nanomechanical Biosensing on Cantilever Arrays. *Advanced Materials*, 20(20):3848+, OCT 17 2008.

[47] J. Fritz, M. K. Baller, H. P. Lang, H. Rothuizen, P. Vettiger, E. Meyer, H. Güntherodt, C. Gerber, and J. K. Gimzewski. Translating biomolecular recognition into nanomechanics. *Science*, 288(5464):316–318, Apr 2000.

[48] Guanghua Wu, Haifeng Ji, Karolyn Hansen, Thomas Thundat, Ram Datar, Richard Cote, Michael F. Hagan, Arup K. Chakraborty, and Arunava Majumdar. Origin of nanomechanical cantilever motion generated from biomolecular interactions. *Proceedings of the National Academy of Sciences of the United States of America*, 98(4):1560–1564, 2001.

[49] Jeanne C Stachowiak, Min Yue, Kenneth Castelino, Arup Chakraborty, and Arun Majumdar. Chemomechanics of surface stresses induced by dna hybridization. *Langmuir*, 22(1):263–268, Jan 2006.

[50] N. Backmann, C. Zahnd, F. Huber, A. Bietsch, A. Pluckthun, H.P. Lang, H.J. Guntherodt, M. Hegner, and C. Gerber. A label-free immunosensor array using single-chain antibody fragments. *Proceedings of the National Academy of Sciences of the United States of America*, 102(41):14587–14592, 2005.

[51] G.H. Wu, R.H. Datar, K.M. Hansen, T. Thundat, R.J. Cote, and A. Majumdar. Bioassay of prostate-specific antigen (psa) using microcantilevers. *Nature Biotechnology*, 19(9):856–860, 2001.

[52] Roberto Raiteri, Massimo Grattarola, Hans-Jürgen Butt, and Petr Skládal. Micromechanical cantilever-based biosensors. *Sensors and Actuators B: Chemical*, 79(2-3):115 – 126, 2001.

[53] Manuel Voegtli. Nanomechanical detection of antibiotic-mucopeptide binding in a model for superbug drug resistance. First Year PhD Report, April 2009.

[54] D. Sarid. *Scanning Force Microscopy*. Oxford University Press, New York, 1991.

[55] Y. Martin, C. C. Williams, and H. K. Wickramasinghe. Atomic force microscope–force mapping and profiling on a sub 100-[a-ring] scale. *Journal of Applied Physics*, 61(10):4723–4729, 1987.

[56] R. R. Grüter and Z. Khan and R. Paxman and J. W. Ndieyira and B. Dueck and B. A. Bircher and J. L. Yang and U. Drechsler and M. Despont and R. A. McKendry and B. W. Hoogenboom. Disentangling mechanical and mass effects on nanomechanical resonators. *Applied Physics Letters*, 96(2):023113, 2010.

[57] B. Ilic, Y. Yang, and H.G. Craighead. Virus detection using nanoelectromechanical devices. *Applied Physics Letters*, 85(13):2604–2606, 2004.

[58] T.P. Burg, M. Godin, S.M. Knudsen, W. Shen, G. Carlson, J.S. Foster, K. Babcock, and S.R. Manalis. Weighing of biomolecules, single cells and single nanoparticles in fluid. *Nature*, 446(7139):1066–1069, 2007.

[59] C. L. Britton, R. L. Jones, P. I. Oden, Z. Hu, R. J. Warmack, S. F. Smith, W. L. Bryan, and J. M. Rochelle. Multiple-input microcantilever sensors. *Ultramicroscopy*, 82(1-4):17 – 21, 2000.

[60] Jorge Amírola, Angel Rodríguez, Luis Castañer, J.P. Santos, J. Gutiérrez, and M.C. Horrillo. Micromachined silicon microcantilevers for gas sensing applications with capacitive read-out. *Sensors and Actuators B: Chemical*, 111-112:247 – 253, 2005. Eurosensors XVIII 2004 - The 18th European Conference on Solid-State Transducers.

[61] M. Tortonese, R.C. Barrett, and C.F. Quate. Atomic resolution with an atomic force microscope using piezoresistive detection. *Applied Physics Letters*, 62(8):834–836, 1993.

[62] Boisen, Thaysen, Jensenius, and Hansen. Environmental sensors based on micromachined cantilevers with integrated read-out. *Ultramicroscopy*, 82(1-4):11–16, Feb 2000.

[63] G. Shekhawat, S.H. Tark, and V.P. Dravid. Mosfet-embedded microcantilevers for measuring deflection in biomolecular sensors. *Science*, 311(5767):1592–1595, 2006.

[64] Soo-Hyun Tark, Arvind Srivastava, Stanley Chou, Gajendra Shekhawat, and Vinayak P. Dravid. Nanomechanoelectronic signal transduction scheme with metal-oxide-semiconductor field-effect transistor-embedded microcantilevers. *Applied Physibarcs Letters*, 94(10):104101, 2009.

[65] Gerhard Meyer and Nabil M. Amer. Novel optical approach to atomic force microscopy. *Applied Physics Letters*, 53(12):1045–1047, 1988.

[66] M. Hoummady, E. Farnault, T. Yahiro, and H. Kawakatsu. Simultaneous optical detection techniques, interferometry, and optical beam deflection for dynamic mode control of scanning force microscopy. volume 15, pages 1539–1542. AVS, 1997.

[67] Christian Gerthsen. *Gerthsen Physik*. Springer, 19 edition, 1997.

[68] J Brugger, R A Buser, and N F de Rooij. Micromachined atomic force microprobe with integrated capacitive read-out. *Journal of Micromechanics and Microengineering*, 2(3):218–220, 1992.

[69] T. Göddenhenrich, H. Lemke, U. Hartmann, and C. Heiden. Force microscope with capacitive displacement detection. *Journal of Vacuum Science & Technology A: Vacuum, Surfaces, and Films*, 8(1):383–387, 1990.

[70] Alejandra Donoso Barrera. *Nanomechanical Sensor Arrays for Antibiotic Drug Analysis*. PhD thesis, London Centre for Nanotechnology & University College London, 2008.

[71] A. C. H. Rowe, A. Donoso-Barrera, Ch. Renner, and S. Arscott. Giant room-temperature piezoresistance in a metal-silicon hybrid structure. *Phys Rev Lett*, 100(14):145501, Apr 2008.

[72] S. Jeon and T. Thundat. Instant curvature measurement for microcantilever sensors. *Applied Physics Letters*, 85(6):1083–1084, 2004.

[73] J. Mertens, M. Alvarez, and J. Tamayo. Real-time profile of microcantilevers for sensing applications. *Applied Physics Letters*, 87(23):–, 2005.

[74] M. Helm, J.J. Servant, F. Saurenbach, and R. Berger. Read-out of micromechanical cantilever sensors by phase shifting interferometry. *Applied Physics Letters*, 87(6):–, 2005.

[75] Sven Kelling, François Paoloni, Juzheng Huang, Victor P. Ostanin, and Stephen R. Elliott. Simultaneous readout of multiple microcantilever arrays with phase-shifting interferometric microscopy. *Review of Scientific Instruments*, 80(9):093101, 2009.

[76] A. Oral, R. A. Grimble, H. Ö. Özer, and J. B. Pethica. High-sensitivity noncontact atomic force microscope/scanning tunneling microscope (nc afm/stm) operating at subangstrom oscillation amplitudes for atomic resolution imaging and force spectroscopy. *Review of Scientific Instruments*, 74(8):3656–3663, 2003.

[77] B. W. Hoogenboom, P. L. T. M. Frederix, J. L. Yang, S. Martin, Y. Pellmont, M. Steinacher, S. Zäch, E. Langenbach, H.-J. Heimbeck, A. Engel, and H. J. Hug. A fabry–perot interferometer for micrometer-sized cantilevers. *Applied Physics Letters*, 86(7):074101, 2005.

[78] D. Iannuzzi, S. Deladi, V. J. Gadgil, R. G. P. Sanders, H. Schreuders, and M. C. Elwenspoek. Monolithic fiber-top sensor for critical environments and standard applications. *Applied Physics Letters*, 88(5):053501, 2006.

[79] Jana Wehrmeister, Achim Fuß, Frank Saurenbach, Rüdiger Berger, and Mark Helm. Readout of micromechanical cantilever sensor arrays by fabry-perot interferometry. *Review of Scientific Instruments*, 78(10):104105, 2007.

[80] K. Zinoviev, C. Dominguez, J. A. Plaza, V. Cadarso, and L. M. Lechuga. Light coupling into an optical microcantilever by an embedded diffraction grating. *Appl. Opt.*, 45(2):229–234, 2006.

[81] Maria Nordström, Dan A. Zauner, Montserrat Calleja, Jörg Hübner, and Anja Boisen. Integrated optical readout for miniaturization of cantilever-based sensor system. *Applied Physics Letters*, 91(10):103512, 2007.

[82] Poggendorff. Ein vorschlag zum messen der magnetischen abweichung. *Annalen der Physik*, 83(5):121–130, 1826.

[83] M Born. *Optk.* Springer, 1972 (3rd Edition).

[84] Joseph W. Goodman. *Introduction to Fourier Optics.* THE McGRAW-HILL COMPANIES, INC., 2nd edition, 1996.

[85] A Sommerfeld. *Mathematical Theory of Diffraction.* Birkhaeuser Boston, 2004.

[86] FM Grimaldi. *Physicomathesis de lumine, coloribus, et iride, aliisque annexis.* 1665 in Bologna.

[87] Huygens. *Abhandlungen über das Licht (german transl. of "Traite de la Lumiere").* 1960.

[88] Arnold Sommerfeld. *Optics: Lectures on Theoretical Physics, Vol. IV.* ACADEMIC PRESS INC., 1954.

[89] T Young. The bakerian lecture: On the theory of light and colours. *Philosophical Transactions of the Royal Society of London*, 92:12–48, 1802.

[90] T Young. The bakerian lecture: Experiments and calculations relative to physical optics. *Philosophical Transactions of the Royal Society of London*, 94:1–6, 1804.

[91] G Kirchhoff. Zur theorie der lichtstrahlen. *Annalen der Physik*, 254:663–695, 1883.

[92] A Sommerfeld. Mathematische theorie der diffraction. *Mathematische Annalen*, 47:317–347, 1896.

[93] E Hecht. *Optics (Series: Schaum's Outlines)*. McGraw-Hill, 1975.

[94] E Hecht. *Optics*, volume 3rd. ADDISON-WESLEY, 1998.

[95] M Born and E Wolf. *Principles of Optics*. Pergamon Press, Oxford, 6th ed. (with corrections) edition, 1980.

[96] JB Keller. Geometrical theory of diffraction. *Journal of the Optical Society of America*, 52(2):116, 1962.

[97] T. John, U. Behn, and R. Stennarius. Laser diffraction by periodic dynamic patterns in anisotropic fluids. *The European Physical Journal B - Condensed Matter and Complex Systems*, 35:267–278, 2003.

[98] J A Ratcliffe. Some aspects of diffraction theory and their application to the ionosphere. *Reports on Progress in Physics*, 19(1):188–267, 1956.

[99] D. Sayre. Some implications of a theorem due to shannon. *Acta Crystallographica*, 5(6):843, Nov 1952.

[100] Richard E. Blahut. *Theory of Remote Image Formation*. Cambridge University Press, 2004.

[101] Gerchberg and Saxton. A practical algorithm for the determination of the phase from image and diffraction plane pictures. *Optik*, 35:237, 1972.

[102] Gerchberg. Super-resolution through error energy reduction. *Optica Acta*, 21:709–720, 1974.

[103] J. R. Fienup. Phase retrieval algorithms: a comparison. *Appl. Opt.*, 21(15):2758–2769, 1982.

[104] I. K. Robinson, I. A. Vartanyants, G. J. Williams, M. A. Pfeifer, and J. A. Pitney. Reconstruction of the shapes of gold nanocrystals using coherent x-ray diffraction. *Phys. Rev. Lett.*, 87(19):195505, Oct 2001.

[105] Jianwei Miao, Tetsuya Ishikawa, Bart Johnson, Erik H. Anderson, Barry Lai, and Keith O. Hodgson. High resolution 3d x-ray diffraction microscopy. *Phys. Rev. Lett.*, 89(8):088303, Aug 2002.

[106] Mark A. Pfeifer, Garth J. Williams, Ivan A. Vartanyants, Ross Harder, and Ian K. Robinson. Three-dimensional mapping of deformation field inside a nanocrystal. *Nature*, 442:63–66, 2006.

[107] Ian Robinson and Ross Harder. Coherent x-ray diffraction imaging of strain at the nanscale. *Nature Materials*, 8:291–298, 2009.

[108] R. J. Sault. Uniqueness condition for the phase problem in one dimension. *Opt. Lett.*, 9(8):325–326, 1984.

[109] RHT Bates. Fourier phase problems are uniquely solvable in more than one dimension .1. underlying theory. *OPTIK*, 61(3):247–262, 1982.

[110] D. Gabor. A new microscopic principle. *Nature*, 161(4098):777, May 1948.

[111] D. H. Williams. The glycopeptide story–how to kill the deadly 'superbugs'. *Nat Prod Rep*, 13(6):469–477, Dec 1996.

[112] Williams and Bardsley. The vancomycin group of antibiotics and the fight against resistant bacteria. *Angewandte Chemie International Edition*, 38:1172–1193, 1999.

[113] J. Lahiri, L. Isaacs, J. Tien, and G. M. Whitesides. A strategy for the generation of surfaces presenting ligands for studies of binding based on an active ester as a common reactive intermediate: a surface plasmon resonance study. *Anal Chem*, 71(4):777–790, Feb 1999.

[114] K. L. Prime and G. M. Whitesides. Self-assembled organic monolayers: model systems for studying adsorption of proteins at surfaces. *Science*, 252(5010):1164–1167, May 1991.

[115] Nickolay V. Lavrik and Panos G. Datskos. Femtogram mass detection using photothermally actuated nanomechanical resonators. *Applied Physics Letters*, 82(16):2697–2699, 2003.

[116] J. Teng and P.D. Prewett. Focused ion beam fabrication of thermally actuated bimorph cantilevers. *Sensors and Actuators A: Physical*, 123-124:608 – 613, 2005. Eurosensors XVIII 2004 - The 18th European conference on Solid-State Transducers.

[117] Nan Yao. *Focused Ion Beam Systems: Basics and Applications*. Cambridge University Press, 2007.

[118] Wuxia Li and P A Warburton. Low-current focused-ion-beam induced deposition of three-dimensional tungsten nanoscale conductors. *Nanotechnology*, 18(48):485305 (5pp), 2007.

[119] Leonard Mandel and Emil Wolf. *Optical Coherence and Quantum Optics*. Cambridge University Press, 1995.

[120] Ralph G. Nuzzo and David L. Allara. Adsorption of bifunctional organic disulfides on gold surfaces. *Journal of the American Chemical Society*, 105:4481, 1983.

[121] Hans Peter Lang, Martin Hegner, and Christoph Gerber. Cantilever array sensors. *Materials Today*, 8(4):30 – 36, 2005.

[122] T.W. Mayes and B.F. Melton. Fraunhofer diffraction of visible light by a narrow slit. *American Journal of Physics*, 62:397–403, 1993.

[123] David Hopwood, Stuart Levy, Richard P. Wenzel, Nafsika Georgopapadakou, Richard H. Baltz, Sujata Bhavnani, and Edward Cox. A call to arms. *Nature Reviews Drug Discovery*, 6(1):8–12, JAN 2007.

[124] Gary Taubes. The bacteria fight back. *Science*, 321(5887):356–361, JUL 18 2008.

[125] Alisa Opar. Bad bugs need more drugs. *Nature Reviews Drug Discovery*, 6(12):943–944, DEC 2007.

[126] Ralph E. Christoffersen. Antibiotics - an investment worth making? *Nature Biotechnology*, 24(12):1512–1514, DEC 2006.

[127] Norris E Allen and Thalia I Nicas. Mechanism of action of oritavancin and related glycopeptide antibiotics. *FEMS Microbiol Rev*, 26(5):511–532, Jan 2003.

[128] D. Stauffer and A. Aharony. *Introduction to percolation theory.* CRC press, 1994.

[129] B Alberts, A Johnson, J Lewis, M Raff, K Roberts, and P Walter. *Molecular Biology of the Cell.* Garland Science, 4th edition, 2002.

[130] M. A. Cooper, M. T. Fiorini, C. Abell, and D. H. Williams. Binding of vancomycin group antibiotics to d-alanine and d-lactate presenting self-assembled monolayers. *Bioorg Med Chem*, 8(11):2609–2616, Nov 2000.

[131] Zhiyu Hu, Tim Seeley, Sebastian Kossek, and Thomas Thundat. Calibration of optical cantilever deflection readers. *Review of Scientific Instruments*, 75(2):400–404, 2004.

[132] L. Y. Beaulieu, Michel Godin, Olivier Laroche, Vincent Tabard-Cossa, and Peter Grütter. Calibrating laser beam deflection systems for use in atomic force microscopes and cantilever sensors. *Applied Physics Letters*, 88(8):083108, 2006.

[133] G. Galitonov, S. Birtwell, N. Zheludev, and H. Morgan. High capacity tagging using nanostructured diffraction barcodes. *Opt. Express*, 14(4):1382–1387, 2006.

[134] D.R. Evans and V.S.J. Craig. Sensing cantilever beam bending by the optical lever technique and its application to surface stress. *Journal of Physical Chemistry B*, 110(11):5450–5461, MAR 23 2006.